Multiscale Modeling of Partially Crystalline Materials

by

Futianyi Wang

A dissertation submitted in partial fulfillment
of the requirements for the degree of
Doctor of Philosophy
(Chemical Engineering)
in the University of Michigan
2023

Doctoral Committee:

Professor Ronald G. Larson, Chair
Assistant Professor Bryan R. Goldsmith
Professor Angela Violi
Professor Robert M. Ziff

Futianyi Wang

wangfty@umich.edu

ORCID iD: 0000-0001-7000-6406

Dedication

This dissertation is dedicated to all the people who have supported me through my education. Thanks for making me see this adventure through to the end.

Acknowledgments

I am immensely grateful to my advisor, Dr. Larson, for his unwavering guidance, support, and patience throughout my Ph.D. studies. His expertise and enthusiasm have helped me navigate through tough times and inspired me to pursue excellence in my research. The invaluable five years under his mentorship have contributed not only to my professional development but also personal growth, which I will cherish for the rest of my life.

I also want to extend my sincere appreciation to my wife, Shujun, who has been a constant source of strength, love, and support for me. As a fellow Ph.D. candidate, she understands the unique challenges of pursuing a doctorate and has encouraged and motivated me to overcome obstacles. Meeting her in graduate school has forever changed my life for the better, and I wish her all the best as she completes her own Ph.D.

I would also like to acknowledge the endless support of my parents throughout my academic journey. Their love and belief in me have been the foundation of my success.

Finally, I would like to express my gratitude to my lab mates and the staff in the Chemical Engineering department for their help and support.

Thank you all for making this achievement possible.

Table of Contents

List of Tables

List of Figures

Abstract

Simulation and modeling methods covering multiple time and length scales are here applied to study crystals and materials with partial crystallinity. The first system investigated is the aqueous emulsion of cationic surfactant and fatty alcohol, known as “lamellar gel networks”, which contains extended networks of bilayers with in-plane solid-like order (L_β phase). Fully atomistic molecular dynamics (MD) simulations were conducted to study the equilibrium bilayer structure. Lateral pressure and temperature scans along reversible pathways were used to avoid kinetic bottlenecks and drive phase changes, including formation of the $L_{\beta I}$ phase with interdigitated tails of opposing leaflets enabled at negative lateral pressure. Thermodynamic integration, with extrapolations to infinitely slow scans, yielded a negative free energy difference between the interdigitated $L_{\beta I}$ and non-interdigitated L_β phase, which is consistent with the spontaneous formation of L_β phase under atmospheric pressure in simulation.

To predict the macroscopic properties of lamellar gel networks in terms of their complex rheology and shear-rate inhomogeneities, a relatively simple thixotropic constitutive model was proposed. The model has an elasto-plastic stress and a smoothly decreasing modulus near a solid boundary, motivated by mesoscopic scale analysis of the effect of confinement and shear flow on lamellae orientation near surfaces. The model qualitatively captures the rheology features of the lamellar gel, including thixotropic shear-thinning, slow creep under small shear stress and abrupt transition to fast yielding at higher stress, as well as a gap-dependent behavior. The introduction of the modulus gradient enables the model to predict the unique shear banding phenomenon of lamellar gel networks wherein a thin, fast-shearing band exists near the boundary that widens only slowly with increased apparent shear rate until a very high rate is reached, while the bulk moves as a plug.

The crystallization process of pharmaceutical cocrystals was also investigated. A coarse-grained model was developed for the cocrystal of carbamazepine and succinic acid using iterative Boltzmann inversion with crystal structural information from atomistic simulation. The coarse-grained model allowed direct simulation of cocrystal growth in the melt, which is extremely challenging with a fully atomistic model. The growth kinetics of three different facets were analyzed, and the (1 0 -1) facet exhibited the slowest growth rate, consistent with the crystal morphology prediction from attachment energy theory. Well-tempered metadynamics simulations were performed to study the molecular orientation during single molecule adsorption at different facets, revealing that hydrogen bonding and layer structure were factors that may cause the difference in growth rates.

The utilization of simulation and modeling techniques across various time and length scales in our research has resulted in the creation of innovative methods and models that provide valuable insights into the intricate behavior of partially crystalline materials.

Chapter 1 Introduction

1.1 Introduction

Modeling and simulation have become increasingly crucial in the field of material science over the past few decades due to the development of new simulation methods and advancements in computational power. Material science involves many interesting problems that span multiple spatial or temporal scales. The microscopic structure and interactions ultimately determine the material properties at the macroscopic level, which are of interest for their applications. Well-established computational approaches have been developed over the years to handle relevant phenomena at different length scales, which can be generally categorized into four characteristic length levels: atomic ($\sim 10^{-9}$ m or a few nanometers), microscopic ($\sim 10^{-6}$ m or a few micrometers), mesoscopic ($\sim 10^{-4}$ m or hundreds of micrometers), and macroscopic ($\sim 10^{-2}$ m or centimeters and beyond).[1] Each of the four length scales mentioned above is typically associated with a corresponding timescale, which ranges roughly from femtoseconds to picoseconds, to nanoseconds, to milliseconds and beyond, respectively.[1]

The smallest scale is the atomic scale, where the interactions of the electrons among the atoms are dictated by their quantum mechanical state. Quantum Monte Carlo (QMC)[2] and quantum chemistry (QC)[3] methods can explicitly and accurately describe electrons at the atomic scale, although they are computationally demanding and limited to systems containing only a few tens of electrons. For larger systems, more efficient methods based on density-functional theory (DFT) and local density approximation (LDA) can be employed.[4,5] These methods provide sufficiently accurate results for static properties such as bulk crystal properties or point defects, which can be modeled reasonably well with a small number of atoms.[1]

At the microscopic scale, interactions between atoms and molecules are often modeled using classical potentials that capture the effects of bonding and intermolecular forces. Molecular dynamics (MD) and Monte Carlo (MC) simulations are two common methods for simulating systems containing hundreds and thousands of molecules.[6] Molecular dynamics simulation can be used to study the dynamic evolution of a system by analyzing the trajectories of atoms and molecules, which are determined by numerically solving Newton's equations of motion. In contrast, Monte Carlo methods use equilibrium statistical mechanics to generate states according to the appropriate Boltzmann distribution.

On the larger mesoscopic scale, lattice defects such as dislocations, grain boundaries, and other microstructural elements are often the focus of interest.[1] The atomic degrees of freedom are typically ignored, and large-scale entities are usually modeled with interactions derived from phenomenological theories. For example, the development of dislocation dynamics (DD) method has been a significant milestone in computational materials science and engineering, as it handles the kinetics of dislocations under strain, which is concerned with the mechanical behavior of solids.[7]

Finally, phenomena on the macroscopic scale are generally governed by constitutive laws in continuum fields such as density, velocity, temperature, displacement, and stress fields. The constitutive laws are usually formulated to capture the effects of lattice defects and microstructural elements on materials properties.[1] Finite-element (FE) methods[8] are commonly used to model materials as an elastic continuum and examine their large-scale properties.[9] Another example is the use of continuum Navier-Stokes equations in the modeling of fluids.

Crystalline systems exhibit unique properties stemming from their microstructure, making them useful in a variety of applications. A crystal is a solid material whose constituents form a highly ordered microscopic structure. Examples include diamond, ice, and salt, where the constituents are atoms, molecules, and ions respectively. A broader definition of partially crystalline materials includes systems with partially aligned molecules, such as polymers with folded and stacked chains and liquid crystals.[10] The microstructure and crystallization process of these materials primarily determine their properties, making them essential to the materials' applications and processing. To use modeling and simulations to study crystals and partially crystalline materials, appropriate methods must be chosen based on the time and length scale of the problem of interest, and there are often additional challenges associated with the limitations of the methods.

In this dissertation, two different systems were investigated: lamellar gel networks composed of surfactant bilayers in a liquid crystalline state and pharmaceutical cocrystals. The findings and problems solved are presented in the following fashion:

Chapter 2 describes the use of atomistic MD simulations to determine the equilibrium phase structure of the surfactant bilayers in partially crystalline states. Different bilayer phases were simulated, and a thermodynamic integration scheme was designed to circumvent the kinetic issues associated with bilayer phase change and compute the free energy cost of bilayer interdigitation. The result of this study provides insight into the phase behavior of bilayers and membranes.

In Chapter 3, a thixotropic constitutive model was developed to predict the complex rheology of lamellar gels. The phenomenological structural kinetic model is complemented by a boundary-induced gradient derived from mesoscopic scale analysis of lamellae orientation under shear flow. The model qualitatively captures the rheology features of lamellar gels and predicts the unique flow inhomogeneities observed in experiments.

Chapter 4 discusses a coarse-graining approach for studying the crystallization of pharmaceutical cocrystals. The coarse-grained model was developed to overcome the kinetic limitation of atomistic simulations. Crystal growth from different facets of carbamazepine and succinic acid cocrystal in melt was directly simulated, and surface adsorption was analyzed with well-tempered metadynamics simulations.

Finally, we present a summary of the main results and conclusions of this dissertation in Chapter 5.

1.2 Reference

[1] Lu, G., & Efthimios, K. (2004). An Overview of Multiscale Simulations of Materials. https://doi.org/10.48550/arXiv.cond-mat/0401073

[2] Foulkes, W. M. C., Mitas, L., Needs, R. J., & Rajagopal, G. (2001). Quantum Monte Carlo Simulations of Solids. *Rev. Mod. Phys.*, 73, 33. https://doi.org/10.1103/RevModPhys.73.33

[3] Szabo, A., & Ostlund, N. S. (1989). *Modern Quantum Chemistry*. McGraw-Hill, New York.

[4] Hohenberg, P., & Kohn, W. (1964). Inhomogeneous Electron Gas. *Phys. Rev.*, 136, B864. https://doi.org/10.1103/PhysRev.136.B864

[5] Payne, M. C., Teter, M. T., Allan, D. C., Arias, T. A., & Joannopoulos, G. (1992). Iterative Minimization Techniques for *ab initial* Total-energy Calculations: Molecular Dynamics and Conjugate Gradients. *Rev. Mod. Phys.*, 64, 1045. https://doi.org/10.1103/RevModPhys.64.1045

[6] Duchstein, P., Ectors, P., & Zahn, D. (2019). Chapter Thirteen: Molecular Simulations of crystal growth: From understanding tailoring. *Adv. Inorg. Chem.*, 73, 507-529. https://doi.org/10.1016/bs.adioch.2018.11.004

[7] Bulatov, V. V., Tang, M., & Zbib, H. M. (2001). Crystal Plasticity from Dislocation Dynamics. *MRS Bull.*, 26, 191. https://doi.org/10.1557/mrs2001.41

[8] Hughes, T. J. R. (1987). *The Finite Element Method: Linear Static and Dynamic Finite Element Analysis*. Prentice-Hall, Eaglewood Cliffs, New Jersey.

[9] Dawson, P. R., & Marin, E. B. (1998). Computational Mechanics for Metal Deformation Processes using Polycrystal Plasticity. Adv. Appl. Mech., 34, 77. https://doi.org/10.1016/S0065-2156(08)70320-X

[10] Khokhlov, A. R., & Semenov, A. N. (1982). Liquid-crystalline ordering in the solution of partially flexible macromolecules. *Phys. A: Stat. Mech. Appl.*, 112, 3, 605-614 https://doi.org/10.1016/0378-4371(82)90199-6

Chapter 2 Free Energy Cost of Interdigitation of Lamellar Bilayers of Fatty Alcohols with Cationic Surfactants from Molecular Dynamics Simulation

This Chapter is based on the previously published article listed below:

Wang, F., & Larson, R. G. (2021). Free Energy Cost of Interdigitation of Lamellar Bilayers of Fatty Alcohols with Cationic Surfactants from Molecular Dynamics Simulations. *J. Phys. Chem. B*, 125, 9, 2389–2397.

2.1 Introduction

Surfactants that lower the surface tension between oil and water are usually amphiphilic organic compounds with hydrophobic tail groups and hydrophilic head groups, which can be either ionic or non-ionic. In the bulk aqueous phase, surfactants can aggregate into micelles with the aggregate core formed by the hydrophobic tails and the hydrophilic heads in contact with surrounding water. Other types of aggregate structure can also be formed such as spherical or cylindrical micelles or bilayers, depending on surfactant concentration and its chemical structure. Fatty alcohols are also amphiphilic molecules with a polar hydroxyl head associated attached to an alkyl chain tail. Long-chain alcohols such as cetyl (C_{16}) and stearyl (C_{18}) alcohols are only weak emulsifiers by themselves and adopt various crystalline structures with poor hydration capacity in water.[1] However, when they are mixed with surfactants in an appropriate ratio in excess water, stable emulsion can form, which are widely used in pharmaceutical creams, cosmetic lotions, hair care products and as drug delivery carriers with other essential additives such as salt and perfume.[2,3] Hair conditioner has been a particularly important product application for these emulsions in the hair and skin-care industry due to the enormous market demand for such products over the past few decades. The cationic surfactant in the conditioner adheres well to the slightly negatively charged wet hair, while the fatty alcohol component helps in lubricating and moisturizing the hair surface to provide a smooth feel.

These pseudo-ternary mixtures contain extended and highly interconnected networks often referred as “lamellar gel networks,” which can withstand elastic deformation and have interesting rheological properties.[4] As a result of the multiphase structure, lamellar gel networks of surfactant and fatty alcohol have an opaque creamy appearance and exhibit highly viscous, shear-thinning rheology.[5,6] The basic units of the networks are highly swollen bilayers self-assembled from surfactant and fatty alcohol molecules with regular in-plane spacing, and inter-lamellar regions filled with water.[7] The swelling of the lamellar stacks by water is caused by steric or electrostatic repulsion of the surfactant head groups which produces an osmotic pressure in the hydrophilic region of the lamellae.[8] The bilayers in lamellar gel networks can form different phases depending on their composition and temperature, similar to other bilayer systems such as lipid membranes.[9] At low temperature, the bilayers form a stiff, gel phase known as the L_β phase, where the C-C bonds in the hydrocarbon chains adopt all-trans conformations and the molecules are tightly packed in hexagonal order within each leaflet. Upon increase of temperature, gauche conformations take over and the bilayer melts into a more fluidic, liquid crystalline L_α phase with loosely packed hydrocarbon chains and shortened extension. Several other structures have been reported for the gel phase, such as an $L_{\beta I}$ phase with an interdigitated bilayer and an $L_{\beta'}$ phase with molecules tilted with respect to the bilayer normal.[10,11] In the interdigitated gel phase ($L_{\beta I}$), the hydrocarbon chains interpenetrate to maximize van der Waals interactions and reduce head group crowding at the expense of unfavorable exposure to the surrounding aqueous solution.[12]

Despite the wide application of lamellar gel networks, their flow properties and microstructures and how these are controlled at the molecular level remain relatively mysterious. In particular, whether those bilayers are interdigitated or not, and what controls this property, is as yet not well understood. In addition to rheology characterization, small-angle X-ray scattering (SAXS) and X-ray diffraction have been used to investigate the structure of lamellar bilayers.[13,14] Other experimental approaches such as Fourier-transform infrared spectroscopy (FTIR), NMR and differential scanning calorimetry (DSC) have also been applied to study the phase transitions of other systems such as lipid bilayers.[15] While these experimental studies have produced valuable insight into understanding bilayer structure, the majority of them yield only one-dimensional information mostly along the bilayer normal, namely inter-lamellar spacings and thickness of bilayers. In contrast, computer simulations have emerged as an attractive technique to obtain microscopic three-dimensional structural information of bilayers. The models employed in simulations range from fully atomistic models to coarse-grained bead-spring descriptions. With calibrated force-field parameters, molecular dynamics (MD) simulations can play an important role in investigating bilayer properties and their dependences on the composition and molecular structure of the constituents, and their molecular level interactions.[9]

Although there are extensive MD simulation studies on lipid bilayers and surfactant micelles, there is limited information on mixed surfactant systems and on bilayer interdigitation, especially from all-atom simulations. Shigematsu et al. investigated stretched-induced interdigitation of a phospholipid/cholesterol bilayer with united-atom MD simulations and proposed a free energy model.[16] Laner et al. used united-atom models to study methanol-induced interdigitation of glycerol-monopalmitate lipid bilayers and found that while the simulation starting structure could affect the final structure formed, no direct transition from $L_{\beta I}$ to L_{β} phase was observed.[17,18] Kranenburg et al. also simulated alcohol-induced interdigitation of lipid bilayers facilitated by using more coarse-grained dissipative particle dynamics (DPD) simulation.[19] With DPD simulation, Lu and Guo demonstrated the phase behavior of lipid bilayers including an interdigitated gel phase.[20] In a recent study, Seo et al. revealed how interdigitated acyl chains modulated the partitioning of cholesterol in the opposing leaflet and affected the phase behavior of an asymmetric lipid membrane with coarse-grained MD simulation.[21] For a mixture of cationic surfactant and fatty alcohol present in lamellar gel networks, Debnath et al. used united-atom simulations to investigate the effect of bilayer composition and water concentration on the phase transition on non-interdigitated and interdigitated bilayers in separate publications, leaving some confusion as to which one is the equilibrium structure.[9,22] In addition, Leonforte et al. were able to simulate with an all-atom forcefield the gel-fluid bilayer transition of a similar surfactant/fatty alcohol mixture.[23] Because of the limited time and length scales accessible with all-atom MD simulations, kinetic trapping is oftentimes an issue especially at low temperature, which prevents the formation of the equilibrium structure of these bilayer systems in the gel state. Thus, although insights are gained from simulations such as these, conclusive evidence determining whether interdigitation is thermodynamically favored or not for a given model forcefield, is still lacking.

Comparing the free energies of the L_{β} and $L_{\beta I}$ phases might determine which of them is the equilibrium state, but the lack of a smooth transition route between the two phases has prevented us, despite numerous efforts, from calculating the free energy difference with methods such as umbrella sampling, where the degree of interdigitation is the reaction coordinate. In this paper, we show that lateral pressure as a second parameter besides temperature allows the creation of reversible pathways to connect L_β and $L_{\beta I}$ phase. Based on this discovery, we propose a method to calculate the free energy cost of bilayer interdigitation using thermodynamic integration.

2.2 Theory

Let us first consider the bilayer system composed of fatty alcohol and cationic surfactant in the L_β phase at room temperature and atmospheric pressure. As illustrated on the right side of Fig. 2-1, when the simulated L_β phase (lower right corner) was gradually heated at constant pressure (1 bar), the bilayer turned into an L_α phase (upper right corner) at high temperature as expected. The bilayer in the fluidic L_α phase could be stretched by imposing a negative lateral pressure on the system, as shown on the upper half of Figure 1. With the bilayer in the stretched state with decreased thickness and increased apparent bilayer area, the spontaneous formation of an interdigitated bilayer in $L_{\beta I}$ phase occurred when the system was cooled back to room temperature while maintaining the negative lateral pressure, as shown by the two images on the left side of Fig. 2-1. Finally, changing the lateral pressure back to atmospheric pressure led to a bilayer at the same starting temperature and pressure as in the lower right-hand corner of Fig. 2-1, but in the $L_{\beta I}$ phase instead of the initial L_β phase. The above transitions were found to be "reversible" in the sense that the states at either end of the transition could be recovered one from the other traversing the transition in either direction by varying the system temperature at fixed pressure or the lateral pressure at fixed temperature. This contrasts with the lack of a spontaneous, direct, transition between the L_β and $L_{\beta I}$ phase, both of which remained stable during runs at atmospheric pressure and room temperature. We indicate this in Fig. 2-1 by an "X" over this transition, showing that both states are metastable at atmospheric conditions, although only one of them is the thermodynamically stable state. However, it is theoretically possible to calculate the free energy change along the indirect pathways by thermodynamic integration.

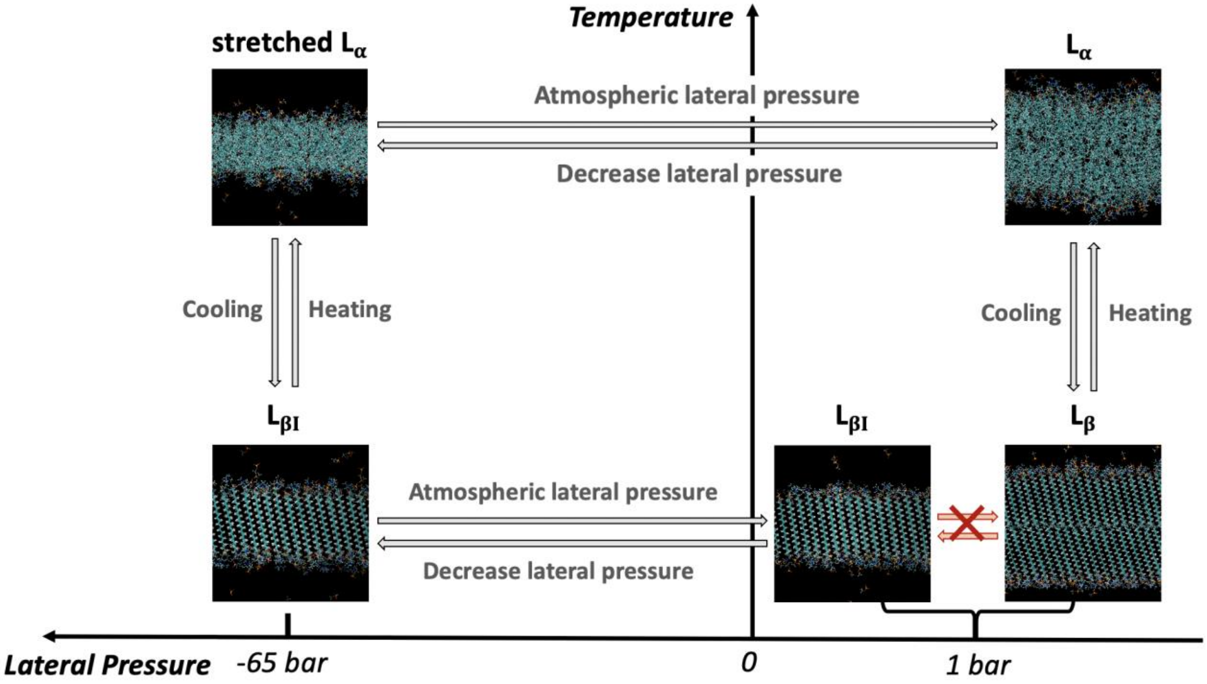

Figure 2-1. Snapshots of different bilayer phases upon changes of temperature or lateral pressure in the x and y directions. The pressure in the z direction perpendicular to the bilayer remains at atmospheric pressure. Water molecules are hidden.

Here, we consider the Helmholtz free energy of F of the system, which is defined as the internal energy U plus the product of temperature T and entropy S. The change of internal energy dU equals the change of heat and work done and can be written as $TdS - pdV$ for a reversible change. (Here we take the pressure to be isotropic for simplicity, but below we generalize to allow for anisotropic pressure, in which lateral pressure in the plane of the bilayer differs from transverse pressure perpendicular to it.) The change of free energy dF is equal to $-SdT - pdV$ in differential form. As the system volume changes reversibly with varying pressure in continuous small steps at constant temperature, the change of free energy ΔF can be calculated from the integral of $-pdV$ as follows:

$$F \equiv U - TS \tag{2.1}$$

$$dU = T\,dS - p\,dV = d(TS) - S\,dT - p\,dV \tag{2.2}$$

$$dF = dU - d(TS) = -S\,dT - p\,dV \tag{2.3}$$

$$\Delta F = -\int p\,dV \ \ for\ constant\ T \tag{2.4}$$

On the other hand, the average internal energy *U* and the thermal average of a generalized force *X* corresponding to an external displacement variable *x* can be expressed in terms of the canonical partition function *Z* and $\beta = \frac{1}{kT}$ to give the differential form of log *Z*. The Helmholtz free energy is also related to the canonical partition function as $F = -\frac{\log Z}{\beta}$. As shown in the following derivation, the change of the ratio of free energy to temperature, $\Delta\left(\frac{F}{T}\right)$, can be written as the integral of the internal energy *U* over the inverse of temperature $d\left(\frac{1}{T}\right)$ plus the integral of a generalized force *X* divided by temperature *T* over the external variable *dx*. Statistical thermodynamics gives the following two identities:

$$U \equiv < E > = -\frac{\partial \log Z}{\partial \beta} \tag{2.5}$$

$$X = \frac{1}{\beta}\frac{\partial \log Z}{\partial x} \tag{2.6}$$

where the derivative with respect to β is taken at fixed x, and that with respect to x is at fixed β. All logarithms are natural logs. We can then obtain from these

$$d(\log Z) = -U\,d\beta + \beta X\,dx \tag{2.7}$$

We also have the identity:

$$F = -\frac{\log Z}{\beta} \tag{2.8}$$

which, when combined with the previous equation of $d(\log Z)$, gives

$$d(F\beta) = d(-\log Z) = U\, d\beta - \beta X\, dx \tag{2.9}$$

Using the definition of $\beta = \frac{1}{kT}$,

$$d\left(\frac{F}{T}\right) = U\, d\left(\frac{1}{T}\right) - \frac{X}{T}\, dx \tag{2.10}$$

which leads to the desired result:

$$\Delta\left(\frac{F}{T}\right) = \int U\, d\left(\frac{1}{T}\right) - \int \frac{X}{T}\, dx \tag{2.11}$$

The generalized force *X* in each direction can be calculated from the anisotropic pressures time the area on each side of the simulation box while the displacement *dx* is just the change of simulation box dimensions. The total energy and temperature are also recorded during simulations. Therefore, the free energy change resulting from varying temperature at constant pressure can be evaluated as well. Based on the above thermodynamic principles, the free energy change can be calculated for two systems starting in same structure (L_{α}) at high temperature and atmospheric pressure after passing through different reversible pathways taking them into two different structures (L_{β} and $L_{\beta I}$) at the same low temperature and atmospheric pressure. As shown in Fig. 2-2, since the starting states are exactly the same and the final states are also at the same temperature and pressure and the pathways are reversible, the difference in free energy change along the two pathways is equal to the free energy difference of their final states, which here are the interdigitated ($L_{\beta I}$) and non- interdigitated bilayer (L_{β}).

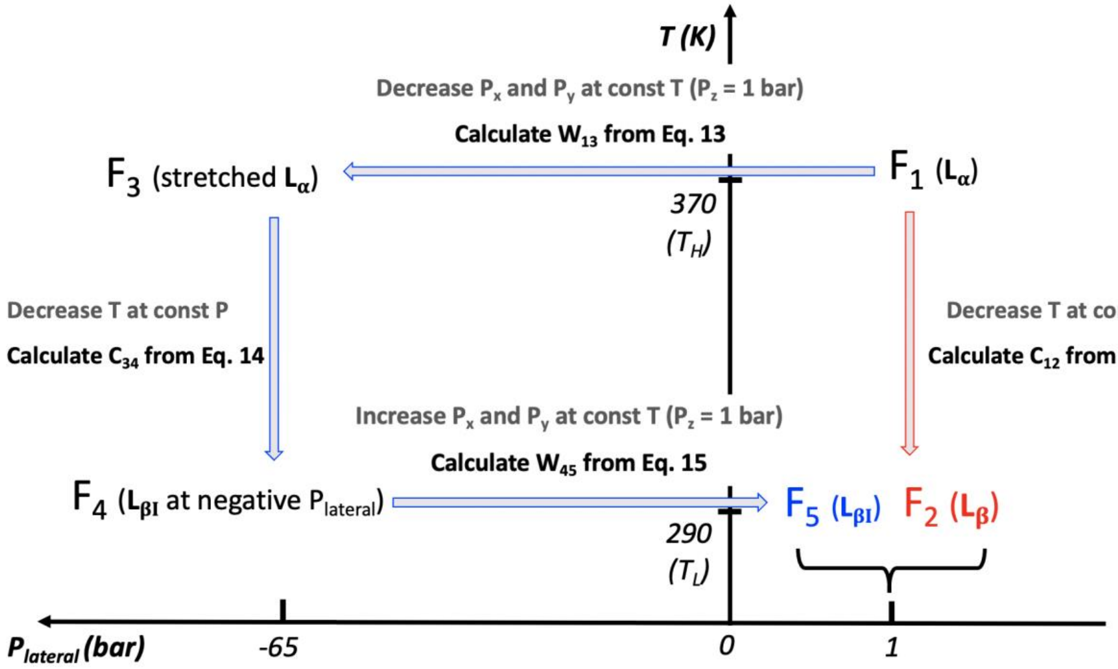

Figure 2-2. Two thermodynamic pathways from the same starting state: F_1, to two different final states, namely, F_2: the non-interdigitated bilayer formed via the red pathway, and F_5: the interdigitated bilayer formed via the blue pathway. Both pathways are at 290 K and atmospheric pressure.

The following four equations (Eqs. 2.12 - 2.15) are derived from the above scheme to relate the unknown free energies of five different states (F_1 to F_5) to quantities (C_1, W_2, C_3, and W_4) that can be calculated from simulation by thermodynamic integration. The anisotropic pressures are P_x, P_y, and P_z and L_x, L_y, and L_z are the simulation box dimensions. After rearrangement, the free energy difference between L_β and $L_{\beta I}$ state can be expressed in terms of all known variables (Eq. 2.16).

$$\frac{F_2}{T_L}-\frac{F_1}{T_H}=\Delta\left(\frac{F}{T}\right)=\int U\,d\left(\frac{1}{T}\right)-\int\frac{P_xL_xL_y\,dL_z+P_yL_xL_z\,dL_y+P_zL_xL_y\,dL_z}{T}=C_{12} \quad (2.12)$$

$$F_3-F_1=\Delta F=-\int P\,dV=\int P_xL_xL_y\,dL_z+P_yL_xL_z\,dL_y+P_zL_xL_y\,dL_z=W_{13} \quad (2.13)$$

$$\frac{F_4}{T_L}-\frac{F_3}{T_H}=\Delta\left(\frac{F}{T}\right)=\int U\,d\left(\frac{1}{T}\right)-\int\frac{P_xL_xL_y\,dL_z+P_yL_xL_z\,dL_y+P_zL_xL_y\,dL_z}{T}=C_{34} \quad (2.14)$$

$$F_5 - F_4 = \Delta F = -\int P\, dV = \int P_x L_x L_y\, dL_z + P_y L_x L_z\, dL_y + P_z L_x L_y\, dL_z = W_{45} \tag{2.15}$$

$$F_5 - F_2 = W_{45} + T_L \left[C_{34} - C_{12} + \frac{W_{13}}{T_H} \right] \tag{2.16}$$

While Eqs. 2.12 - 2.16 apply for general displacements in three dimensions, we restrict our interest to lateral pressure change with semiisotropic pressure coupling in which $dL_x = dL_y$, $P_x = P_y$, and P_z stays at a constant of 1 bar.

2.3 Molecular Dynamics Simulation Methods

2.3.1 Bilayer composition and simulation details

All-atom MD simulations were carried out for bilayers consisting of the cationic surfactant (CS) behentrimonium methylsulfate (BTMS) and the fatty alcohol (FA) stearyl alcohol (C_{18}) as the fatty alcohol (FA) cosurfactant. The simulation system consisted of 46 BTMS, 154 stearyl alcohol to match the CS:FA molar ratio in the experimental sample for rheology characterization and 12000 water molecules. The simulation system has 77 wt% of water, which is reduced from the 93 wt% in the actual industrial application due to the limitation on system size, but the mixed surfactant bilayers are still sufficiently hydrated with large enough lamellar spacing that the water content is not expected to influence the phase transitions.[9] The surfactant and fatty alcohol molecules were packed into the bilayer to create the initial configuration, and then equilibrated at 290 K for at least 40 ns to obtain the gel state structure. The forcefield parameters were adopted from L-OPLS with the rigid SPC/E model for water.[24-26] For NPT simulations, a time step of 1 fs was used. The temperatures of cationic surfactant, fatty alcohol and water were separately controlled by the velocity-rescale coupling method with a time constant of 0.1 ps.[27] Pressure was controlled by the Parrinello-Rahman semi-isotropic coupling method with a time constant of 2.0 ps, which allows the lateral pressure in x and y direction and the pressure in z direction to be set differently.[28] A Verlet neighbor-searching scheme was used and both Coulombic and van der Waals interactions were cut off at 1.2 nm. Long range electrostatic interactions were treated using the particle-mesh Ewald method with an interpolation order of 4 and 0.12 nm Fourier spacing.[29] Periodic boundary conditions were applied in all three directions. System energy, temperature and periodic box dimensions were saved every 10 ps, with results reported here being insensitive to this choice. All simulations were performed with GROMACS 2019.[30, 31]

2.3.2 Variation of temperature and lateral pressure

To control the phase transition, a linear temperature ramp from 290 K to 370 K was imposed with various heating/cooling rates ranging from 2.0 K/ns to 0.25 K/ns. The actual temperature fluctuated somewhat from this linear ramp on short time scales, so that the increase was not strictly monotonic. Therefore, the recorded temperatures and the corresponding total energies were reordered before integrating the total energy over the inverse of temperature. Since pressure could not be changed during a simulation run, separate simulation runs at different lateral pressures were performed to approximate a continuously changing pressure using linear interpolation. The lateral pressure was varied from 1 bar to -65 bar with an interval of 10 bar, each for 20 ns to allow the system to reach equilibrium, and a subsequent 20 ns of sampling to calculate average properties.

2.3.3 Monitoring phase transitions

To monitor structural change in the bilayer, the carbon-hydrogen order parameter of the alkyl chains in the molecules is computed for each carbon along the alkyl chain:

$$S_{CD} = \frac{1}{2}|3\cos^2\theta - 1| \tag{2.17}$$

where θ is the angle between the C-H bond vector and the bilayer normal. This order parameter is averaged over all the carbons of all alkyl chains and used to identify the phase transition of the bilayer, supported by snapshots from the simulation.

2.4 Results and Discussion

2.4.1 Phase transitions

Bilayers with separate leaflets were built as the initial structure and assembled into a bilayer. When the system was equilibrated at 290 K and 1 bar, the bilayer formed a tilted L_β phase shown in the lower right-hand corner of Figure 1 with the alkyl chains hexagonally packed in each leaflet shown in Fig. 2-3(a). As the temperature was increased, at above 355 K the bilayer melted as expected into an L_α phase with much lower order parameter shown in the upper right-hand corner of Fig. 2-1. The packing of alkyl chains in the leaflets also loses the hexagonal order as shown in Fig. 2-3(b). The melting temperature from the simulation is reasonably close to the values of around 340-350 K reported in previous simulations and differential calorimetry (DSC) experimental data of similar systems.[9] The L_β to L_α phase change is reversed upon cooling, although at a lower transition temperature due to hysteresis.

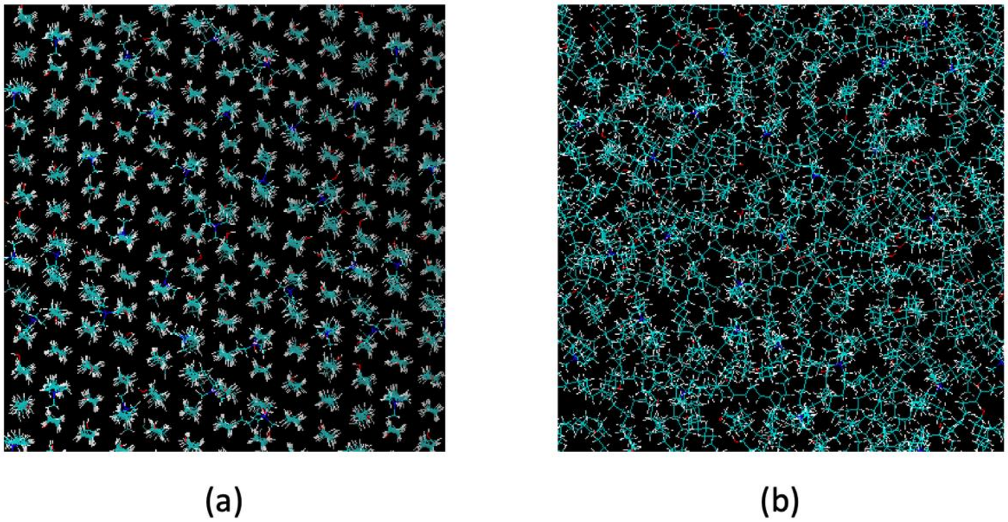

Figure 2-3. *Packing of FA and CS in one leaflet of the bilayer in* ***(a)*** *L_β phase (hexagonal order), and* ***(b)*** *L_α phase (disorder).*

To investigate the formation of the interdigitated $L_{\beta I}$ phase, a negative lateral pressure in the x and y directions was applied to stretch the L_α bilayer at 370 K into a thinner state with the two leaflets penetrating more into each other as shown in the upper half of Fig. 2-1. The average area per molecule in the leaflet increases by 76% from 0.307 nm^2 to 0.540 nm^2 at -65 bar in Fig. 2-4. The order parameter S_{CD} also further decreased from 0.15 of the unstretched state to 0.05 of the stretched state, which can be seen by comparing the endpoints on Figs. 2-6(a) and 2-6(b). The deformation of the bilayer was reversible when the lateral pressure was changed back to 1 bar. Successive cooling of the stretched L_α bilayer at negative lateral pressure could lead to the spontaneous formation of an ordered, interdigitated $L_{\beta I}$ phase as shown on the left side of Fig. 2-1. Afterwards, heating the bilayer in the interdigitated $L_{\beta I}$ phase under negative lateral pressure could bring the bilayer back into the stretched L_α phase. However, a critical lateral pressure between -40 and -50 bar was required for sufficient deformation to induce enough interdigitation. Otherwise, a less stretched L_α bilayer would turn into the non-interdigitated L_β phase upon cooling as shown by the comparison in Fig. 2-10 in the Appendix. The surface tension on the bilayer caused by the stretching is also plotted in Fig. 2-5, which shows that the critical tension value required for the formation of the interdigitated bilayer is around 5 x 10^{-7} N/m. We note that an equivalent way of computing free energy is to control surface tension, rather than lateral pressure. While no pore formation was observed during the bilayer stretching presented in this work, the fluidic L_α bilayer could be prone to rupture if much higher tension is imposed.

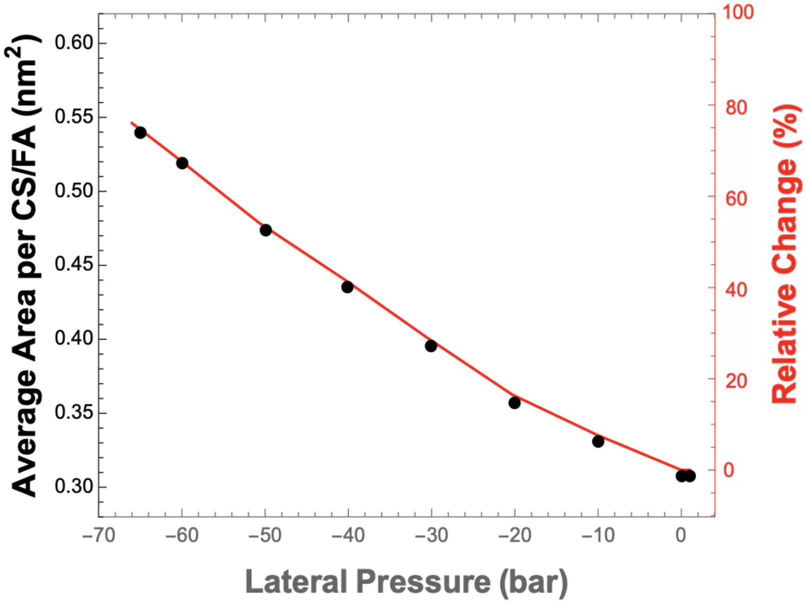

Figure 2-4. Change of average area per CS/FA molecules in each leaflet when the bilayer in the L_α phase is stretched under different negative lateral pressures, in a sequence from right to left from 1 to -65 bar.

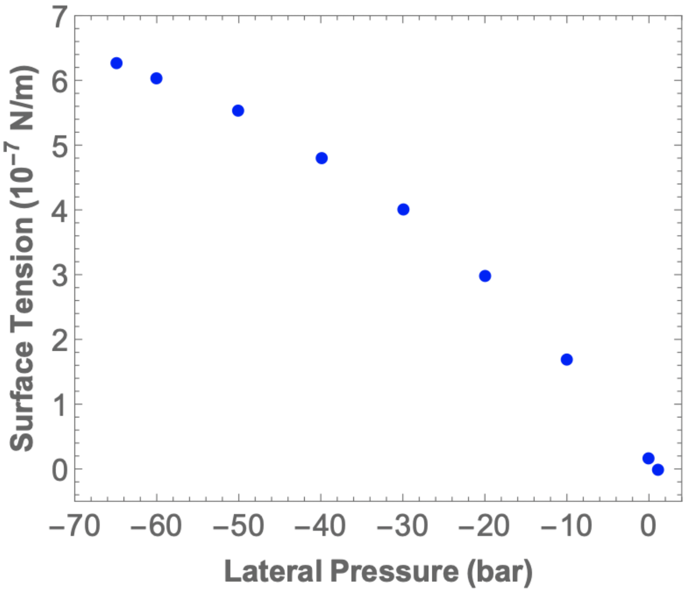

Figure 2-5. Dependence of surface tension on the bilayer to lateral pressure, varied from right to left from 1 to -65 bar.

2.4.2 Thermodynamic integration

With the method proposed, we calculate C_{12} and C_{34} during the temperature change at each of the two fixed pressures and W_{13} and W_{45} during lateral pressure change at the two fixed temperatures, according to Eqs. 2.12 - 2.15. W_{13} and W_{45} are equal to the PV work done if the pressure change is carried out in small steps and the volume change is reversible. In practice, W_{13} and W_{45} were approximated by numerical integration of the PV change and interpolation from a series of simulations at 370 K and 290 K with different lateral pressures. The bilayer in the L_α phase gradually expanded laterally in the x and y directions and shrank in the z direction when the lateral pressure changed from 1 bar to -65 bar with P_z fixed at 1 bar as shown in Fig. 2-16 in the Appendix. Since the absolute value of the lateral pressure was much larger than P_z and the system was expanding against a negative lateral pressure, the free energy increased during the bilayer stretching giving W_{13} = 3.45 kJ/mol, a positive value. In contrast, W_{45} corresponds to a lateral pressure change from -65 bar back to 1 bar on the bilayer system in the rigid $L_{\beta I}$ phase with much less volume change, thus giving a negative and much smaller absolute free energy change, W_{45} = -0.40 kJ/mol.

The calculation of C_{12} and C_{34} by numerical integration of the system energy over increments of inverse temperature is subjective to uncertainties due to hysteresis between cooling and heating. Hysteresis is revealed by a difference in the transition temperature between the high temperature L_α phase and either the L_β or the $L_{\beta I}$ phase upon heating vs. cooling. To investigate the hysteresis effect, both the interdigitated and non-interdigitated systems were heated from 290 K to 370 K and cooled from 370 K to 290 K at different rates of change of temperature. As shown in plots of the order parameter in Fig. 2-6, hysteresis is more significant for cooling especially for the interdigitated bilayer and decreases with slower heating or cooling rates.

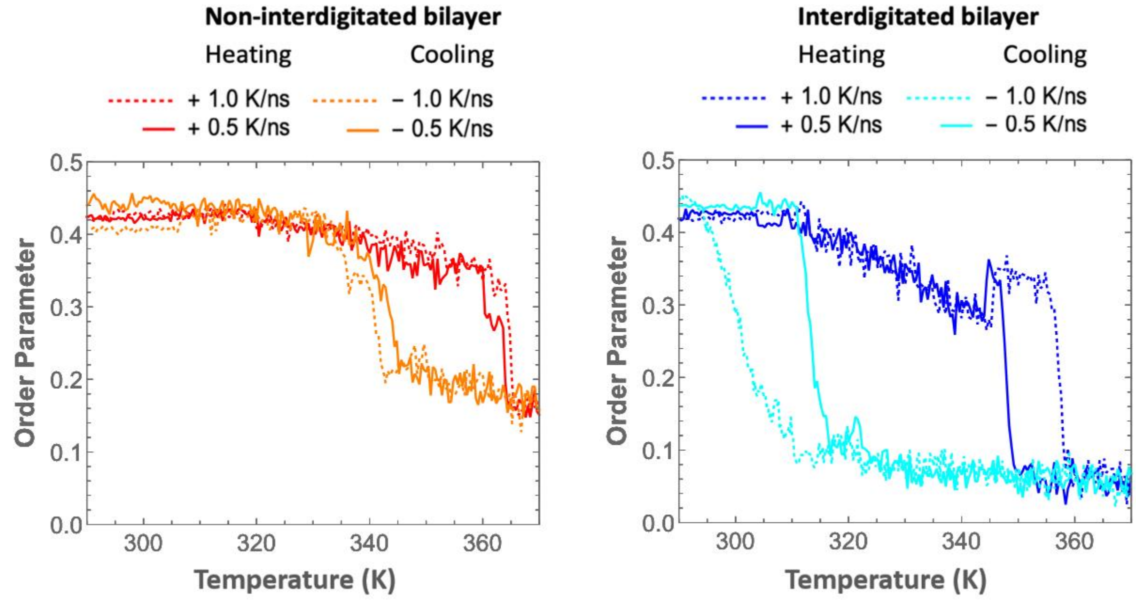

(a) (b)

*Figure 2-6. Hysteresis in change of average order parameter S_{CD} (calculated from Eq. 2.17) of the fatty alcohol molecules during heating and cooling at two different rates for **(a)** transition of non-interdigitated bilayer system between L_α and L_β phases at atmospheric pressure, **(b)** transition of interdigitated bilayer system between stretched L_α and $L_{\beta I}$ phases at -65 bar lateral pressure.*

In theory, hysteresis will be eliminated if the rate of temperature change is made infinitely small, but it remains finite with any finite simulation time. To extrapolate towards an infinitely slow rate, we plot in Fig. 2-7 C_{12} (corresponding to a phase transition in a non-interdigitated bilayer) and C_{34} (corresponding to a phase transition in an interdigitated bilayer under negative lateral pressure) calculated from simulations of heating or cooling at different rates. Ideally, the data points from heating and cooling simulations should converge when extrapolated to an infinitely slow rate of temperature change. For both systems, the data points from heating and cooling do approach each other as the rate of temperature change decreases, and those from heating are less sensitive to the change of heating rate and fit better to a linear extrapolation than those from cooling. This is not surprising, since melting is faster than crystallization and not as susceptible to defect formation. Therefore, data points from the heating simulation should be the more reliable data and were therefore used for our free energy calculations. The extrapolated values of the constants obtained from the four thermodynamic integrations shown in Fig. 2-2 are given in the row of values labeled "$L_{\beta I}$ vs L_{β}" in Table 2-1.

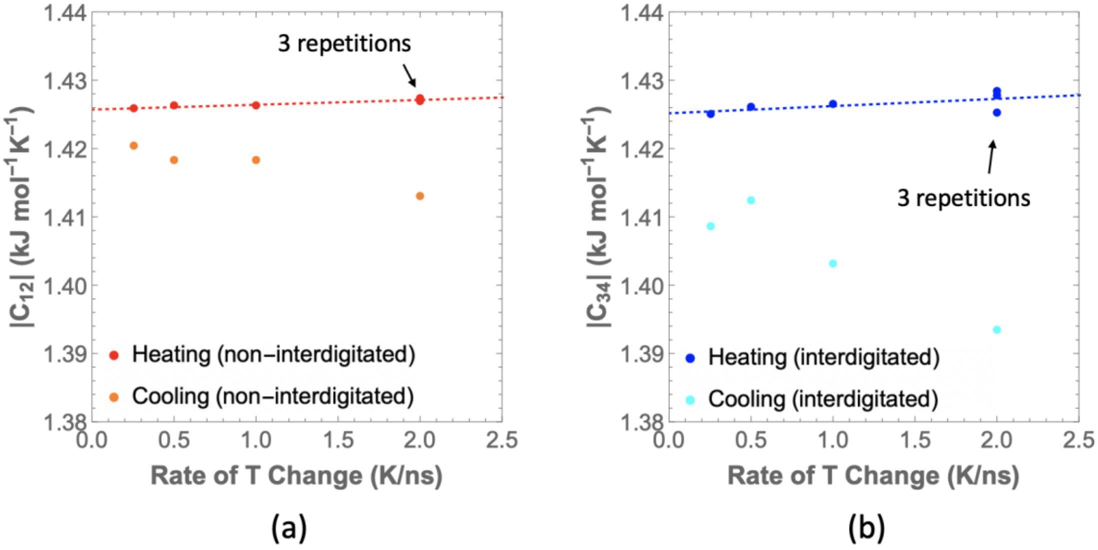

Figure 2-7. Effect of hysteresis on value of ***(a)*** *C_1 for non-interdigitated bilayer, and* ***(b)*** *C_3 for interdigitated bilayer.*

To investigate the potential influence of the lateral density distribution of the two components, bilayers with more homogenously dispersed cationic surfactant molecules were created as shown in Fig. 2-8(b). No significant difference was found in the phase transition temperature or in results from thermodynamic integration (Appendix Fig. 2-11). Since a perfectly "homogenous" bilayer almost never spontaneously forms by cooling of the L_α phase in the simulation, bilayers with randomly dispersed cationic surfactants were used in the simulations in the main text. In addition, a smaller simulation system with 36 molecules in each bilayer leaflet instead of the 100 of the original system with almost the same CS:FA ratio (8 CS and 28 FA) and water content was created to investigate the influence of system size. Heating simulations at 2.0 K/ns and 0.5 K/ns were performed for both the interdigitated bilayer and the non-interdigitated bilayer. The values of C_{12} and C_{34} calculated from the smaller system are very close to the ones from the original system (Appendix Fig. 2-12), proving that the result is not affected by system size. The test with different system size also addresses the concern with non-zero off-diagonal pressure tensors, especially the xy stress distortions. At 290 K, the xy stress is around 2 bar for L_β phase at 1 bar lateral pressure and 19 bar for $L_{\beta I}$ phase at -65 bar lateral pressure, which is caused by the box-induced distortion of the hexagonal phase, and this stress vanishes when the bilayer turns into an L_α phase at high temperature. Since non-zero shear stresses will get smaller for bigger systems, the fact that both systems give similar results indicates that the bias in pressure does not change the main results of the paper.

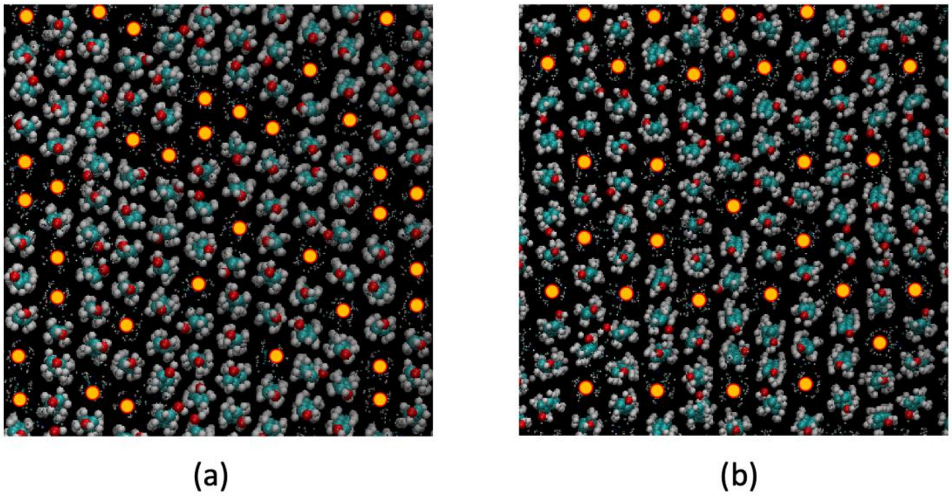

Figure 2-8. Lateral distribution of FA and CS hexagonally packed in one leaflet of the bilayer in L_β phase: ***(a)*** *with random dispersion of CS,* ***(b)*** *with artificially created more homogenous dispersion of CS. CS molecules are highlighted with orange circles.*

Based on the proposed method, the free energy difference between $L_{\beta I}$ and L_β phases at 290 K, and atmospheric pressure, was calculated to be 2.4 kJ/mol of surfactant and fatty alcohol. The major source of error comes from the extrapolation of C_{12} and C_{34} from linear regression, where the 95% confidence interval produces an uncertainty of ± 0.5 kJ/mol. The positive free energy difference indicates that the bilayer with an L_β structure has the lower free energy and is more stable. The result agrees with the spontaneous formation of non-interdigitated bilayer observed in simulation.

2.4.3 Verification with thermodynamic cycles

To further verify the proposed method, two thermodynamic cycles were constructed, one for a non-interdigitated bilayer and the other for an interdigitated bilayer at different negative lateral pressures as illustrated in Fig. 2-9. In the previous case, a difference in free energy change resulted from the two pathways from the same starting state, since the pathways led to two different final states, namely L_β and $L_{\beta I}$ phases. In the two new cycles presented in Fig. 2-9, the same starting states transition to the same final states via two different pathways and therefore the theoretical difference between the two pathways of each system should be zero.

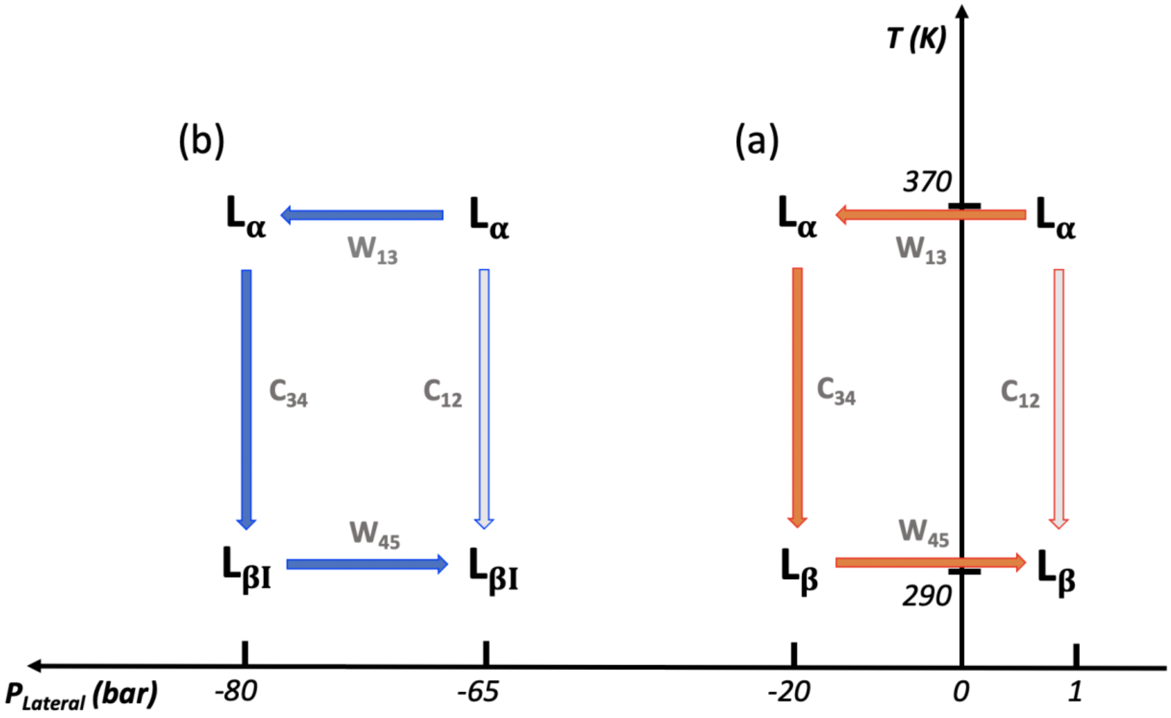

Figure 2-9. Thermodynamic cycles for ***(a)*** *non-interdigitated bilayer, and* ***(b)*** *interdigitated bilayer. Solid and hollow arrows are different thermodynamic pathways connecting the same starting and final states.*

The same method as used above was also used for free energy calculations in heating simulations, although the extrapolation of C_{34} was based on three different heating rates instead of four (Appendix Fig. 2-13). The two cycles in Figs. 2-9(a) and 2-9(b) converged with errors of 0.3 and 0.4 kJ/mol respectively from Table 1, which is within the estimated systematic error. These simulations indicate that our method of computing free energy differences between namely $L_{\beta I}$ and L_β phases using these thermodynamic cycles is valid and has error well below the calculated free energy difference.

Table 2-1. Calculated values for C_{12}, W_{13}, C_{34}, and W_{45}, each multiplied by temperature or temperature ratio used in calculating the free energy difference between the $L_{\beta I}$ and L_{β} phases and in the two constructed thermodynamic cycles.

$\Delta F = W_{45} + T_L \left[C_{34} - C_{12} + \frac{W_{13}}{T_H} \right]$ unit: kJ/mol					
System	$- C_{12} * T_L$	$W_{13} * T_L/T_H$	$C_{34} * T_L$	W_{45}	ΔF
$L_{\beta I}$ vs L_{β}	413.45	2.704	- 413.31	- 0.40	**2.44**
Cycle (a)	413.45	0.203	- 413.96	- 0.029	**- 0.34**
Cycle (b)	413.31	0.972	- 414.55	- 0.122	**- 0.39**

2.4.4 Discussion

The major contribution of the excess free energy difference between the $L_{\beta I}$ phase and the L_{β} phase comes from the PV work (W_{13}) during stretching of the bilayer in the L_{α} phase. This is because the free energy change from the L_{α} to L_{β} phase and from the stretched L_{α} to $L_{\beta I}$ phase under negative lateral pressure almost cancel each other as shown in the first row of numerical values in Table 2-1. For the interdigitated bilayer to be the favored structure, the free energy of the $L_{\beta I}$ phase minus that of the L_{β} phase should be negative. This would require a smaller positive PV work during stretching (W_{13}) of the L_{α} phase and a larger free energy reduction upon turning the L_{α} phase into the $L_{\beta I}$ phase on cooling (C_{34}). The contribution of the entropy to the free energy difference can also be determined. The difference of internal energy is readily found from the simulation to be 3.05 kJ/mol. Using $\Delta F = \Delta U - T\Delta S$, the entropy difference of the $L_{\beta I}$ phase over that of the L_{β} phase is computed to be 2.2 J/(mol K) at 290 K. The higher entropy of the interdigitated bilayer might be explained by the various ways the molecules from each leaflet can interpenetrate into the other leaflet in the bilayer.

2.5 Conclusion and Future Directions

Using MD simulations of bilayers of fatty alcohol and cationic surfactant, we induced the formation of an interdigitated $L_{\beta I}$ bilayer from a non-interdigitated L_{β} phase, by 1) heating the L_{β} phase into an L_{α} phase, then 2) stretching the L_{α} bilayer using negative lateral pressure to induce interdigitation, and then 3) cooling to a lower temperature at which the $L_{\beta I}$ phase formed. By thermodynamic integration, the free energy changes of each of these transformations were computed, although the third of these free energy changes were found to be more accurately determined by heating from the $L_{\beta I}$ phase rather than the reverse. Both interpolation and extrapolation to zero heating rates were used in the free energy calculations to approximate the true equilibrium properties and two additional thermodynamic cycles designed to produce zero net free energy change were constructed to provide negative control, thus verifying the method. The free energy of the $L_{\beta I}$ phase was found to be 2.4 ± 0.5 kJ/mol higher than that of L_{β} phase, which is consistent with the spontaneous formation of the L_{β} phase under atmospheric pressure in simulations of cooling from the L_{α} phase. To further improve the method, performing long simulations at different temperatures and using interpolation in between could be an alternative way to obtain the energy-temperature curve for thermodynamic integration and could be compared with the current approach. Using a different forcefield may also provide a better result although the forcefield gives a phase transition temperature of around 350-355 K, which is only 5-10 K higher than the experimental one. It would also be worthwhile to apply our method to other bilayer systems, especially those that experimentally show interdigitation to gain a better understanding of the molecular requirements needed for interdigitation. We also note that there may be other solid-solid phase transitions in lamellar geometries for which lateral pressure might be used to determine relative phase stability.

2.6 Appendix

Supporting information includes figures showing the non-interdigitated and the interdigitated bilayer formed upon cooling at different lateral pressures, a comparison of results from the main paper with those from a smaller system and from a system with "homogenously" dispersed surfactant with the original system, and the results of thermodynamic integration of two thermodynamic cycles.

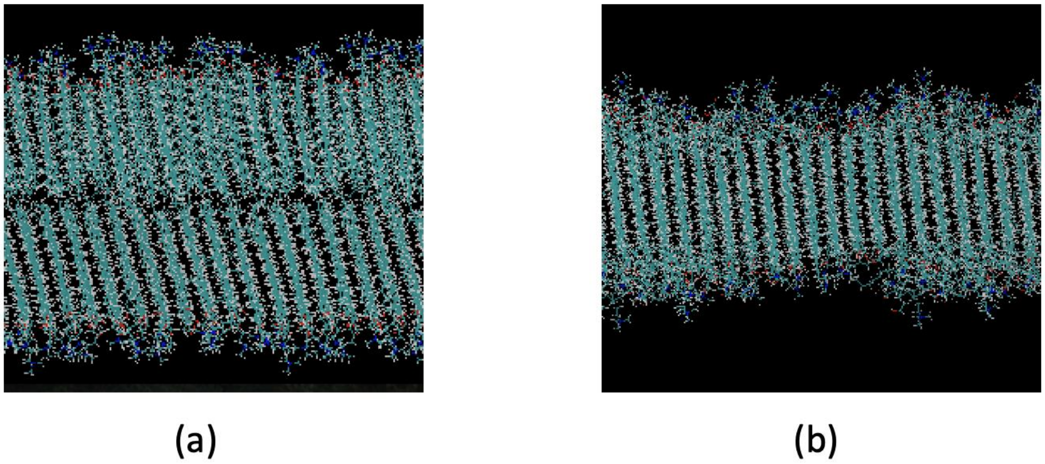

Figure 2-10. Snapshots of ***(a)*** *non-interdigitated bilayer formed upon cooling at -40 bar lateral pressure, and* ***(b)*** *interdigitated bilayer formed upon cooling at -50 bar lateral pressure.*

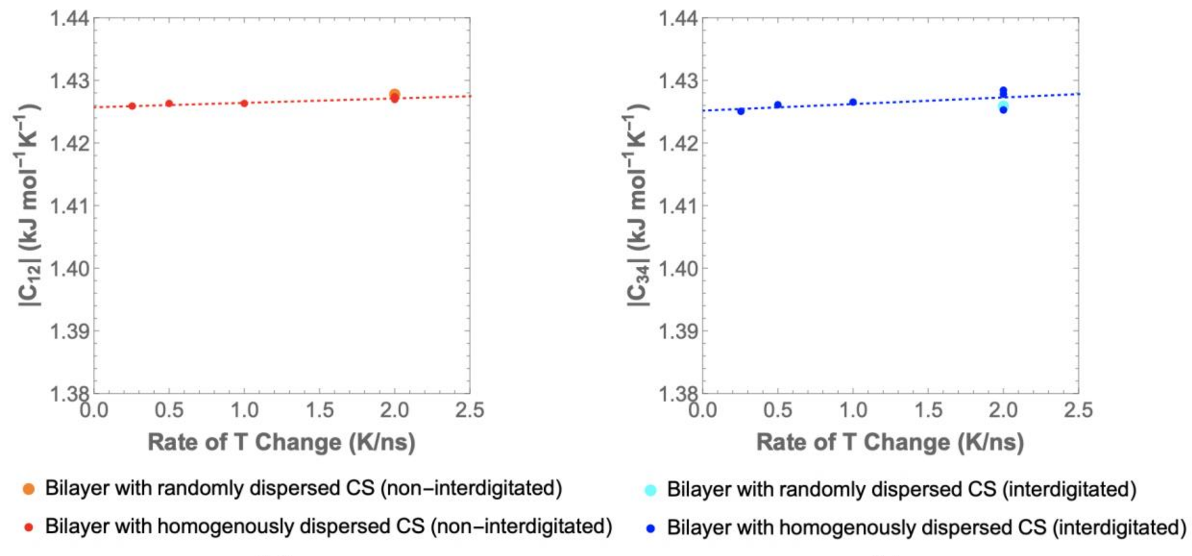

(a) (b)

Figure 2-11. Comparison between systems with randomly dispersed CS and "homogeneously" dispersed CS at 2.0 K/ns heating rate for ***(a)*** *C_{12} for the non-interdigitated bilayer, and* ***(b)*** *C_{34} for the interdigitated bilayer.*

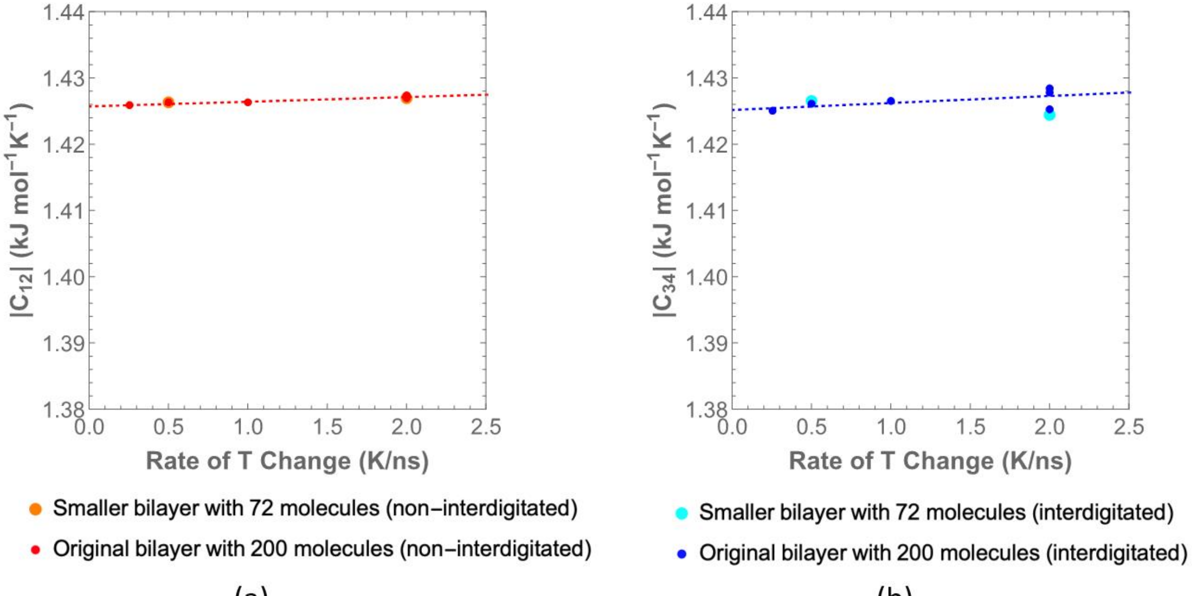

(a) (b)

Figure 2-12. Comparison between results from a smaller system and the original system at 2.0 and 0.5 K/ns heating rates for ***(a)*** *C_{12} for the non-interdigitated bilayer, and* ***(b)*** *C_{34} for the interdigitated bilayer.*

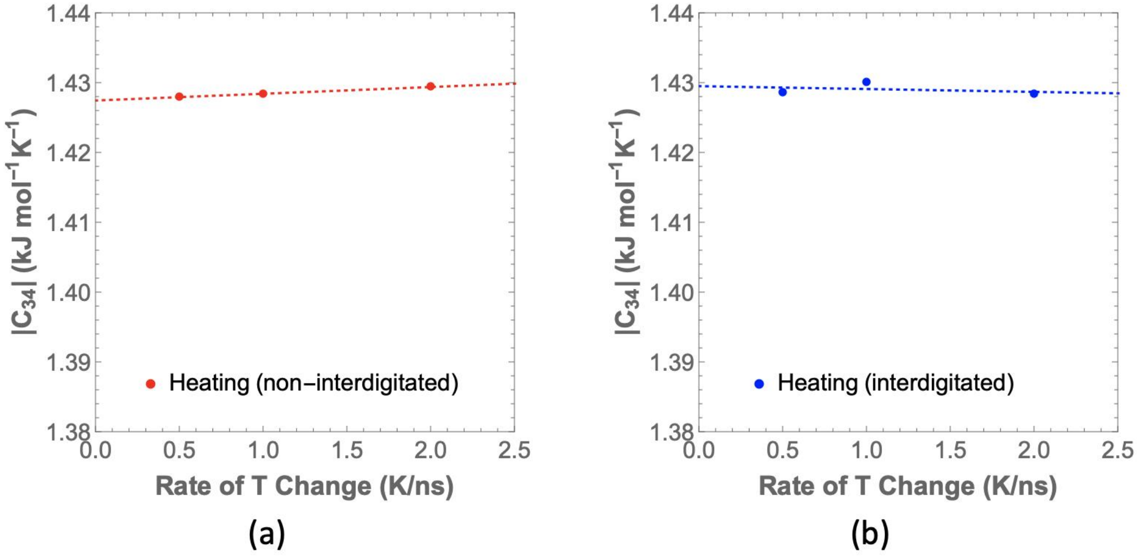

Figure 2-13. Extrapolation to calculate C_{34} for thermodynamic cycle between lateral pressures of ***(a)*** *1 bar and -20 bar for non-interdigitated bilayer, and* ***(b)*** *-65 bar and -80 bar for interdigitated bilayer.*

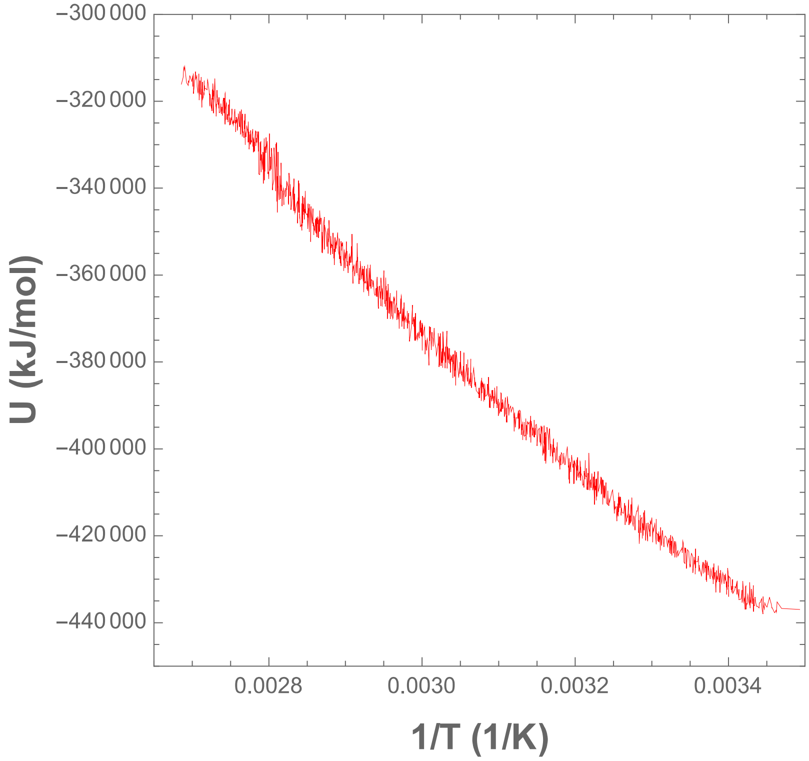

Figure 2-14. U vs (1/T) for heating non-interdigitated bilayer at 1 bar lateral pressure at 0.25 K/ns.

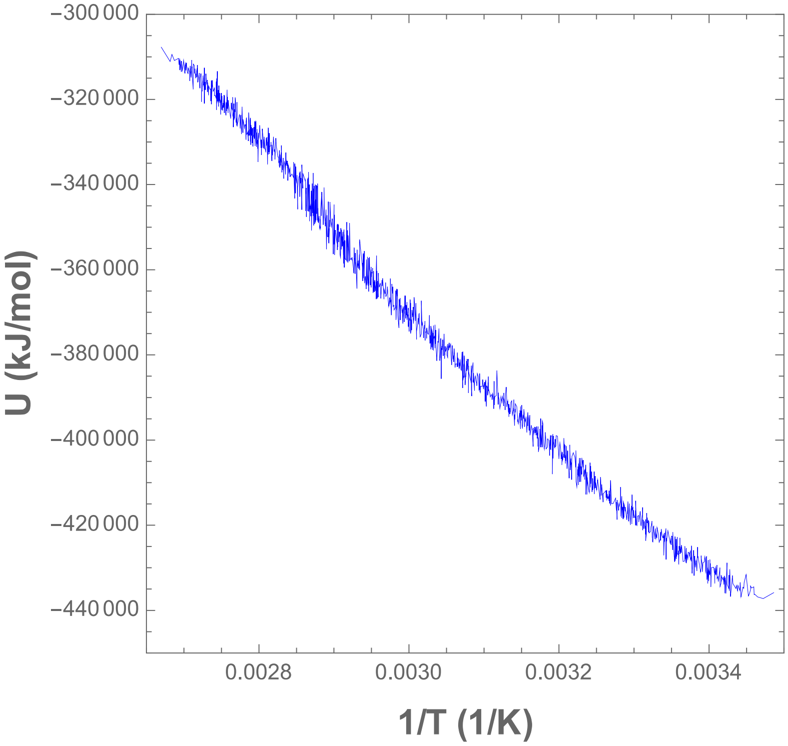

Figure 2-15. U vs (1/T) for heating interdigitated bilayer at -65 bar lateral pressure at 0.25 K/ns.

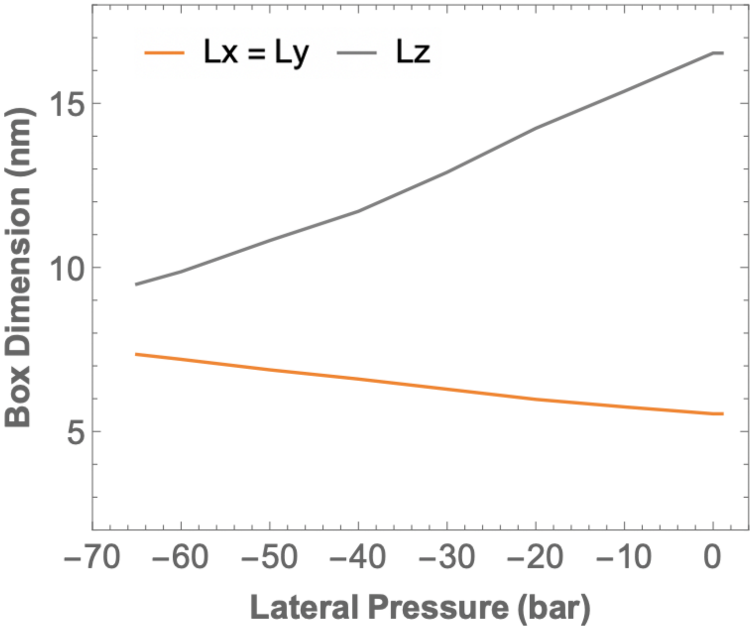

Figure 2-16. Change of periodic box dimensions when the bilayer in the L_α *phase is stretched by changing lateral pressures from right to left from 1 to -65 bar at 370 K with* P_z *held at 1 bar.*

Table 2-2. Calculated values for C_{12}, W_{13}, C_{34}, and W_{45} used in calculating the free energy difference between the $L_{\beta I}$ and L_{β} phases and in the two constructed thermodynamic cycles.

System	C_{12} (kJ/mol K)	W_{13} (kJ/mol)	C_{34} (kJ/mol K)	W_{45} (kJ/mol)
$L_{\beta I}$ vs L_{β}	- 1.4257	3.45	- 1.4252	- 0.40
Cycle (a)	- 1.4257	0.26	- 1.4274	- 0.029
Cycle (b)	- 1.4252	1.24	- 1.4295	- 0.122

2.7 Reference

[1] Fukushima, S., Yamaguchi, M., & Harusawa, F. (1977). Effect of cetostearyl alcohol on stabilization of oil-in-water emulsion: II. Relation between crystal form of the alcohol and stability of the emulsion. *Journal of Colloid and Interface Science, 59*(1), 159-165. https://doi.org/10.1016/0021-9797(77)90350-2

[2] Barry, B. W., & Saunders, G. M. (1970). The Self-bodying action of the mixed emulsifier cetrimide/cetostearyl alcohol. *Journal of Colloid and Interface Science, 34*(2), 300–315. https://doi.org/10.1016/0021-9797(70)90182-7

[3] Laba, D. (1993). *Rheological properties of cosmetics and toiletries*. Routledge. https://doi.org/10.1201/9780203740651

[4] Barry, B. W., & Eccleston, G. M. (1973). Influence of gel networks in controlling consistency of O/W emulsions stabilized by mixed emulsifiers. *Journal of Texture Studies, 4*(1), 53–81. https://doi.org/10.1111/j.1745-4603.1973.tb00654.x

[5] Iwata, T. (2017). Lamellar gel network. In K. Sakamoto, R. Lochhead, H. Maibach & Y. Yamashita (Eds), *Cosmetic science and technology: Theoretical principles and applications* (pp. 415-447). Elsevier.

[6] Datta, A., Tanmay, V. S., Tan, G. X., Reynolds, G. W., Jamadagni, S. N., & Larson, G. (2020) Characterizing the rheology, slip and velocity profiles of lamellar gel networks. *Journal of Rheology, 64*(4), 851-862. https://doi.org/10.1122/8.0000011

[7] Larson, R. G. (1998). *The structure and rheology of complex fluids.* Oxford University Press.

[8] Dubois, M., Zemb, T., Belloni, L., Delville, A. D. P., Levitz, P., & Setton, R. (1992). Osmotic pressure and salt exclusion in electrostatically swollen lamellar phases. *The Journal of Chemical Physics, 96*(3), 2278–2286. https://doi.org/10.1063/1.462078

[9] Debnath, A., Ayappa, K. G., Kumaran, V., & Maiti, P. K. (2009). The influence of bilayer composition on the gel to liquid crystalline transition. *The Journal of Physical Chemistry B, 113*(31), 10660–10668. https://doi.org/10.1021/jp901551d

[10] Tiddy, G. J. T. (1980). Surfactant-water liquid crystal phases. *Physics Reports, 57*(1), 1–46. https://doi.org/10.1016/0370-1573(80)90041-1

[11] Quinn, P. J., Chapman, D., & Keith, A. D. (1980). The dynamics of membrane structure. *Critical Reviews in Biochemistry, 8*(1), 1–117. https://doi.org/10.3109/10409238009105466

[12] Smith, E. A., & Dea, P. K. (2015). The interdigitated gel phase in mixtures of cationic and zwitterionic phospholipids. *Biophysical Chemistry, 196*, 86–91. https://doi.org/10.1016/j.bpc.2014.10.003

[13] Barry, M. D., & Rowe, R. C. (1989). The characterisation by small-angle X-ray scattering of a pharmaceutical gel with a lamellar structure. *International Journal of Pharmaceutics, 53*(2), 139-143. https://doi.org/10.1016/0378-5173(89)90237-8

[14] Eccleston, G. M., Behan-Martin, M. K., Jones, G. R., & Towns-Andrews, E. (2000). Synchrotron X-ray investigations into the lamellar gel phase formed in pharmaceutical creams prepared with cetrimide and fatty alcohols. *International Journal of Pharmaceutics, 203*(1-2), 127– 139. https://doi.org/10.1016/S0378-5173(00)00447-6

[15] Naumann, C., Brumm, T., & Bayerl, T. M. (1992). Phase transition behavior of single phosphatidylcholine bilayers on a solid spherical support studied by DSC, NMR and FT-IR. *Biophysical Journal, 63*(5), 1314–1319. https://doi.org/10.1016/S0006-3495(92)81708-3

[16] Shigematsu, T., Koshiyama, K., & Wada, S. (2018). Stretch-induced interdigitation of a phospholipid/cholesterol bilayer. *The Journal of Physical Chemistry B, 122*(9), 2556-2563. http://doi.org/10.1021/acs.jpcb.7b10633

[17] Laner, M., Horta, B. A. C., & Hünenberger, P. H. (2014). Effect of the cosolutes trehalose and methanol on the equilibrium and phase-transition properties of glycerol-monopalmitate lipid bilayers investigated using molecular dynamics simulations. *European Biophysics Journal, 43*(10–11), 517–544. https://doi.org/10.1007/s00249-014-0982-9

[18] Laner, M., & Hünenberger, P. H. (2015). Effect of methanol on the phase-transition properties of glycerol-monopalmitate lipid bilayers investigated using molecular dynamics

simulations: In quest of the biphasic effect. *Journal of Molecular Graphics and Modelling, 55*, 85–104. https://doi.org/10.1016/j.jmgm.2014.10.017

[19] Kranenburg, M., Vlaar, M., Smit, B. (2004). Simulating induced interdigitation in membranes. *Biophysical Journal, 87*(3), 1596-1605. https://doi.org/10.1529/biophysj.104.045005

[20] Lu, T., & Guo, H. (2018). Phase behavior of lipid bilayers: A dissipative particle dynamics simulation study. *Advanced Theory and Simulations, 1*, 1800013. http://doi.org/10.1002/adts.201800013

[21] Seo, S., Murata, M., Shinoda, W. (2020). Pivot role of interdigitation in interleaflet interactions: Implications from molecular dynamics simulations. *The Journal of Physical Chemistry Letters, 11*(13), 5171-5176. https://doi.org/10.1021/acs.jpclett.0c01317

[22] Lunkad, R., Srivastava, A., & Debnath, A. (2017). Influence of water concentrations on the phase transformation of a model surfactant/co-surfactant/water system. *Chemical Physics, 483–484*, 103–111. https://doi.org/10.1016/j.chemphys.2016.11.014

[23] De Oliveira, T. E., Leonforte, F., Nicolas-Morgantini, L., Fameau, A. L., Querleux, B., Thalmann, F., & Marques, C. M. (2020). Fluid bilayer phase in aqueous mixtures of fatty alcohol and cationic surfactant. *Physical Review Research, 2*(1), 013075. https://doi.org/10.1103/PhysRevResearch.2.013075

[24] Jorgensen, W. L., Maxwell, D. S., & Tirado-Rives, J. (1996). Development and testing of the OPLS all-atom force field on conformational energetics and properties of organic liquids. *Journal of the America Chemical Society, 118*, 11225– 11236. https://doi.org/10.1021/ja9621760

[25] Siu, S. W. I., Pluhackova, K., Böckmann, R. A. (2012). Optimization of the OPLS-AA force field for long hydrocarbons. *Journal of Chemical Theories and Computation, 8*(4), 1459-1470. https://doi.org/10.1021/ct200908r

[26] Zangi, R. (2018). Refinement of the OPLSAA Force-Field for Liquid Alcohols. *ACS Omega, 3*(12), 18089–18099. https://doi.org/10.1021/acsomega.8b03132

[27] Bussi, G., Donadio, D., Parrinello, M. (2007). Canonical sampling through velocity rescaling. *The Journal of Chemical Physics, 126*(1), 014101. https://doi.org/10.1063/1.2408420

[28] Parrinello, R., Rahman, A. (1981). Polymorphic transitions in single crystals: A new molecular dynamics method. *Journal of Applied Physics, 52*(12), 7182. https://doi.org/10.1063/1.328693

[29] Darton, T., York, D., Pedersen, L. (1993). Particle mesh Ewald: An $N \cdot \log(N)$ method for Ewald sums in large systems. *The Journal of Chemical Physics, 98*(12), 10089. https://doi.org/10.1063/1.464397

[30] Berendsen, H. J. C., van der Spoel, D., & van Drunen, R. (1995). GROMACS: A message-passing parallel molecular dynamics implementation. *Computer Physics Communications, 91*(1-3), 43–56.

https://doi.org/10.1016/0010-4655(95)00042-E

[31] Abraham, M., Murtola, T., Schulz, R., Páll, S., Smith, J. C., Hess, B., Lindaul, E. (2015). GROMACS: High performance molecular simulations through multi-level parallelism from laptops to supercomputers. *SoftwareX, 1*(2), 19-25. https://doi.org/10.1016/j.softx.2015.06.001

Chapter 3 Thixotropic Constitutive Modeling of Shear Banding by Boundary-Induced Modulus Gradient in Lamellar Gel Networks

This Chapter is based on the previously published article listed below:

Wang, F., & Larson, R. G. (2023). Thixotropic Constitutive Modeling of Shear Banding by Boundary-Induced Modulus Gradient in Lamellar Gel Networks. *J. Rheol.*, 67, 35.

The experiment data referred in this Chapter is from a published article with permission.[1]

3.1 Introduction

Thixotropic fluids, characterized by a slow, time-dependent, at least partially reversible, reduction in viscosity during flow, often show a yield stress and at least some viscoelasticity.[2,3] Such fluids are very common, and include blood,[4] paints,[5] adhesives,[6] concrete,[7] personal care products,[8,9] waxy crude oils,[10] food materials,[11-13] and weakly flocculated colloidal suspensions.[14-18] It is a challenging task to develop accurate constitutive equations to describe their complex rheology, but these are needed to model their behavior in processing flows, and in the hands of the consumer. Measuring and describing their rheological behavior accurately remains an outstanding challenge in the field of soft matter.

While suspensions of weakly associating particles are the most commonly discussed class of thixotropic materials, an interesting and important additional class is that of aqueous surfactant emulsions known as "lamellar gel networks." These usually contain an ionic surfactant mixed with fatty alcohol as co-surfactant and form emulsions in excess water that contain extended and highly interconnected networks of bilayers which can withstand elastic deformation and have complex flow properties.[19] These lamellar gels are prepared by mixing surfactant and fatty alcohols in the molten state with water at high temperature; upon cooling to room temperature, the mixture transforms locally into so-called L_β bilayers whose alkyl chains are in trans conformation and packed hexagonally in the plane of the lamellae.[20] Macroscopically, the lamellar layers are randomly oriented and interconnected, resulting in a material with the properties of a gel with modulus of order 1000 Pa.[1] As a result of the multiphase structure, these pseudo-ternary mixtures have an opaque creamy appearance and exhibit highly viscous, shear-thinning rheology.[20] Lamellar gels are widely used in pharmaceutical and cosmetic creams and lotions that frequently contain other essential additives such as salt and perfume. Recently, Datta et al. conducted a comprehensive rheological characterization of lamellar gel networks composed of behentrimonium methosulfate (BTMS), cetostearyl alcohol, and water, which is a typical formulation for hair conditioner products. As shown in Fig. 3-1, these materials exhibit a highly shear-thinning viscosity with unique hysteresis in up- and down-ramps of shear rate as the gel “remembers” the maximum shear it had experienced for around 12 hours before it heals and recovers its original viscosity.[1] The hysteresis and the very slow recovery indicate level of internal structure that changes over time scales longer than that of the normal thixotropic response.

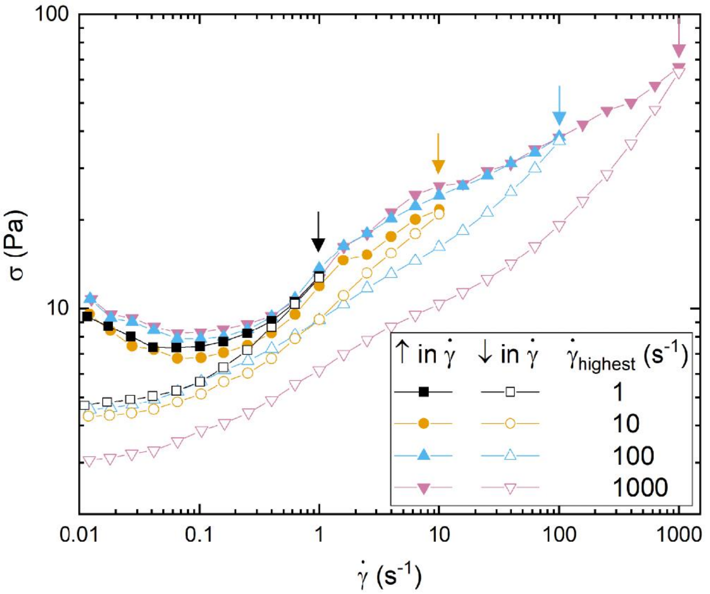

Figure 3-1. Effect of the highest shear rate, $\dot{\gamma}_{highest}$, on hysteresis loops for an experimental lamellar gel sample (Reproduced from [1], with the permission of AIP Publishing). Note that each hysteresis loop is carried out on a separately loaded sample.

Another major feature of these materials is the presence of flow inhomogeneities including fracture planes and shear bands revealed by particle image velocimetry (PIV). Under a constant shear rate, shear banding develops from an initially linear velocity profile shown in Fig. 3-2(a), which transitions into a plug flow with most of the shearing concentrated in a very thin boundary layer adjacent to each plate of the rheometer, as shown in Fig. 3-2(b). Other rheological characteristics include a "solid-like" weak power-law creep response up to a critical strain followed by a fluid-like response, a sluggish power-law stress decay after step-strain experiments, and high storage modulus relative to loss modulus over a wide range of frequencies in small amplitude oscillatory flow.[1] The material shows a nearly elastic response to small deformations and thus has similarity to a "soft glassy" material.[1] In addition, the rheology was found to be gap-dependent, displaying some characteristics of solid-like friction.[1]

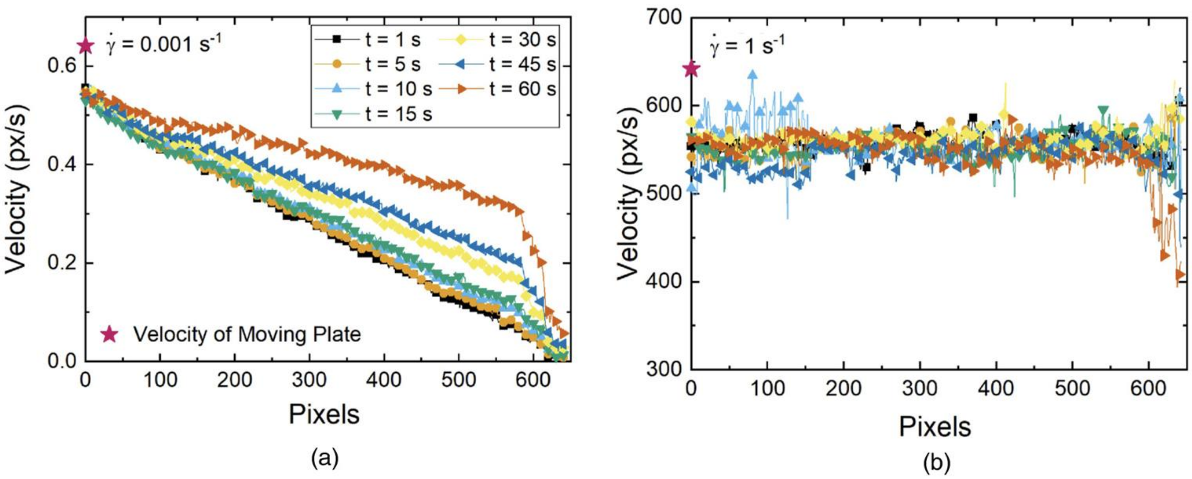

(a)

(b)

Figure 3-2. Velocity variation across the gap at different times after startup of steady shearing at ***(a)*** *0.001 s^{-1},* ***(b)*** *1 s^{-1} (Reproduced from [1], with the permission of AIP Publishing). Pixel 0 is at the position of the moving bottom plate of the rheometer and Pixel 642 is at the position of the stationary top plate with each pixel corresponding to an interval of 0.687 μm.*

Many theoretical efforts have been made in the field to predict the rheological behavior of thixotropic fluids and their shear banding phenomena.[21-24] For example, structure kinetic models are a class of phenomenological based model developed to qualitatively capture the key rheological behaviors of such materials. In these minimal models, rheological parameters such as viscosity are taken to be functions of a structure parameter (usually represented by λ) with unclear microstructural basis, but whose behavior under flow is taken to be governed by a phenomenological kinetic equation. This equation is in general composed of a break-down/rejuvenation term caused by flow and a build-up/aging term describing restoration of structure towards its rest state. Coussat et al. proposed a rather simple model of this type to study the so-called "viscosity bifurcation" in thixotropic, yielding fluids.[25] Their model was later modified by Jain et al. to analyze the transient dynamics in plane Couette flow including the effect of inertia during start-up shear.[26] In the model of Wei et al., λ ranges between 0 and 1 and is decomposed into multiple modes to predict the stretched exponential response in transient shear flows.[27,28] In all such models, the equation for λ is supplemented with an expression for the stress in terms of λ and other parameters, one version of which includes isotropic kinematic hardening. Besides the phenomenological structural kinetic models, there are also ones developed through more physically based argument, an example of which is the well-known soft glassy rheology (SGR) model.[29,30]

Lamellar gel networks, while displaying some properties consistent with these existing models in terms of thixotropy and shear banding, also exhibit distinctive behavior, especially the plug-like flow velocity profile (in Fig. 3-2(b)), which is not well described by a conventional shear banding model. In lamellar gels, the fast-shearing zone near the stationary plate (which is on the right side of Figs. 3-2(a) & 3-2(b)) is more prominent than that along the moving boundary, which is the opposite of the behavior found of a structural kinetic model with inertia.[26] Moreover, the stress that accompanies shear banding increases with apparent shear rate (see Fig. 3-1), while the fast-shearing band remains thin. This too is contrary to the predictions from several structural kinetic models and the experimental observations of other typical thixotropic fluids for which the width of the flowing band increases across the entire gap with increasing imposed shear rate according to a lever rule, until a critical shear rate is reached above which the flow becomes homogeneous.[31,32] These crucial differences from the predictions of established models necessitate the development of a new 1D constitutive model with new features that enable it to describe both the apparent rheology and the velocity profile of lamellar gel networks properly. Such a model could ultimately help improve the modeling of the processing, storage, and consumer experience of commercial products. To serve this practical function, however, the model needs to be kept simple and general while capturing the distinguishing properties of these complex materials at least qualitatively.

3.2 Proposed Model

3.2.1 Strain-dependent elasticity

At the microstructural level, a lamellar gel is a mesoscopically disordered L_β smectic (i.e., lamellar) phase, with randomized lamellar orientation at the mesoscopic and macroscopic levels. The L_β structure implies that the lamellar layers are soft solids, able to be bent and fused together, forming a network typically containing around 90% water. The closest microstructural physical theories for such a material are liquid crystalline theories for nematics and smectics, such as those covered in a monograph by de Gennes.[33] While the physics of well-ordered nematic and smectic liquid crystals are quite well understood, the rheological behavior of orientationally disordered liquid crystals is much more challenging to describe. The only complete nonlinear rheological model for such a material is that of Doi and Larson for mesoscopically disordered nematics.[34] This theory, while successful in describing steady and start-up shearing flows of polymeric nematics, is not directly applicable to lamellar gels, because the latter are smectic, rather than nematic, and, unlike L_α smectics for which the lamellar sheets are disordered and two-dimensionally fluid, L_β sheets are two dimensional solids. Thus, prior to yield, a lamellar gel is a soft solid whose microstructure consists of anisotropic regions describable by an orientation-dependent modulus, which in general is a fourth rank tensor. Although the lamellar in-plane isotropy reduces the number of independent components of this tensor, the absence of any measurements of orientation-dependent modulus on monodomains of a lamellar gel render a description at this level of detail useless for present purposes.

While the above situation suggests pursuit of a purely phenomenological approach, the rheological behavior of lamellar gels, reviewed briefly above, is sufficiently different from other classes of thixotropic or plastic materials (owing to the anisotropic microstructure), that a novel phenomenological model is required for an even qualitative description. To ascertain the form the phenomenology should take, we can appeal to general principles of anisotropic material response to deformation. In particular, an axisymmetric object, whether rod-like or plate-like, whose axis of symmetry is defined by a director (i.e., a unit vector) $\boldsymbol{n}$, responds to flow according to the following equation[35]

$$\frac{\partial}{\partial t}\boldsymbol{n} = \boldsymbol{n}\cdot\boldsymbol{\omega} - \lambda_T(\boldsymbol{n}\cdot\boldsymbol{D} - \boldsymbol{D}:\boldsymbol{nnn}) \tag{3.1}$$

Here λ_T is the tumbling alignment parameter (*not* the thixotropic structure parameter λ), which depends on the anisotropy of the rotating object, with a value of $\lambda_T \approx 1$ for a long rod-like object, and $\lambda_T \approx -1$ for a thin disk-like one. For the former, the director is driven by flow to align parallel to the flow, while for the latter, it is driven to align perpendicular to it, so that the long dimensions of the disk align parallel to flow. The response to flow of a disordered material consisting of regions with different orientations of $\boldsymbol{n}$ is modified somewhat from the above equation by the gradient elastic forces that arise from spatial variations in $\boldsymbol{n}$. For smectics, these include elastic forces that strongly resist flow-induced changes in lamellar thickness. Despite these limitations, as a starting point, we can follow Larson and Doi[34] in accounting for spatial variations in $\boldsymbol{n}$ through invocation of a "mesoscopic averaging" procedure, which averages the outer product of $\boldsymbol{n}$ times Eq. 3.1 (i.e., Larson, Eq. 11-29 [35]) over regions large compared to the lamellar thickness but small compared to the macroscopic sample size. This produces the equation below, drawn from Larson, Eq. 11-33 [35].

$$\frac{d}{dt}\overline{\boldsymbol{S}} = \boldsymbol{\omega}^T\cdot\overline{\boldsymbol{S}} + \overline{\boldsymbol{S}}\cdot\boldsymbol{\omega} + \lambda_T\left(\frac{2}{3}\boldsymbol{D} + \boldsymbol{D}\cdot\overline{\boldsymbol{S}} + \overline{\boldsymbol{S}}\cdot\boldsymbol{D} - 2\overline{\boldsymbol{S}}:\boldsymbol{D}\left(\overline{\boldsymbol{S}} + \frac{1}{3}\boldsymbol{\delta}\right)\right) - \varepsilon\rho_v\overline{\boldsymbol{S}} \tag{3.2}$$

where the "mesoscopic" order parameter $\overline{\boldsymbol{S}}$ is defined as

$$\overline{\boldsymbol{S}} \equiv \langle[\boldsymbol{nn}]\rangle - \frac{1}{3}\boldsymbol{\delta} \tag{3.3}$$

with $\boldsymbol{\delta}$ the unit tensor. In the above, $\boldsymbol{\omega}$ is the vorticity tensor and $\boldsymbol{D}$ the rate of strain tensor, these being the anti-symmetric and symmetric parts of the velocity gradient tensor, respectively. The initial value of the tensor $\overline{\boldsymbol{S}}$ is normally taken to be zero in all components, reflecting the lack of order at the mesoscale, as it is assumed that the orientation, while locally anisotropic, averages to zero over a larger domain. The final term in Eq. 3.2 is due to the elastic director gradient terms alluded to above, which drives the mesoscopic orientation tensor $\overline{\boldsymbol{S}}$ back towards zero over a time scale set by the magnitude of the phenomenological coefficient ε, which has units of diffusivity. The term ρ_v is the density of defect lines in the sample, with units of inverse length squared. The square root of its inverse is the characteristic "domain size" or the length scale over which the orientation is relatively uniform. The form and magnitude of this term in an L_β phase is likely to be drastically different from that in a nematic. The change of $\overline{\boldsymbol{S}}$ over strain can be readily derived from Eq. 3.2 by taking the tumbling parameter λ_T to be -1 for lamellae similar to oblate particles and imposing a simple shear flow where $\nabla\boldsymbol{v}_{21} = \dot{\gamma}$ and the other elements of the velocity gradient tensor are zero. As shown in Fig. 3-3, the component $\overline{\boldsymbol{S}}_{22}$, representing the degree of alignment of the lamellae parallel to the walls of the shearing device, increases rapidly initially and then gradually approaches a steady state while $\overline{\boldsymbol{S}}_{12}$ first reaches a peak negative (because the tumbling parameter $\lambda_T < 0$) at a strain around 1.7 and approaches zero eventually as the orientation distribution in other directions vanishes, corresponding to complete alignment of the normal vector in the shear gradient direction.

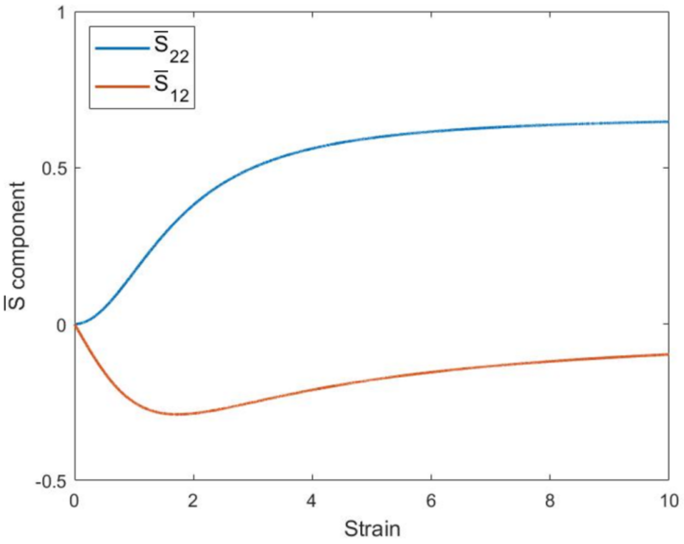

Figure 3-3. $\bar{\mathbf{S}}_{22}$ *and* $\bar{\mathbf{S}}_{12}$ *of the mesoscopic order parameter vs strain under simple shear flow.*

Despite the differences between a nematic and an L_β phase, both phases have a director specifying the orientation, and so we can use Eq. 3.2 as a means to gain some insight into the response of the lamellar gel to deformation. First, we note that the loading of the gel into a rheometer imposes local orientation on what would otherwise be a mesoscopically unoriented gel. The imposed orientation is both due to the flatness of the boundaries, which should tend to align lamellar layers that resist sharp bends in their orientation, and due to any squeezing flow needed to set and fill the rheometer gap. The orientation due to the boundary condition should produce aligned layers, with alignment decaying over a distance set, in part, by the bending modulus of the lamellae. For fluid-like L_α smectics, this modulus is of order 10^{-7} dyn,[35] and is likely much larger for much stiffer L_β smectics. While our lack of knowledge limits our ability to estimate the range over which wall-induced order might penetrate, we can say a bit more about the alignment induced by the squeezing flow used to set the rheometer gap, since we can use the analytical formula for squeezing flow between parallel disks derived for Newtonian fluids.[36] While non-Newtonian effects will modify this flow, the overall features are largely set by kinematics, which tells us that the highest strains and strain rates in this flow are the shearing strains in the *r-z* plane, as these strains and strain rates are proportional to *r/H*, where *r* is the radial position and *H* the gap, while the other, extensional, strains, have prefactors proportional to *z/H*, with *z* the position in the gap. Thus, for typical thin rheometer gaps relative to plate radius, the majority of the sample, which is near the edge, where $r/H \gg 1$, is therefore much more highly strained in shear than in extension. Hence, starting from a mesoscopically isotropic state in which $\overline{\boldsymbol{S}} = \boldsymbol{0}$, and allowing a small deformation to be imposed, the leading order term on the right side of Eq. 3.2 leads to

$$\frac{d}{dt}\overline{\boldsymbol{S}} \approx \frac{2}{3}\lambda_T \boldsymbol{D} \tag{3.4}$$

From this, and the solution to the squeezing-flow problem in Denn,[36] we readily find that the shear component of the order parameter is given by

$$\overline{\boldsymbol{S}}_{rz} \approx \frac{\lambda_T r}{H_0}\epsilon\left(1 - \frac{2z}{H}\right) \tag{3.5}$$

where H_0 is the initial gap thickness, *H* is the final thickness and *z* the position in the gap, while here $\epsilon \equiv \frac{H_0}{H} - 1$ is the strain imposed by the squeezing, where we have taken $\epsilon \ll 1$. The imposition of this strain field will orient the material in the gap and change its effective modulus in response to subsequent shearing flow. Since the modulus for an anisotropic material is a fourth rank tensor, the best we can do to estimate its effect is to assume that the *effective* modulus to subsequent shearing flow is reduced by the alignment produced by squeezing flow. By symmetry, we can therefore suggest that the effective modulus G^0 after squeezing flow, but before shearing flow, is related to the modulus G_0 of a mesoscopically isotropic (unaligned) material at small ϵ by

$$G^0(z,\epsilon) \approx G_0\left(1 - \overline{\boldsymbol{S}}_{rz}{}^2\right) \approx G_0\left[1 - \alpha\left(\frac{\lambda_T r}{H_0}\right)^2 \epsilon^2\left(1 - \frac{2z}{H}\right)^2\right] \tag{3.6}$$

where α is a parameter that reflects the dependence of modulus on local alignment, and we take $\epsilon \ll 1$. Notice that the greatest reduction in modulus, according to Eq. 3.6, is expected to be at the surfaces of the rheometer plates ($z = 0, H$) where $\left(1 - \frac{2z}{H}\right)^2$ is largest.

In addition to this aligning effect of the squeezing flow, the modulus near the wall should presumably be reduced even further owing to the wall-alignment mentioned above. If we neglect the wall effect, we can use Eq. 3.6 as an initial modulus distribution, which is further affected as shear, now in the z-θ plane in the rheometer, is imposed. Following analogous reasoning, we expect the effective shear modulus to continue to decrease in response to the aligning effect of shear, following a formula such as

$$G(z,t) \approx G^0(z)[1 - \beta\gamma^2(z,t)] \text{ for } G(z,t) > G_{min}; \text{otherwise } G(z,t) = G_{min} \qquad (3.7)$$

where $\gamma(z,t)$ is the time and z-dependent strain and we have taken $G^0(z) = G^0(z,R)$, where R is radius at the edge of the sample. Since the quadratic dependence on strain in Eq. 3.7 is limited to small strains, to crudely extend it to large strains, we limit the decrease of modulus to some minimum value.

All of the above is obviously very crude, and here we use it only to justify the assumption that the effective modulus of the initial sample is likely to be nonuniform and lower near the boundaries than in the sample bulk, and that shearing is likely to further enhance this modulus reduction, as the lower initial modulus near the wall directs subsequent shear to concentrate there, leading to still lower modulus at the wall as shearing continues. Fortunately, in what follows we will show that the modulus gradient near the wall dominates the predicted behavior, and that the functional form and depth into the sample to which the modulus reduction penetrates does not strongly influence the results. We also note that the non-uniform reduction in modulus produced by the flow can be reversed over time in the absence of flow by allowing for a non-zero final term in Eq. 3.2, corresponding to a non-zero phenomenological coefficient ε (which is *not* the strain ϵ). This recovery of isotropy provides a mechanism to gradually recover the undeformed properties of the material, except for the wall-induced orientation, which presumably remains indefinitely.

Finally, we note that Eq. 3.2 could be solved numerically without approximation for both squeezing flow and subsequent shearing flow, producing a time and spatially dependent mesoscopic orientation tensor $\overline{\boldsymbol{S}}$. To use this, however, to predict rheology, would require constitutive relationships between this tensor and the anisotropic elastic modulus, the yielding condition, and the viscous stresses. While developing such constitutive relationships is too big a task to undertake here, a possible future direction is to link Eq. 3.2 with a three-dimensional thixotropic elasto-visco-plastic (TEVP) model such as the Frederick-Armstrong kinematic-hardening model. [37,38] This would likely require introduction of tensor relationships linking $\overline{\boldsymbol{S}}$ to back-strain and/or back-stress in such models, possibly involving fourth rank tensors.

3.2.2 A structural kinetics model for thixotropic fluid

The above presentation tells us that a lamellar gel should have an elastic modulus, can yield under flow, with slow recovery thereafter, and that the modulus should vary across the gap, with lowest values at the walls. A useable model therefore needs to include these features, and so we here develop a phenomenological structural kinetics, or thixotropic, model which can describe gradual reduction in shear viscosity and yield stress upon prolonged shearing, and delayed recovery of viscosity after step-down of shear rate. Here we consider a common, basic kinetic equation (Eq. 3.8) for the thixotropic structure parameter λ (which is *not* the alignment parameter given earlier). In Eq. 3.8, the break-down term caused by flow is proportional to the shear rate with a prefactor K and the build-up term for restoration of structure is controlled by another constant k_λ. The range of λ is set to lie between 0 and 1, representing, respectively, a completely broken-down state and a fully structured one.[27] To study the shear-banding phenomenon, the velocity profile in 1D shear flow between two parallel plates located at boundaries set at $y = 0$ and $y = H$ is examined. Thus, λ and the flow parameters $\dot{\gamma}$ and σ become dependent on both time t and position within the gap y. A diffusive term $D\frac{\partial^2\lambda}{\partial y^2}$ for λ is introduced, making the model non-local, which is necessary to avoid ill-defined sensitivity to starting fluctuations and to smooth the velocity profile across adjacent bands.[39]

$$\frac{d\lambda}{dt} = -K|\dot{\gamma}|\lambda + k_{\lambda}(1-\lambda) + D\frac{\partial^2\lambda}{\partial y^2} \tag{3.8}$$

The rheological equation (Eq. 3.9) also has a rather simple form in that the shear stress is equal to a viscous term plus the yield stress and both the overall viscosity and yield stress have linear dependencies on λ. η_n is the non-thixotropic viscosity characterizing the fully broken-down structure at the high-shear limit. η_{thi} is the thixotropic viscosity and σ_{y0} is the thixotropic yield stress. The presence of the sign function in front of the yield stress terms arises because the model is a scalar model, and the sign of the yield stress depends on the shear direction.

$$\sigma = \dot{\gamma}(\eta_{thi}\lambda + \eta_n) + sign(\dot{\gamma}) * \sigma_{y0}\lambda \tag{3.9}$$

These two equations above constitute perhaps the simplest constitutive model for scalar shear stress of a thixotropic yield stress fluid in simple shear flow. Given the initial condition of λ across the gap, the time evolution of λ and the unknown local shear rates and shear stresses from the rheological equation can be solved under either an imposed shear rate or a shear stress with two assumptions. The first one is that the shear stress is the same at all positions (i.e., there are no inertial effects) and the second is that the average of the local shear rate over the gap should equal the apparent shear rate.

To incorporate strain-dependent elasticity into the model, we here replace the simple yield stress with a yield strain term which also helps to address the issue of transient local flow reversal. In a transient startup flow at constant overall shear rate, when yielding occurs in the developing banded region, flow in this region speeds up, and the unyielded zone begins to flow backwards briefly to keep overall shear rate constant at the imposed value. In the absence of a yield strain, the reversing flow instantly reverses the stress in the unyielded region because the yield stress term and the viscous contribution both take the same sign as the flow rate, which is impossible when stress is required to be uniform, since it is positive in the yielded zone. We believe that this represents a pathology caused by the complete lack of elasticity in the constitutive model, so that even a very brief reversal of shear rate immediately changes the sign of the stress. The presence of a small elastic yield strain allows the unyielded zone to keep a positive stress even as it briefly flows backward while unloading elastic strain, making a solution for a time-dependent development of banded flow possible. Inclusion of inertia is another possible "fix" for the brief reversing flow that occurs during onset of banding. But without either elasticity or inertia, there is no time-dependent solution possible from Eqs. 3.8 & 3.9 for the one-dimensional flow of a band-forming material. The introduction of elasticity can be either physically motivated (based on the soft-solid behavior of an L_β phase), or considered as a regularization, with elasticity taken to be so small that its only significant effect is to avoid a sudden change in sign of stress. As an example of physically motivated elasticity, Wei et al. used a kinematic hardening term in their predictions of shear banding dynamics.[39] To keep our model simple and avoid including features that are either nonexistent or not of prime importance in lamellar gel networks, we instead simply replace the yield stress term in Eq. 3.9 with an elastic-plastic form (Eqs. 3.10 - 3.12).

$$\sigma = \dot{\gamma}(\eta_{thi}\lambda + \eta_n) + G\gamma_e \tag{3.10}$$

$$\begin{cases} \dfrac{\partial \gamma_e}{\partial t} = \dot{\gamma} \quad \text{when } |\gamma_e| < \gamma_c (\text{pre} - \text{yield}) & (3.11) \\ \\ |\gamma_e| = \gamma_c \quad \text{where } \gamma_c = \gamma_{c0}\lambda \ (\text{post} - \text{yield}) & (3.12) \end{cases}$$

As proposed by Mujumdar et al. for a colloidal network, γ_e is the elastic strain associated with the flowing structure and physically represents the elastic deformation of flocs that form when the network microstructure of the fluid breaks down.[40] γ_e grows when the flow is in positive direction until it reaches a maximum value $\gamma_{e,critical}$ noted as γ_c which depends on λ (Eqs. 3.11 & 3.12). Note that in the post-yield region, the elasto-plastic stress model reduces to the simple yield stress model in unidirectional flow in zero dimensions. This is because $G\gamma_e = G\gamma_{c0}\lambda$ in the elasto-plastic model is mathematically the same as $sign(\dot{\gamma}) * \sigma_{y0}\lambda$ in the simple plasticity model since they both are a constant (either $G\gamma_{c0}$ or σ_{y0}) multiplied by λ. The difference is that in 1D flow, since both the viscous stress and the yield stress take the same sign as the flow direction, the overall stress in the simple plasticity model immediately turns negative when any local flow is reversed. In contrast, in the elastic-plastic model, the elastic stress is proportional to elastic strain, whose sign remains unchanged for a least a small period of time following local flow reversal. This allows the overall stress to remain positive until the strain disappears even when some local flow rates turn temporarily negative during the development of bands. For lamellar gel networks, the value of γ_{c0} could be relatively large. The lamellar bilayers can withstand elastic deformation until the accumulated strain significantly changes their orientation whereon they tend to slide upon each other. As shown in Fig. 3-3 and discussed earlier, full alignment is not achieved until large strain, and at some point, yielding occurs which cuts off the reversibility of the elastic strain, therefore an estimate of $\gamma_{c0} = 4$ was used for the proposed model.

3.2.3 Introduction of modulus gradient near the boundary

To induce the fast-shearing thin boundary layer observed in the PIV experiment, some form of perturbation near the boundary either as the initial condition or imposed permanently is required in the constitutive model. While a stress-dependent slip term might seem like an obvious choice, this does not produce the experimentally observed gap dependence of the apparent shear rate at constant stress. Another choice would be using an initial condition in which $\lambda = 1$ defines the unsheared state everywhere in the gap except at a "weak point" at one boundary (i.e., $\lambda < 1$ at $y = H$) to represent some slight apparent slip at this boundary in a rheometer. At low shear rate, this slight weakening of the material at the boundary is greatly intensified as overall strain increases. This eventually produces a highly non-homogenous shear-rate profile containing a thin layer over which shear rate changes drastically, while the rest of the fluid is left nearly non-flowing with negligible shear rate, which is similar to what is seen in the experiment. However, for this model, when the apparent shear rate increases, the local shear rate of the fast-shearing band stays the same, while its thickness increases, and the steady state shear stress remains unchanged until the shear rate is high enough that the band fills the entire gap, which is very different than the behavior of lamellar gels explained earlier. Beyond this shear rate, the flow becomes homogenous, and the stress starts to increase again, once the apparent shear rate has exceeded that of the fast-shearing band. This behavior represents typical shear banding behavior common, for example, in solutions of worm-like micelles,[41] but fundamentally different from that in lamellar gel networks, where that the fast-shearing band remains a thin boundary layer while the stress keeps increasing (albeit sub-linearly) with increasing shear rate, rather than reaching a plateau. The banding behavior of the lamellar gel network therefore is well-described neither by a convention shear-banding model, nor by a stress-dependent slip coefficient.

Hence, we propose to use a weaker modulus G instead of a weaker λ near the boundary, to induce band formation, which is inspired by the anisotropy of microstructure of lamellar gels caused by sample loading and rheometer geometry, as discussed in Section 3.2.1 above. Similar to the structural parameter λ which determines the viscosity and maximum elastic strain, the modulus G also represents the strength of our material, especially when it is closer to being an elastic solid than to a liquid in the unsheared state. While we have outlined a potential microstructurally based approach of doing mesoscopic average over the lamellar anisotropy in section 3.2.1, we did not derive from this a governing equation for a spatial and time dependent G which can self-adjust over time and different flow conditions. Nevertheless, to see if a non-uniform modulus might help explain the unusual rheological behavior of lamellar gels, as a first step, we here explore the effects of a simple fixed non-uniform modulus profile with a near-boundary layer gradient to allow a smooth transition of G from a wall-influenced value to that of the bulk. As this is a crude approximation, and the exact shape of the fixed profile should vary under shear anyway, we resort to a simple linear or piecewise linear modulus profile. An example of a linear profile is an increase from 0.002% to 100% of the bulk value G_0 over a distance from 0% to 20% of the gap width as shown in Fig. 3-4. However, to control the near-wall gradient independently without affecting the boundary layer thickness, we use a segmented linear profile as the standard case with smaller gradient near the wall (accounting for a quarter of the wall gradient zone, or 5% of the total gap thickness) also shown in Fig. 3-4, which gives us better agreement with the creep test under small stress in the experiment. The influence of the shape of the profile and of the minimum value of G at the boundary will be discussed later. Exponential and logarithmic profiles were also considered but found to yield results controlled by the slope of the profile at the wall and so results for these profiles are not shown. We note that both boundaries of the shearing geometry should apply a similar gradient in G, but for simplicity we here introduce this profile onto one wall only.

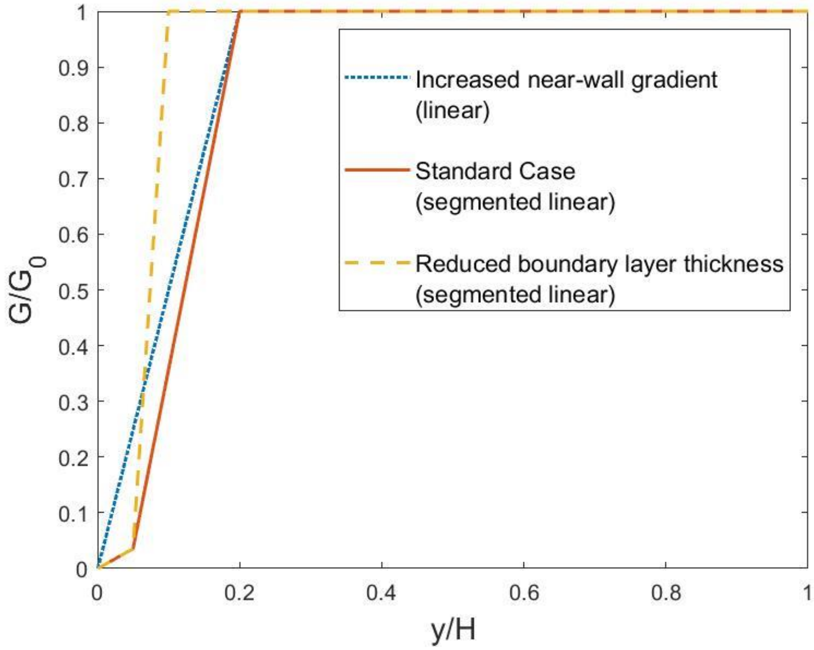

Figure 3-4. Different linear and segmented linear profiles of modulus G across the gap with smallest value equal to 0.002% of the bulk modulus G_0 at near one wall.

3.2.4 Model parameterization

Besides the profile of the modulus near the boundary, there are six model parameters to be specified including $K, k_\lambda, D, \eta_{thi}, \eta_n, G_0$ and γ_{c0}. We set $G_0 = 500$ Pa taken from the instantaneous modulus measured in experiment and $\gamma_{c0} = 4$ explained in section 3.2.2. The viscosities cannot be easily derived from experiment due to the huge difference between local shear rates and apparent shear rates caused by extreme shear banding. They are therefore tuned together with the time constants which control how λ changes with shear rate so that the constant-stress (creep) response is roughly similar to that seen in the experiments. After a preliminary study, we set $\eta_{thi} = 80\ \mathrm{Pa\cdot s}$, $\eta_n = 0.2\ \mathrm{Pa\cdot s}$, $K = 0.2$, $k_\lambda = 0.01\ \mathrm{s}^{-1}$ and $D = 10^{-11}\ \mathrm{m}^2/\mathrm{s}$ and retain these values for all the predictions shown here. In the experiments, gaps of 0.1 to 1.0 mm in plate-plate instruments were used for some measurements, while other data were obtained in 25 mm diameter cone-plate fixtures with 2° cone angle, producing a gap at the sample edge of 0.44 mm. Our simulations are carried out in a plane Couette geometry with uniform gap, and we set the gap to H = 1 mm in most cases, for simplicity. Because of the qualitative character of our modeling, we feel that additional efforts to match conditions and parameters of our predictions with experiments in more detail than this would be premature.

3.3 Method

During each time step, MATLAB was used to solve for the time evolution of the local variables λ_y and $\gamma_{e,y}$ first and then σ_y and $\dot{\gamma}_y$, after which the time step is advanced. When shear stress is imposed, it is the same everywhere, and the local shear rate at each position in the gap can be readily solved for. When the apparent shear rate is imposed, both the local shear rate and uniform shear stress are unknown and must be solved from a system of linear equations using matrices. The time step was chosen to be 0.002 s which is sufficiently small for the results to converge. The 1D grid is constructed with tiles of two different sizes such that 90% of the gap is made up of tiles of 0.5% of the overall gap width H and the remaining 10% of the gap nearest the boundary is better resolved by discretizing at 0.05% intervals of the gap H. For higher spatial resolution, the time step needs to be made even smaller due to the diffusion term in Eq. 3.8, requiring much longer computation time for minimal gain. A brief discussion on grid resolution and convergence of the solution is covered later.

3.4 Results

Here we present a through comparison of the results from the proposed constitutive model with the various experimental rheological characterizations published in previous work.[1] We start with the creep and recovery test during which a constant stress is imposed for a long period of time and then removed. The experimental results, shown in Fig. 3-5(a), show a jump in initial strain upon application of stress that is roughly proportional to the imposed stress. For relatively small stress, the experimental material shows a “quasi-solid” creep response that follows a weak power-law time-dependence (with exponent 0.25) and partial recovery of strain upon stress removal. In response to a larger imposed stress, the material exhibits an apparent “yielding” behavior in that after a brief period of weak power-law creep, it abruptly accelerates to a much faster flow following a much steeper power-law (with exponent 1.35) at long times. The results from the constitutive model qualitatively predict the observed creep under small stress and the subsequent partial recovery upon stress removal, as well as the yielding behavior under a larger stress. The exponent of the power-law time-dependency under small stress or short times (0.25) is comparable to the observed value, while the value at high stress or long times (1.16) is somewhat smaller than the observed value (1.35). Depending on the choice of model parameters and the gradient profile near the boundary, the shape of the curves and the exact values of the exponents change, as discussed later, but continue to agree qualitatively with the experiment.

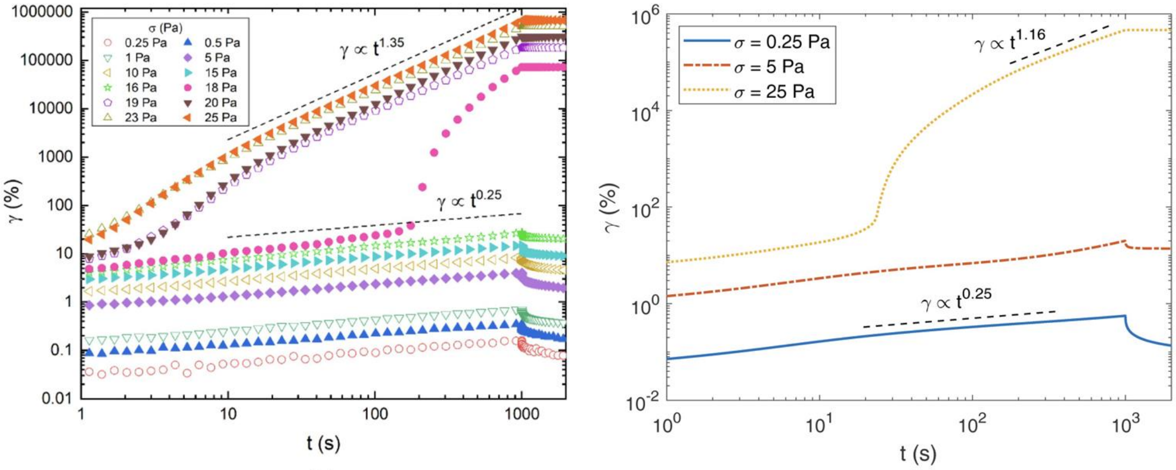

(a) (b)

*Figure 3-5. Creep in response to stress applied for 1000 s and recovery measured over the next 1000 s from **(a)** experiment (Reproduced from [1], with the permission of AIP Publishing), and **(b)** constitutive model.*

The time evolution of the velocity profile across the gap from the constitutive model also agrees qualitatively with the experiment, presenting strong evidence for the validity of the model. As shown in Fig. 3-6, shear banding occurs almost immediately after the impose of stress, and shear rates in the slow-shearing band slow down with time as indicated by the change of slope in the velocity profile, although this happens over a faster time scale in the simulation than in the experiment, while the faster-shearing band near the boundary becomes thinner over time (as shown by the tilt in the dashed lines in Fig. 3-5 that mark the boundary between fast and slow bands).

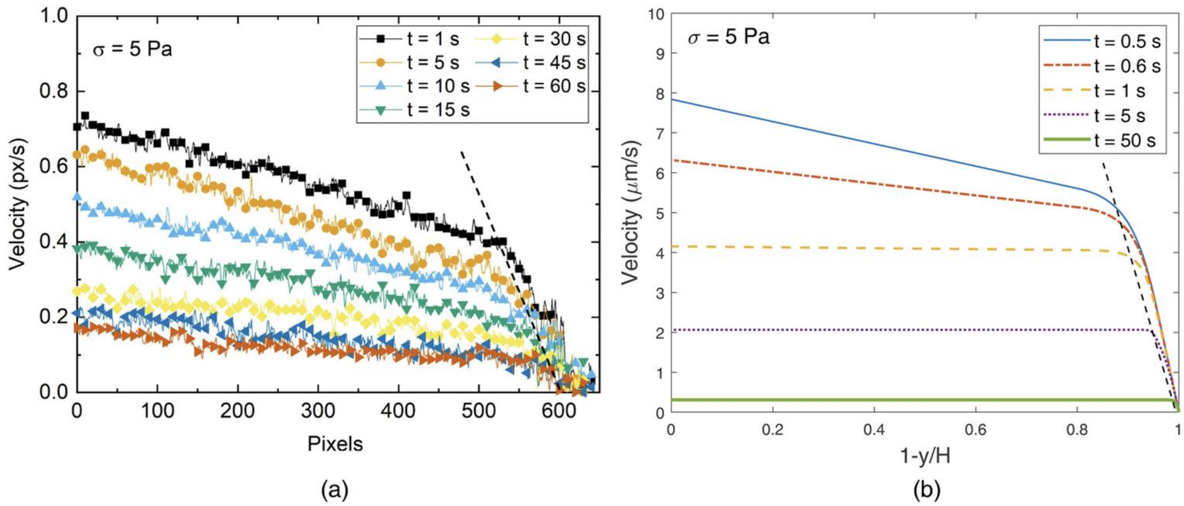

Figure 3-6. Velocity profiles at different times during creep after the imposition of a constant shear stress of 5 Pa from ***(a)*** *experiment (Reproduced from [1], with the permission of AIP Publishing, each pixel corresponding to an interval of 0.687 μm), and* ***(b)*** *the constitutive model, note that V is plotted against (1-y/H) to match the experiment set up in PIV. The dashed lines show the transition between the "slow" and "fast" bands.*

Next, under an imposed overall constant shear rate, in the experiment, the shear stress decreases over a long period of time as shown in the first 500 s of Fig. 3-7(a). Following a step-down in the shear rate, the sample shows a sudden drop in the stress followed by a more gradual increase in the stress and then a slow decrease over longer period of time toward a plateau value. The sudden drop followed by a more gradual increase in stress is the normal response of a thixotropic, nearly inelastic fluid, and that feature is captured by the constitutive model shown in Fig. 3-7(b). Missing from the model prediction, however, is the gradual decrease in stress at long times after the step-down, as well as the long-time decay of stress before the step-down, as the stress drops quickly followed by a slight rebound to steady state before the shear-rate step-down. This is expected as our model lacks the additional more complex long-time dynamics of the actual material. This could be addressed by including multiple modes of λ decaying over different time scales, as described in earlier work,[23] a complication we avoided in this first modeling attempt, in order to maintain the simplicity of the model.

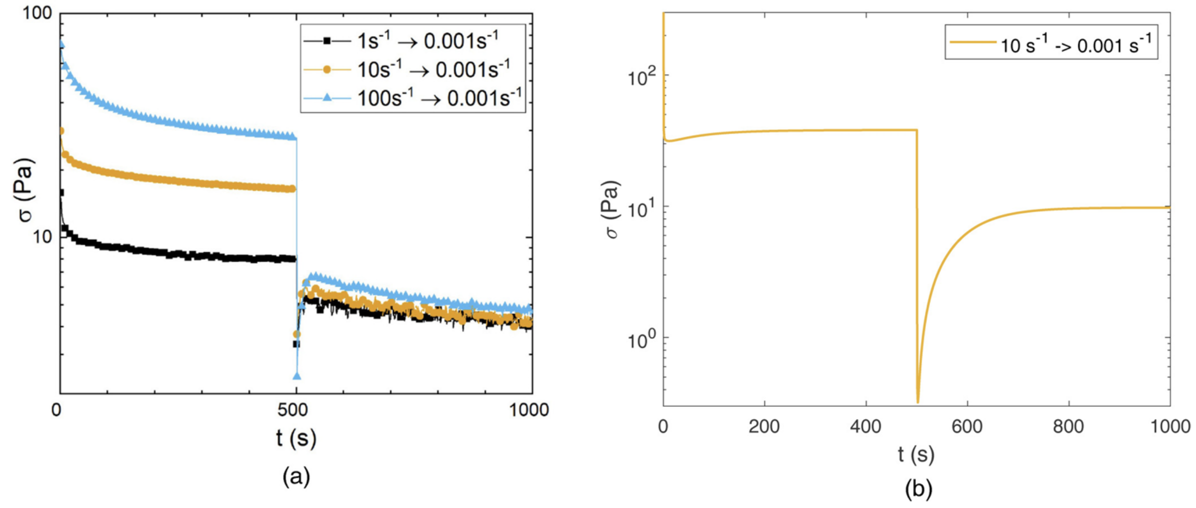

(a)

(b)

Figure 3-7. Step down shear tests with a sudden drop of shear rate at t = 500 s from ***(a)*** *experiment (Reproduced from [1], with the permission of AIP Publishing), and* ***(b)*** *the constitutive model.*

In addition, we find that the velocity profile under constant shear rate from the PIV experiment is well predicted by the model. For a small shear rate of 0.001 s^{-1}, the experimental results in Fig. 3-2(a) show that shear banding slowly develops over time from an initially linear velocity profile. For higher shear rates of 0.01 s^{-1}, or above, the transition into the plug flow happens almost immediately, so that the bulk of the material behaves like a solid slab moving with a speed somewhat less than that of the rotating plate of the rheometer while the fast shearing occurs in thin boundary layers adjacent to the plates, mostly at the stationary plate as shown in Fig. 3-2(b). All these phenomena are captured by the constitutive model in the results in Fig. 3-8. While the fast-shearing banding for lamellar gel is more prominent near the stationary boundary modeled by the introduction of the weak modulus layer, the experiment also shows a smaller degree of slip at the moving boundary. The different behaviors at the two boundaries are not necessarily caused by the motion of one boundary while the other is stationary, but could instead be the result of geometric differences between the cone and plate surfaces, differences in their surface friction, or a gravitational effect. To resolve the source of the asymmetry thus will require additional PIV experiments.[1] In addition, the model reveals that for the shear of 1.0 s^{-1} in Fig. 3-8(b) there is an overshoot of velocity near the upper moving plate, which means that the shear rate in the slower shearing band turns slightly negative due to elasticity, before quickly declining to zero as the band becomes a plug flow. In the experiments, the velocity on the wall side of boundary layer becomes momentarily larger than the plug flow velocity of the bulk due to elastic recoil, as can be seen in Fig. 3-2(b) at t = 30 s and PIV data at other shear rates,[1] although noise and limited resolution of PIV prevent us from drawing a definite conclusion.

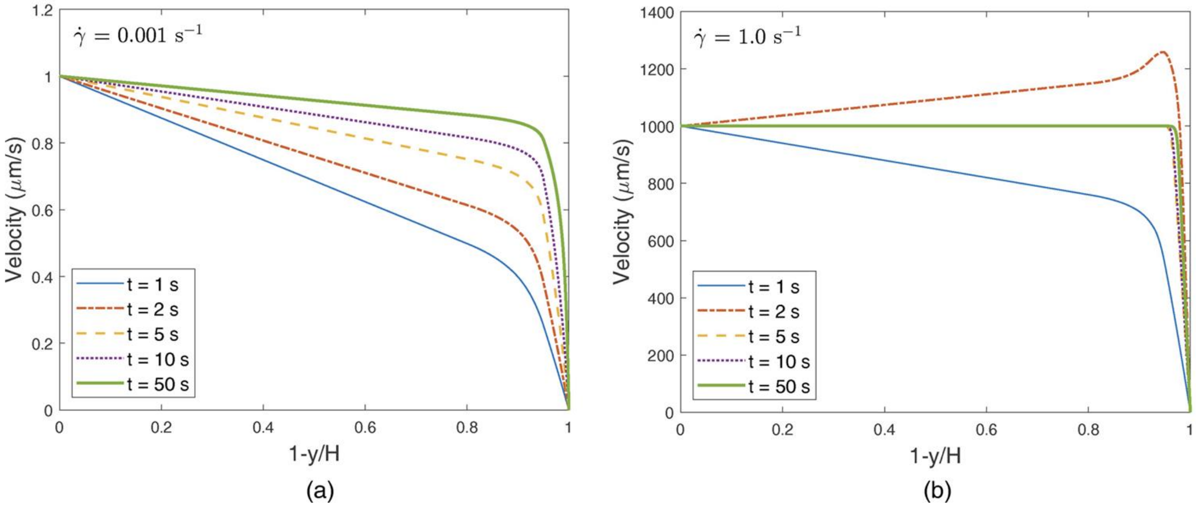

(a)

(b)

Figure 3-8. Velocity profiles at different times during start-up of constant shear rate predicted by the constitutive model: ***(a)*** $\dot{\gamma} = 0.001\ s^{-1}$, *and* ***(b)*** $\dot{\gamma} = 1.0\ s^{-1}$.

In the experiments, subjecting the sample to a high shear induces microstructural changes leading to reduced viscosity as demonstrated by the hysteresis loops seen upon initially increasing and then decreasing the shear rate in shear-rate ramps in Fig. 3-1. In Fig. 3-9(a), an immediate repetition of the shear hysteresis test shows essentially no hysteresis and gives a stress vs shear rate curve that is almost identical to that for the first decreasing shear-rate ramp in Fig. 3-1.

However, as described in ref. [1], given sufficient rest time for about 12 hours, the microstructure is partially recovered and hysteresis is again observed, indicating a very slow mode of recovery. Since we make no effort to include such a “slow mode” of structure recovery, our model with a fixed modulus profile is unable to capture the hysteresis seen in the experiments, and we aim only at describing the flow curve after the first pre-shear and before recovery by the “slow mode.” However, we will discuss later how the hysteresis and the very slow structure recovery in the experiment could be the result of a modulus change near the boundary. Within the restriction in this section, the predictions in Fig. 3-9(b) agree reasonably with the measurements in Fig. 3-8(a), including the roughly two-orders of magnitude increase in stress over a five-order-of-magnitude increase in shear rate.

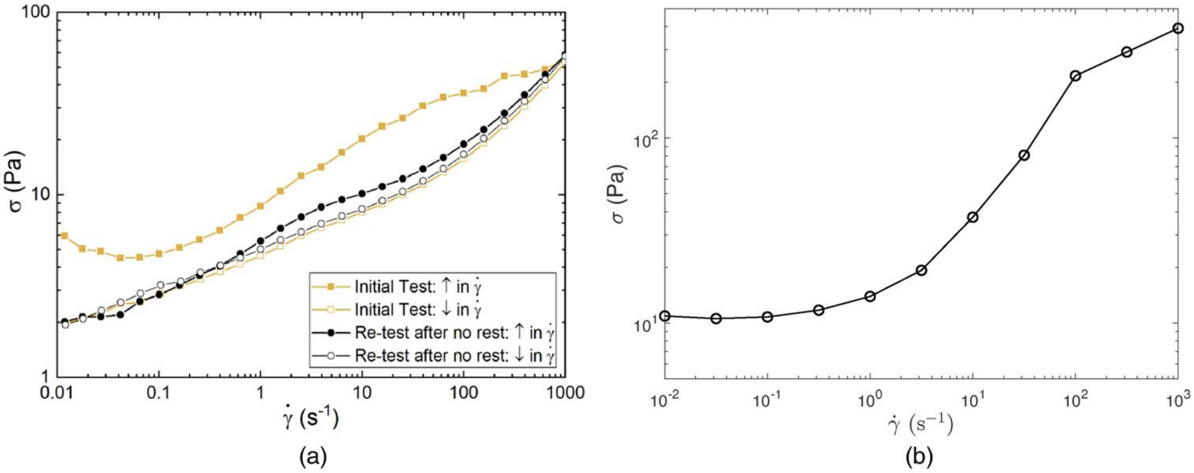

*Figure 3-9. **(a)** Shear stress response to increasing and decreasing shear rate ramps in experiment (Reproduced from [1], with the permission of AIP Publishing), and **(b)** steady-state shear stress versus imposed constant shear rate.*

After a step-strain, the shape of the model prediction of modulus decay in Fig. 3-10(b) after 10 s qualitatively agrees with the simple power-law response seen in the experiment results in Fig. 3-10(a). Despite the difference in exponent and modulus value, the model still successfully predicts the strain softening at strains of 5% and higher, and the prolonged relaxation over several orders of magnitude of time. Further improvement may require more parameter tuning and a distribution of thixotropic time scales, since we already noted that there are some very long-time scales missing from our model, that are responsible for the hysteresis in the shear up and down ramps. Attempting to include such a distribution is worth considering, but would complicate the model, and also invite the kind of "data fitting" that we think is not warranted at this stage.

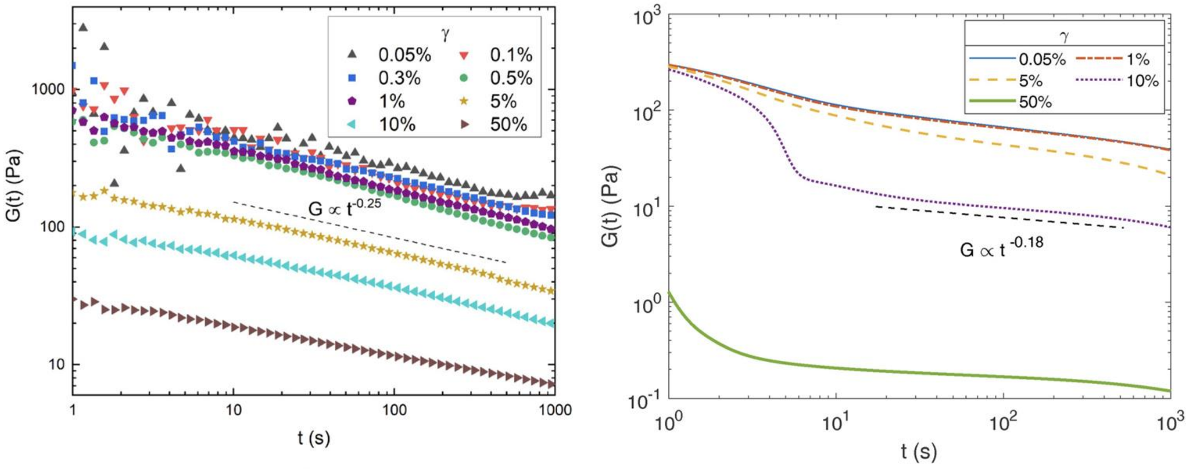

(a) (b)

Figure 3-10. Response of the relaxation modulus, G(t), to varying imposed step strains, γ. ***(a)*** *from experiment (Reproduced from [1], with the permission of AIP Publishing), and* ***(b)*** *from the constitutive model.*

In an oscillatory shear amplitude sweep, the model (Fig. 3-11(c)) predicts a linear region for small strain followed by a plunge in the storage modulus which drops below the loss modulus for large strain, which is similar to experimental results (Fig. 3-11(a)), although the critical strain at which the collapse of stress occurs is a factor of five lower than in the experiment. In the frequency sweep test, the storage modulus is found to be higher than the loss modulus until reaching a frequency over 5 rad/s, so it deviates from the experimental results as seen by comparing Figs. 3-11(b) and 3-11(d). This is not surprising, since the model has only a single thixotropic time scale, and frequency-dependent moduli are especially sensitive to the distribution of time scales in the material. An analogous situation is the common use of a single-mode nonlinear model of viscoelasticity to model a polymer solution: the start-up of shear can often be qualitatively predicted, but oscillatory shearing measurements of *G'* and *G''* disagree drastically with such a simple model, as is so well known that comparisons of one-mode models with *G'* and *G''* data are often simply avoided. Despite this obvious limitation of our model having only a single mode, we study the oscillatory flow here because the *G'* and *G''* response of our model shows a complex frequency dependence, rather than just simple Maxwellian behavior typical of single-mode models. Again, a distribution of thixotropic time scales could be used to improve the prediction but is unwarranted at the present stage of the model development.

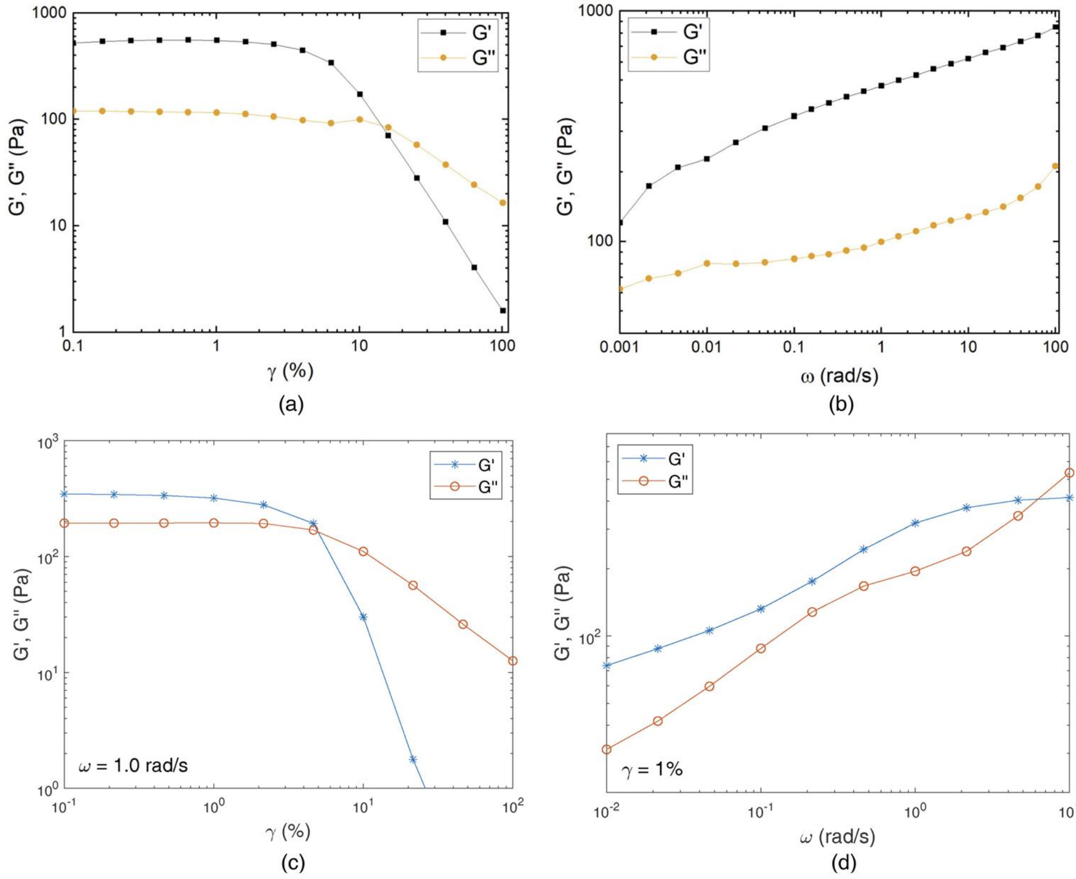

Figure 3-11. Results of oscillatory shear tests: ***(a)*** *amplitude sweep at 1 rad/s from experiment,* ***(b)*** *frequency sweep at 1% strain from experiment (Reproduced from [1], with the permission of AIP Publishing),* ***(c)*** *amplitude sweep at 1 rad/s from the constitutive model, and* ***(d)*** *frequency sweep at 1% strain from the constitutive model.*

A peculiar feature of these gels is the lack of correspondence between step-shear and oscillatory shear results, even when both are carried out at strains small enough to be in the "linear" regime, defined by an insensitivity of time- or frequency-dependent modulus to the strain amplitude. In the experimental results in Figs. 3-10(a) and 3-11(a), the linear region is reached at strains of 1% or less, yet it is clear from Figs. 3-10(a) and 3-11(b) that the time and frequency dependencies of the moduli within this linear regime are not related to each other by the Fourier transformation expected for linear rheological functions. This can be seen by observing the three-decade power law in G(t) in Fig. 3-10(a), from 1 to 1000 s, which is not mirrored in a similar power law at frequencies 0.001 to 1 s^{-1} in Fig. 3-11(b). Whatever "power-law" may exist in Fig. 3-11(b) has an exponent much smaller than 0.25, and no power-law can describe the behavior at frequencies near 0.001 s^{-1}. This failure to reach a true linear viscoelastic regime is also seen in the model predictions in Figs. 3-10(b) and 3-11(d), and can be attributed to the banded structure present in both experiments and simulations. While a "linear" response is evident at low strains in oscillatory shearing in both experiments, Fig. 3-11(a), and the model, Fig. 3-11(c), the response is not truly linear viscoelastic in the conventional sense, and the behavior near the wall is highly non-linear, despite the superficial linearity of the oscillatory response. In fact, the response to a sinusoidal strain history is not sinusoidal even in the "linear" small-strain regime; the values of *G'* and *G''* are obtained from the stress amplitude and phase angle using convolution time integrals of stress and strain waveforms in both experiment and simulation. The key to this failure of normal rules for "linear viscoelasticity" is the inhomogeneous strain field, with the inhomogeneity depending on the time- or frequency-dependence of the flow. Thus, there is linearity *separately* for small step strains and for small oscillatory strains, indicating that in each of these the time- and position-dependent strain distributions within the sample are proportional to overall strain magnitude, at small strains. However, step shear and oscillatory shearing evidently have different time- and spatial distributions of strain within the sample. Thus, their responses are not related to each other by the usual linear viscoelastic transformations. This is not surprising, since the relationship between $G(t)$ and $G^*(\omega)$ in the linear regime is based on a uniform strain within the material. The situation is somewhat analogous to measuring torque response for a simple viscoelastic material in a cone-and-plate versus a plate-and-plate device in the linear limit. The torques differ because the stress in the plate-plate device is not uniform, even though the overall torque is linear in the strain amplitude. A conversion of the response in one geometry to that in the other has to integrate over the nonuniform stress in the plate-plate measurement. The strain nonuniformity in the lamellar gel is vastly more complex than in the plate-plate geometry; strain varies along the gap and not simply along the radius, and is evidently dependent on frequency and time, so a simple conversion from frequency to time domain is not possible. Thus, our model helps to resolve this puzzling "linear," yet nonlinear, feature of the rheology, and is an interesting case in which the usual rheological tests of "linearity" fail completely.

In the experiments, the material exhibits an intermediate response between rheological and "tribological" in that the stress differs when the gap is changed, with either the shear rate or the plate velocity kept constant with changing gap.[1] For example, under a constant shear rate, the experimental stress increases with increasing gap (and therefore with increasing plate velocity), as shown in Fig. 3-12(a). In the model, the weaker modulus profile is introduced at one wall of the geometry, and its width is taken to be independent of the gap width. Thus, for wider gaps, the modulus gradient extends over a smaller part of the gap. For the standard case we considered, the modulus varies from the bulk value over 20% of the gap, but this percentage decreases when the gap becomes larger. From simulations, we obtain in Fig. 3-12(b) a similar dependence on gap as seen in the experiments in Fig. 3-12(a), except for the initial rapid rise of stress which is absent in the experiment likely because of lack of rheometer time resolution at short times. The small bumps for case of the highest gap thickness of 5 mm are caused by the shrinkage of the fast-shearing banding with reduced resolution as the low-modulus layer is reduced to only 4% of the gap width, causing the transition to be a bit unsmooth. The simulations also largely lack the long-time slow decay seen in the experiments, again likely because of the lack of a structural "slow mode" in the simulations.

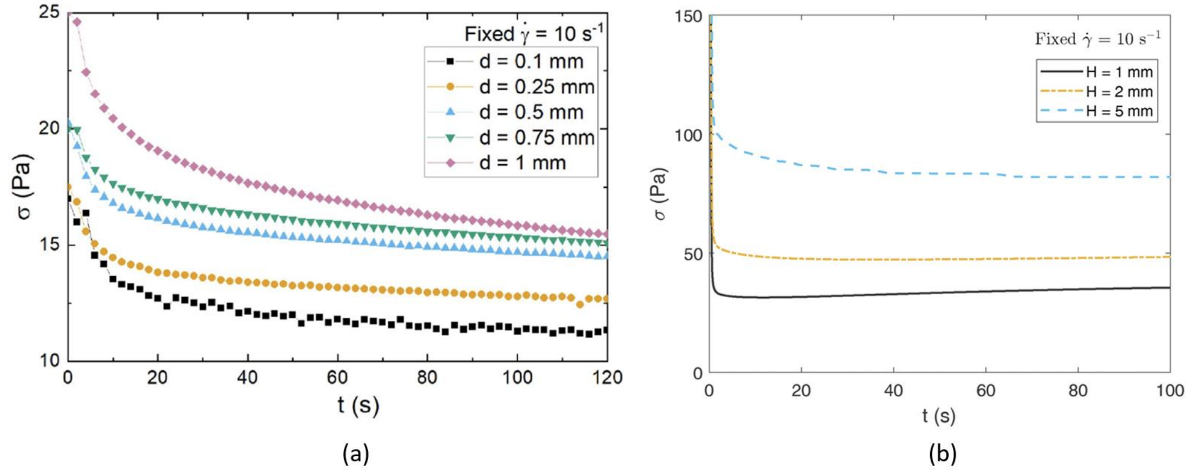

Figure 3-12. Shear stress curves for different gaps at constant shear rate of 10 s^{-1}: ***(a)*** *from experiment (Reproduced from [1], with the permission of AIP Publishing), and* ***(b)*** *from the constitutive model.*

In summary, the proposed thixotropic constitutive model with a linear modulus gradient near the boundary captures qualitatively a surprising number of the rheological properties observed in the experiments as well as the time evolution of the velocity profiles across the gap. There are discrepancies in the magnitude of stress and in the time scales for rheological changes compared in some tests, which could likely be improved by a more extensive parameter optimization, but our goal here is not to fit the model exactly with the experiment material. Our constitutive model is too simple and crude to make quantitatively realistic predictions, or for them to be meaningful if they were achieved. Improved agreement, if needed for modeling flows of a particular gel, could be produced empirically by using multiple thixotropic time scales. A more rigorous approach would require a more microscopic model of the lamellar structure of the gel, and the effect of the hard boundaries on this structure. Nevertheless, we believe that we have demonstrated that the introduction of a modulus gradient near the boundary is a key element in describing the unique properties of lamellar gel networks.

3.5 Discussion

Among the variety of rheological tests, we focus our discussion here on the response to imposition of a constant shear stress, which is imposed across the entire gap even in banded flow, and therefore is in some sense the “simplest” test. Given the importance of the modulus gradient to the rheological properties predicted by our model, and the arbitrariness of our choice of a segmented linear near-wall modulus profile, we examined the sensitivity to this profile of the model predictions. The details are given in the Appendix, and it was found that the modulus gradient within the vicinity of the wall determines the exponent of the approximate power-law time dependence of the strain on time while the overall thickness of the weak modulus layer has little effect as shown in Fig. 3-15 in the Appendix, because both the bulk and the portions of the modulus-gradient region farthest from the wall quickly stop flowing and most flow is concentrated in a boundary layer that is initially less than 5% of the gap width and shrinks further with time. The minimum modulus at the wall is also important that its product with the elastic strain limit γ_c needs to be sufficiently small compared to the imposed stress to trigger continuous creep and partial, rather than complete, recovery; see Fig. 3-16 in the Appendix.

If we further investigate the behavior close to the boundary for the standard case under a moderate stress of 5 Pa shown in Fig. 3-13, we see that initially the elastic strain γ_e accumulates rapidly within 0.1% of the boundary where the shearing is concentrated (as shown by blue, red, and yellow lines in Fig. 3-13(a)). At the same time, the local value of λ decreases to 0.81 in Fig. 3-13(c) due to shear which therefore reduces the threshold $\gamma_c = \gamma_{c0}\lambda$ from 4 to around 3.25. Here, all the strain build-up is elastic (i.e., reversible) and is directly governed by the local shear rate. Once γ_c for yield near the boundary is reached at around t = 40 s, while the total strain keeps increasing for y within 0.1% H as shown (by the blue, red, and yellow lines) in Fig. 3-13(b), the *elastic* strain build-up in Fig. 3-13(a) significantly slows down and levels off eventually. This is because the additional elastic strain increase is now controlled by the gradual rebound of the threshold γ_c from 3.25 to a new threshold of around 3.7 due to the slight recovery in λ near the wall to around 0.92 in Fig. 3-13(c) as the shearing slows down (again shown by blue, red, and yellow lines) in Fig. 3-13(d). In comparison, γ_e away from the boundary (cyan and green curves in Fig. 3-13(a)) stops increasing at a value below γ_c because the local shear rate approaches zero (shown by cyan and green curves in Fig. 3-13(d)). Thus, the fast-shearing region near the wall thins with time, as can be inferred from Fig. 3-13(d) where the stoppage of local shear rate occurs at progressively later times at points closer to the wall from y = 2% H to y = 0.5% H and causes the local elastic strain at these points levels off in Fig. 3-13(a). Eventually, the thinning of the fast-shearing band ceases, as the local shearing continues for points close to the wall (blue, red, and yellow lines) in Fig. 3-13(d). As a result, the fast-shearing band is concentrated in a very thin layer, whose ultimate thickness according to Fig. 3-13(d) is between 0.1% and 0.5% H, and by further examination is found to be around 0.4% H. Within this thin zone, the strain continues increasing with time, but its elastic portion has reached its threshold (blue, red, and yellow curves in Figs. 3-

13(a) and 3-13(b)). This progressive concentration of shearing within an ever-thinner zone is an important characteristic of the lamellar gel that we both observed experimentally and captured within our model.

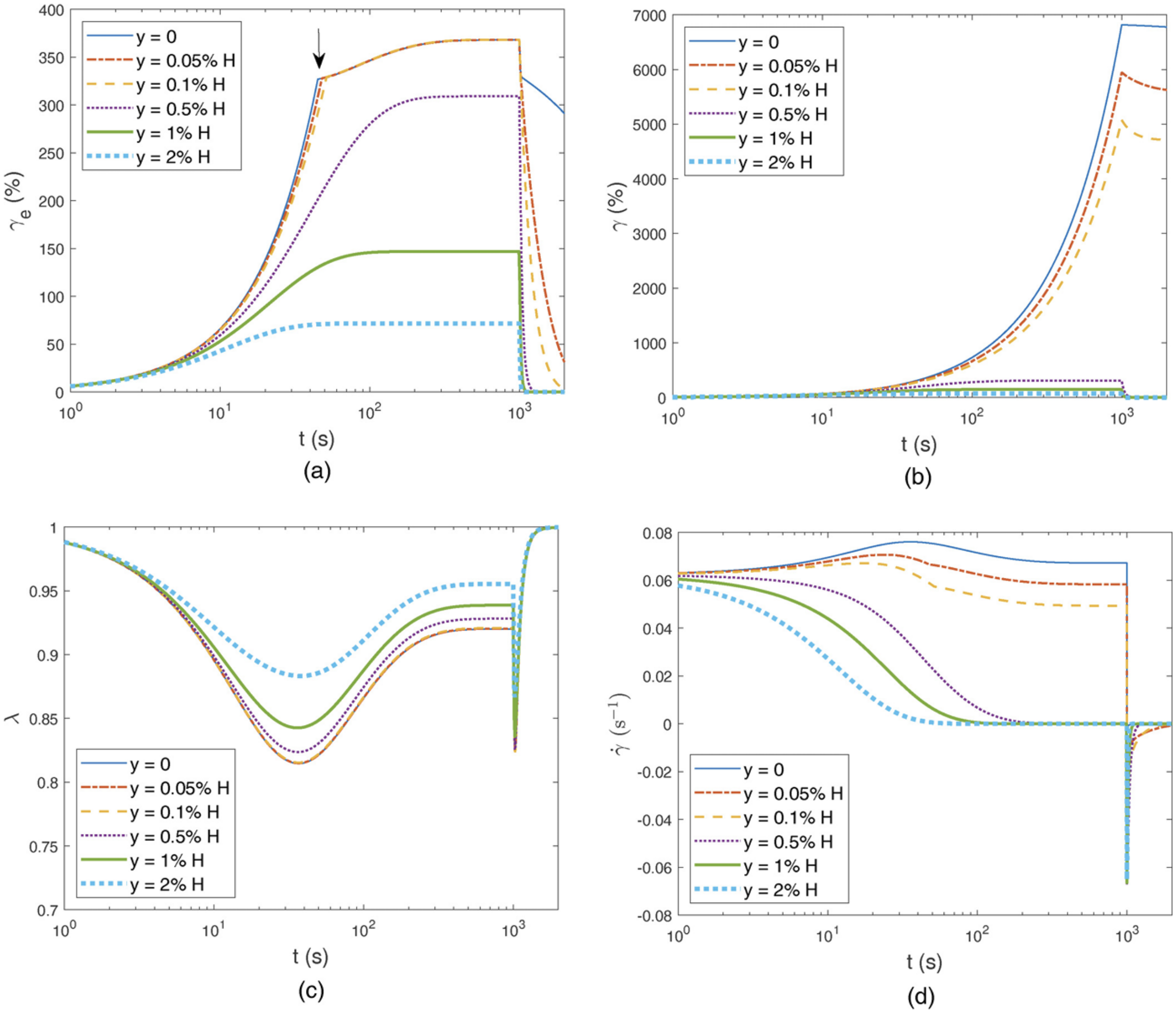

Figure 3-13. Time and local variation of ***(a)*** *elastic strain* γ_e*,* ***(b)*** *total strain* γ*,* ***(c)*** λ*, and* ***(d)*** *shear rates during creep with constant stress of 5 Pa imposed for 1000 s and thereafter removed.*

The modulus profile near the boundary also influences the recovery in Fig. 3-13 by controlling how much local elastic strain has accumulated at each position, which depends on position except for the upper three lines in Fig. 3-13(a). Even very close to the wall, where the accumulated strain is insensitive to position (as shown by the upper three lines in Fig. 3-13(a), the modulus is position-dependent, and this controls how fast the subsequent the recovery occurs. The change of total strain in Fig. 3-13(b) also shows that most of the shearing occurs at the boundary, which has the lowest modulus and any strain beyond the elastic strain limit becomes unrecoverable after stress removal.

It should be noted that most of the shearing occurs within a few tiles of the 1D grid right at the boundary, which brings into doubt whether the system is sufficiently resolved spatially. In fact, Fig. 3-14(a) shows that in creep under a stress of 10 Pa, the upturn in strain after the power-law time region can be pushed to later times if a smaller tile size is used. Initially, we attributed this sensitivity to the finite resolution of the method and assumed that it would disappear when the tiles become infinitely small. In this case, the hypothesis could not be verified due to the limitation on time steps from the diffusion term in the model, since a smaller time step is required for a smaller tile size. However, we found previously that at small stress, by using a constant $\lambda = 1$ and dropping the diffusion term to access much smaller tile size without reducing the time step, the curves converge onto one with the upturn remaining. Hence, this upturn is indeed a feature of the model rather than an artifact of inadequate spatial resolution. Such an upturn was also actually observed in the experiment after a very long time as shown in Fig. 3-14(b). When the boundary layer is spatially resolved, its thickness depends on the modulus profile near the wall. As the modulus increases from the minimal value as one moves further away from the wall, the shearing stops once $G \cdot \gamma_c \geq \sigma$ and that is where the boundary layer ends.

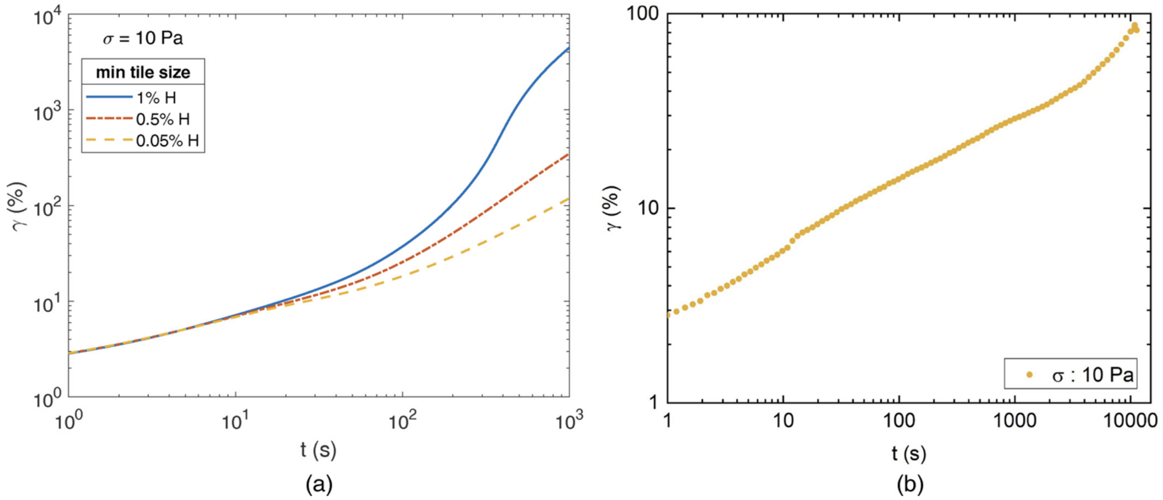

Figure 3-14. ***(a)*** *Predicted creep response under stress of 10 Pa with decreasing tile size near the boundary from both the standard constitutive model, and* ***(b)*** *Experimental creep data showing upturn at very long times (Reproduced from [1], with the permission of AIP Publishing).*

Finally, we return to the constant-shear-rate test and examine the potential of our model to be able to predict hysteresis as seen in the experiment. While the non-uniform modulus profile we used is fixed, in reality it is more likely to further evolve under imposed shear. It is a reasonable assumption that the weak modulus layer near the boundary will be further weakened under increasing shear especially since the shearing is concentrated in the boundary layer, and the structural rebuild corresponding to modulus recovery with reducing shear rate occurs at a slower time scale than the thixotropic viscosity. As a result, the modulus near the boundary will be weakened during the shear-rate ramp-up scan but likely recovers too slowly during the shear-rate ramp-down scan to avoid hysteresis. Therefore, in Fig. 3-17 in the Appendix, we plot an additional curve derived by using a "stronger" modulus boundary layer with larger $G_{\min}$ at the boundary meant to represent the material before it has experienced very high shear rates during the ramp-up scan. Significant hysteresis can be observed at low shear rates, which qualitatively resembles the experimental results in Fig. 3-1. By adding thixotropic time scales to our model, we could capture such behavior less artificially, but as noted before, attempting to make the model more comprehensive is premature, in our view.

Our model thus seems to be a promising starting point towards explaining and modeling the flow and rheology of lamellar gel networks summarized in Table 3-1, and represents a new category of constitutive equations, one in which, along with 1) a yield stress, 2) thixotropy, and 3) elasticity, also contains 4) a modulus gradient. The most unsatisfying part of the model is the ad hoc imposition of a modulus gradient, rather than allowing one to emerge from the model itself. Thus, a more satisfying model would include *the non-local physics of spatial variations in modulus*, resulting from the underlying structure, the boundary condition against the solid, and the flow induced by rheometer loading and subsequent shear. We note here that we have not accounted for any effect of shear on the modulus, and simply assumed that only the flow produced by loading into the rheometer can have any effect on the modulus. Obviously, this is a serious limitation of the model. The more physical model presented in Section 3.2.1 provides a starting point towards a more realistic model.

Table 3-1. Dynamic rheological signatures of lamellar gels and their manifestations (or lack thereof) in the proposed model.

Behavior of lamellar gel networks	**Model prediction**
1. Shear thinning with increasing shear rate	See Fig. 3-9(b) (apparent shear stress increases less than a factor of 10^2 when shear rate increases by 10^5)
2. Thixotropy	See Fig. 3-7(b) for quick stress rebound after shear step-down
3. Gradual decrease of viscosity over very long time under constant shear rate	Not captured by the current model as the stress quickly reaches steady state in Figs. 3-7(b) and 3-12(b) (could be addressed by introducing multiple modes of λ or stretched exponential)
4. Pronounced hysteresis in up- and down-ramps of shear rate	Not captured by the current model (could be addressed if modulus variation under shear is allowed as discussed)
5. Shear banding develops into plug-like flow with very thin fast-shearing band under constant shear rate	See Figs. 3-8(a) and 3-8(b)

6. Weak power law creep under small stress and partial strain recovery upon stress removal	See blue curve in Fig. 3-5(b)
7. Creep followed by yielding above	See yellow curve in Fig. 3-5(b)
8. Slow power-law stress relaxation after step strain	See Fig. 3-10(b) with a nearly linear viscoelastic regime up to 1% strain, similar to the experiment
9. Linear regime up to a critical strain beyond which G' drops below G'' in amplitude sweep of oscillatory shear test	See comparison of Figs. 3-11(a) and 3-11(c)
10. G' is much higher than G'' in frequency sweep of oscillatory shear test	Only true in a small range of frequency in Fig. 3-11(d), presumably due to the limitation of simple one-mode model
11. Gap-dependent behavior	See comparison in Fig. 3-12 where larger gap leads to higher stress under the same shear rate

3.6 Conclusion

In summary, we have proposed a constitutive model that successfully predicts the shear banding phenomenon in lamellar gel networks during creep and shear flow by imposing a boundary-induced modulus gradient. The model also captures some important features of the material, such as a thixotropic shear-thinning behavior, creep under constant shear stress and partial recovery of strain upon stress removal, the drop of storage modulus below loss modulus at large amplitude in oscillatory tests, and the gap-dependent rheology. The creep behavior is sensitive mostly to the modulus magnitude and its gradient nearest the boundary, which controls the thin boundary layer where most of the shearing is concentrated. We also show as a proof of concept that hysteresis can be predicted if the non-uniform modulus profile is allowed to vary under shear instead of being fixed. The physical origin of the boundary-induced modulus gradient could be related to the lamellar microstructure, which likely aligns preferentially parallel to the wall, near the wall, producing a low modulus there, and becomes disorganized further from the wall, resulting in a much higher modulus in the bulk. We discussed how a more rigorous, microstructurally based approach might be taken to derive the variation of the modulus profile by doing a mesoscopic average over the lamellar anisotropy. Improvements in the model will likely also require addition of multiple thixotropic time scales to account for multiple time and spatial scales of the structures likely present in this very complex material. Such improvements could also help address the long-time decay in shear stress and hysteresis which are currently missing from the model predictions.

3.7 Appendix

Supplemental information includes figures showing the detailed results from varying the weak modulus layer profile and minimum modulus at the boundary referred in the discussion section.

We compared the results from two other modulus profiles to results obtained from our standard case, which is the segmented profile shown in Fig. 3-4 (orange). The first alternative we checked is just the simple linear profile (blue) where the overall thickness of the near-wall zone is the same but has a larger near-wall gradient. In the second, the segmented linear profile is similar to the one we used before, but the overall thickness is reduced by steepening the gradient outside of the zone closest to the wall, also shown in Fig. 3-4 (yellow). In the first case, by increasing the near-wall gradient and thus increasing the average near-wall modulus, the extent of creep decreases so that the power-law exponent of the time-dependence under small stress is lower and yielding under large stress is suppressed as shown by comparing Fig. 3-15(a) and 3-5(b). On the other hand, if the overall thickness of the weak modulus layer decreases to 10% instead of 20% of the total gap while the near-wall gradient remains the same, there is no significant change in response under both small and large stress, as is observed by comparing Fig. 3-15(b) and 3-5(b).

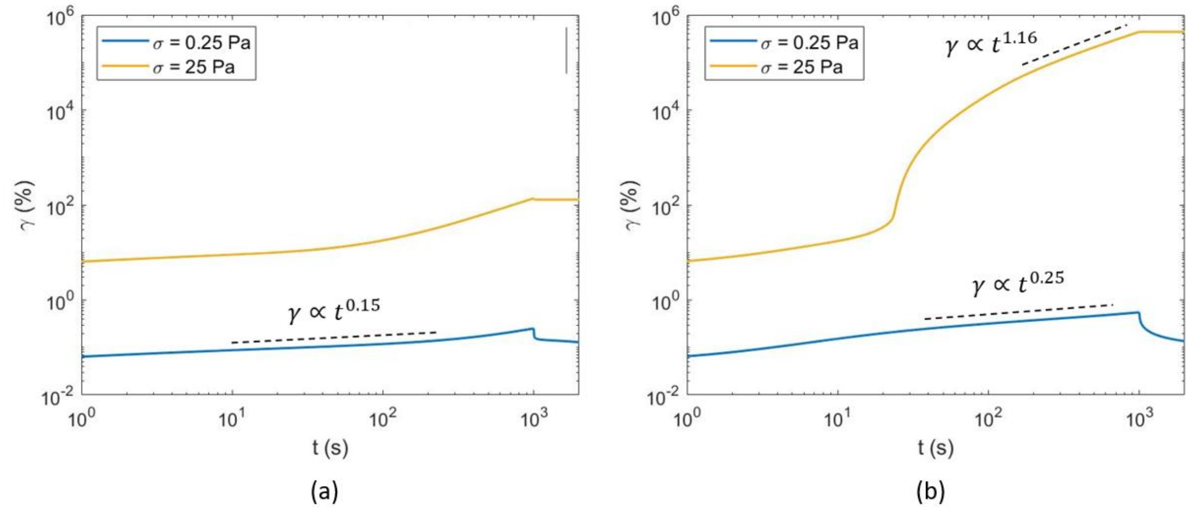

Figure 3-15. Creep, recovery and yielding behavior under a constant stress imposed for 1000 s and thereafter removed for a modulus profile with ***(a)*** *increased near-wall gradient as depicted by the blue dotted linear profile in Figure 4, and* ***(b)*** *reduced overall thickness of reduced-modulus layer, relative to the standard case, as depicted by the yellow long-dash profile in Fig. 3-4.*

Because of this sensitivity to the modulus nearest to the wall, the minimal modulus at the boundary strongly affects both the creep and recovery behavior. Fig. 3-16 presents the results for the simple linear modulus profile extending over 20% of the gap H but with different minimum values at the boundary. A minimum G of 1 Pa, equal to 0.2% of G_0 in the bulk, is high enough to support the imposed stress without exceeding the elastic strain limit γ_c, and so the flow eventually stops, and the strain is completely recovered after the stress is removed as shown in Fig. 3-16. Therefore, to trigger continuous creep and obtain non-recoverable creep, the product of the minimum modulus and the elastic strain limit γ_c needs to be sufficiently small compared to the imposed stress.

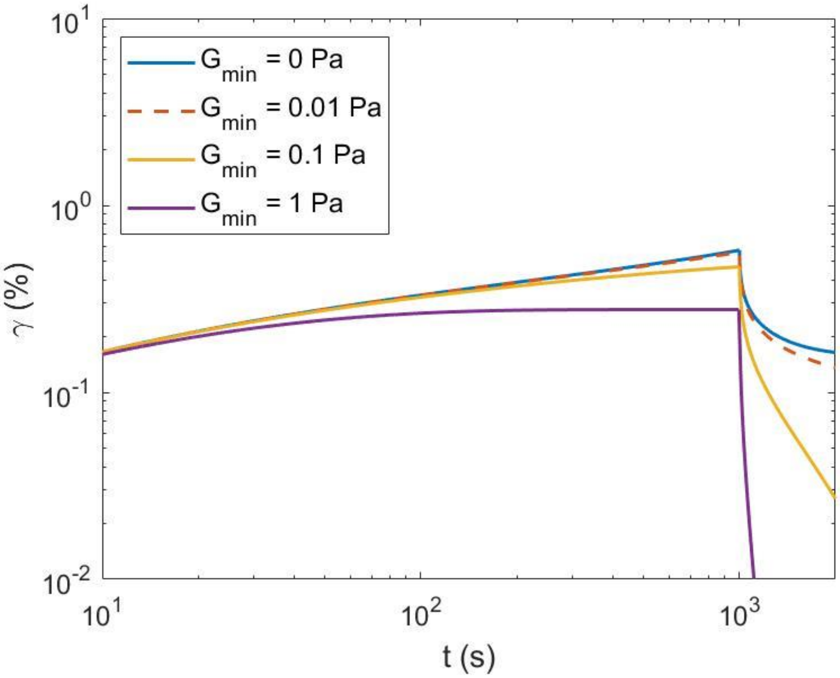

Figure 3-16. Creep, recovery and yielding behavior with constant stress of 0.25 Pa imposed for 1000 s and removed afterwards for different values of the minimum modulus G *at the boundary.*

Here, we demonstrate the potential of our model to be able to predict hysteresis as seen in the constant-shear-rate experiment. Although the non-uniform modulus profile we used is fixed, in reality the weak modulus layer near the boundary will be further weakened during the shear-rate ramp-up scan especially since the shearing is concentrated in the boundary layer, and the structural rebuild corresponding to modulus recovery with reducing shear rate occurs at a much slower time scale than the thixotropic viscosity, leading to hysteresis during the shear-rate ramp-down scan. The exact evolution in modulus profile will be very complex, likely involves reduction of both the minimum value at the boundary and the near-wall gradient, as well as a potential expansion of the weak modulus layer (thickness increase) into the bulk, which can only be derived from the more physical model presented in Section 3.2.1. Therefore, we just used larger $G_{\min}$ at the boundary as a proof of concept to represent a simple case of a "stronger" modulus boundary layer. In Fig. 3-17, an additional curve was derived by using the “stronger” modulus boundary layer meant to represent the material before it has experienced very high shear rates during the ramp-up scan. Significant hysteresis can be observed at low shear rates, which qualitatively resembles the experimental results in Fig. 3-1.

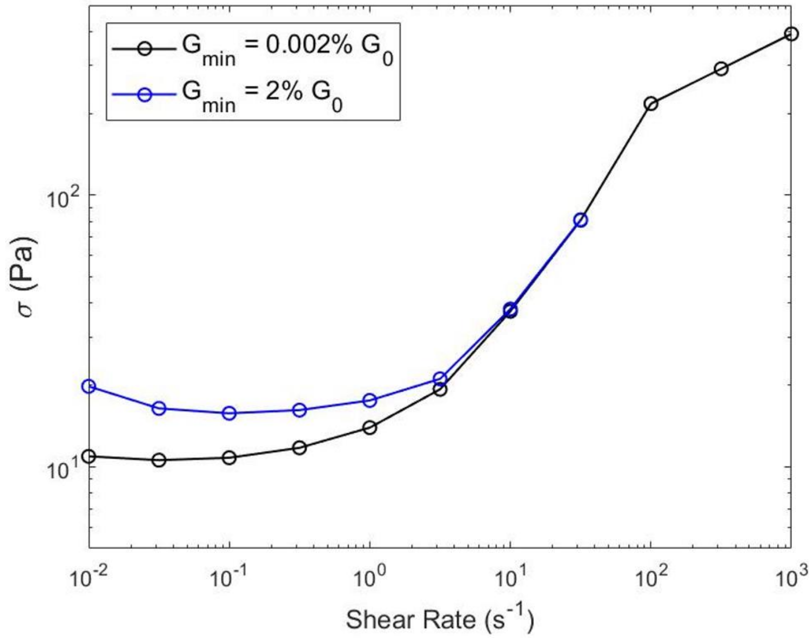

Figure 3-17. Stress vs shear rate curve with two different minimum moduli in the weak-modulus layer.

3.8 Reference

[1] Datta, A., Tanmay, V. S., Tan, G. X., Reynolds, G. W., Jamadagni, S. N., & Larson, R. G. (2020). Characterizing the rheology, slip and velocity profiles of lamellar gel networks. *J. Rheol.*, 64(4), 851-862. https://doi.org/10.1122/8.0000011

[2] Barnes, H. A. (1997). Thixotropy—A review. *J. Non-Newton. Fluid Mech.*, 70(1–2), 1–33. https://doi.org/10.1016/S0377-0257(97)00004-9

[3] Ewoldt, R. H., & McKinley, G. H. (2017). Mapping thixo-elasto-visco-plastic behavior. *Rheol. Acta.*, 56(3), 195–210. http://doi.org/10.1007/s00397-017-1001-8

[4] Jin, L., Wu, Z., Wei, T., Zhai, J., & Zhang, X. (2011). Dye-sensitized solar cell based on blood mimetic thixotropy sol–gel electrolyte. *Chem. Commun.*, 47(3), 997–999. https://doi.org/10.1039/C0CC04285D

[5] Armelin, E., Martı, M., Rud e, E., Labanda, J., Llorens, J., & Aleman, C. (2006). A simple model to describe the thixotropic behavior of paints. *Prog. Org. Coatings*, 57(3), 229–235. https://doi.org/10.1016/j.porgcoat.2006.09.002

[6] Durairaj, R., Ekere, N., & Salam, B. (2004). Thixotropy flow behaviour of solder and conductive adhesive pastes. *J. Mater. Sci.: Mater. Electron.*, 15(10), 677–683. http://doi.org/10.1023/B:JMSE.0000038923.62923.1E

[7] Feys, D., Verhoeven, R., & De Schutter, G. (2008). Influence of thixotropy on pressures required during pumping of concrete. *AIP Conference Proceedings.* 1027, 710. https://doi.org/10.1063/1.2964819

[8] Kropf, C., & Brueninghaus, U. (2001). Thixotropic oral and dental care agents. Google Patent US 20030175217 A1.

[9] Noudeh, G. D., Sharififar, F., Khazaeli, P., Mohajeri, E., & Jahanbakhsh, J. (2011). Formulation of herbal conditioner shampoo by using extract of fenugreek seeds and evaluation of its physicochemical parameters. *African J. Pharmacy Pharmacol.*, 5(22), 2420–2427. http://doi.org/10.5897/AJPP11.121

[10] Dimitriou, C. J., & McKinley, G. H. (2014). A comprehensive constitutive law for waxy crude oil: A thixotropic yield stress fluid. *Soft Matter*, 10(35), 6619–6644. https://doi.org/10.1039/C4SM00578C

[11] Glicerina, V., Balestra, F., Dalla Rosa, M., & Romani, S. (2015). Microstructural and rheological properties of white chocolate during processing. *Food Bioprocess Technol.*, 8(4), 770–776. http://doi.org/10.1007/s11947-014-1443-2

[12] Razavi, S. M. A., & Karazhiyan, H. (2009). Flow properties and thixotropy of selected hydrocolloids: Experimental and modeling studies. *Food Hydrocolloids*, 23(3), 908–912. https://doi.org/10.1016/j.foodhyd.2008.05.010

[13] Li, X., Fang, Y., Zhang, H., Nishinari, K., Al-Assaf, S., & Phillips, G. O. (2011). Rheological properties of gum arabic solution: From Newtonianism to thixotropy. *Food Hydrocolloids*, 25(3), 293–299. https://doi.org/10.1016/j.foodhyd.2010.06.006

[14] Alessandrini, A., Lapasin, R., & Sturzi, F. (1982). The kinetics of thixotropic behaviour in clay/kaolin aqueous suspensions. *Chem. Eng. Commun.*, 17(1-6), 13-22. https://doi.org/10.1080/00986448208911610

[15] Beris, A. N., Stiakakis, E., & Vlassopoulos, D. (2008). A thermodynamically consistent model for the thixotropic behavior of concentrated star polymer suspensions. *J. Non-Newton. Fluid Mech.*, 152(1-3), 76-85. https://doi.org/10.1016/j.jnnfm.2007.10.016

[16] Burgos, G. R., Alexandrou, A. N., & Entov, V. (2001). Thixotropic rheology of semisolid metal suspensions. *J. Mater. Process. Technol.*, 110(2), 164-176.

https://doi.org/10.1016/S0924-0136(00)00731-7

[17] Kelessidis, V. (2008). Investigations on the thixotropy of bentonite suspensions. *Energy Sources, Part A*, 30(18), 1729-1746.
https://doi.org/10.1080/15567030701456261

[18] Dullaert, K., & Mewis, J. (2005). A model system for thixotropy studies. *Rheologica Acta*, 45(1), 23-32.
http://doi.org/10.1007/s00397-005-0439-2

[19] Barry, B. W., & Eccleston, G. M. (1973). Influence of gel networks in controlling consistency of O/W emulsions stabilised by mixed emulsifiers. *Journal of Texture Studies*, 4(1), 53-81.
https://doi.org/10.1111/j.1745-4603.1973.tb00654.x

[20] Iwata, T. (2017). *Cosmetic Science and Technology: Theoretical Principles and Applications*. Elsevier.

[21] Fielding, S. M., Sollich, P., & Cates, M. E. (2000). Aging and rheology in soft materials. *J. Rheol.*, 44, 323-369.
https://doi.org/10.1122/1.551088

[22] Coussot, P. (2007). Rheophysics of pastes: A review of microscopic modelling approaches. *Soft Matter*, 3, 528-540.
https://doi.org/10.1039/B611021P

[23] Mewis, J., & Wagner, N. J. (2009). Thixotropy. *Adv. Colloid Interface Sci.*, 147-148, 214-227.
http://doi.org/10.1016/j.cis.2008.09.005

[24] Larson, R. G. (2015). Constitutive equations for thixotropic fluids. *J. Rheol.*, 59, 595-611.

https://doi.org/10.1122/1.4913584

[25] Coussot, P., Nguyen, Q. D., Huynh, H. T., & Bonn, D. (2002). Viscosity bifurcation in thixotropic, yielding fluids. *J. Rheol.*, 46, 573-589.

https://doi.org/10.1122/1.1459447

[26] Jain, A., Singh, R., Kushwaha, L., Shankar, V., & Joshi, Y. M. (2018). Role of inertia and thixotropy in start-up flows of aging soft materials: Transient dynamics and shear banding in a rate-controlled flow field. *J. Rheol.*, 62, 1001.

https://doi.org/10.1122/1.5023305

[27] Wei, Y., Solomon, M. J., & Larson, R. G. (2016). Quantitative nonlinear thixotropic model with stretched exponential response in transient shear flows. *J. Rheol.*, 60, 1301.

https://doi.org/10.1122/1.4965228

[28] Wei, Y., Solomon, M. J., & Larson, R. G. (2018). A multimode structural kinetics constitutive equation for the transient rheology of thixotropic elasto-viscoplastic fluids. *J. Rheol.*, 62, 321.

https://doi.org/10.1122/1.4996752

[29] Sollich, P., Lequeux, F., Hebraud, P., & Cates, M. E. (1997). Rheology of soft glassy materials. *Phys. Rev. Lett.*, 78, 2020–2023.

https://doi.org/10.1103/PhysRevLett.78.2020

[30] Fielding, S. M., Cates, M. E., & Sollich, P. (2009). Shear banding, aging and noise dynamics in soft glassy materials. *Soft Matter*, 5, 2378–2382.

https://doi.org/10.1039/B812394M

[31] Paredes, J., Shahidzadeh-Bonn, N., & Bonn, D. (2011). Shear banding in thixotropic and normal emulsions. *J. Phys. Condenss,* 23, 284116.

https://doi.org/10.1088/0953-8984/23/28/284116

[32] Joshi, Y. M. (2014). Dynamics of colloidal glasses and gels. *Annu. Rev. Chem. Biomol. Eng.*, 5, 181–202. https://doi.org/10.1146/annurev-chembioeng-060713-040230

[33] de Gennes, P. G., & Prost, J. (1993). *The physics of liquid crystals*. Oxford University Press.

[34] Larson, R. G., & Doi, M. (1991). Mesoscopic domain theory for textured liquid crystalline polymers. *J. Rheol.*, 35, 539. https://doi.org/10.1122/1.550180

[35] Larson, R. G. (1999). *The structure and rheology of complex fluids*. Oxford University Press.

[36] Denn, M. M. (1980). *Process fluid mechanics*. Prentice-Hall.

[37] Frederick, C. O., & Armstrong, P. (2007). A mathematical representation of the multiaxial Bauschinger effect. *Materials at High Temperatures*, 24, 1–26. http://doi.org/10.1179/096034007X207589

[38] Dimitriou, C. J., & McKinley, G. H. (2014). A comprehensive constitutive law for waxy crude oil: a thixotropic yield stress fluid. *Soft Matter*, 10(35), 6619-6644. https://doi.org/10.1039/C4SM00578C

[39] Wei, Y., Solomon, M. J., & Larson, R. G. (2019). Time-dependent shear rate inhomogeneities and shear bands in a thixotropic yield-stress fluid under transient shear. *Soft Matter*, 15, 7956. https://doi.org/10.1039/C9SM00902G

[40] Mujumdar, A., Beris, A. N., & Metzner, A. B. (2002). Transient phenomena in thixotropic systems. *J. Non-Newton. Fluid Mech.*, 102, 157-178. https://doi.org/10.1016/S0377-0257(01)00176-8

[41] Olmsted, P.D. (2008). Perspectives on shear banding in complex fluids. *Rheol. Acta*. 47, 283–300. http://doi.org/10.1007/s00397-008-0260-9

Chapter 4 Coarse-grained Modeling of Pharmaceutical Cocrystal Growth from Melt with Iterative Boltzmann Inversion

This Chapter is based on an EFRI project funded by NSF and has not been submitted for publication yet. We are grateful for advice from Taraknath Mandal in the work presented in this chapter.

4.1 Introduction

The crystallization of organic molecules is of great importance in various applications, particularly in the pharmaceutical industry as it plays a crucial role in the synthesis process of active pharmaceutical ingredients (APIs) as well as their in vivo release mechanism. Unfortunately, many APIs have poor solubility and slow dissolution kinetics, leading to reduced bioavailability, which makes them unsuitable as drug candidates. To address this issue, co-crystallization has emerged as an effective crystal engineering tool for modifying the crystal structure and properties to solve drug formulation and manufacturing problems without changing the molecular structure of APIs.[1]

Pharmaceutical cocrystals are solids of neutral crystalline single phase composed of API and another pharmaceutically acceptable conformer other than solvate or simple salts, generally in a stoichiometric ratio. Although various methods for cocrystal formation have been reported, such as solvent evaporation, solution crystallization, slurry conversion, and melt crystallization, little consistency has been found in the application of different preparation methods.[1] Recently, our collaborators have developed a novel gas-assisted desublimation process that produces single crystal and cocrystal of APIs with reduced particle size.[2] The solvent-free process has the potential to enable high-throughput, continuous manufacturing, and personalized dosage simultaneously. To further develop these new drug processing methods and enhance the bioavailability of APIs, a better understanding of the nature of co-crystallization of organic molecules and polymorph selection is necessary and of great interest to the pharmaceutical industry.

While experimental investigations can provide a phenomenological understanding of crystallization, the detailed nucleation and growth mechanism at the atomistic level is challenging to study using experiments alone. However, modern molecular simulation approaches have become increasingly useful in studying crystal growth.[3] The main challenge with molecular simulations is that nucleation and crystal growth are generally rare events that require very long timescales beyond the range accessible with ordinary atomistic simulations. To overcome this problem, rare-event sampling methods such as umbrella sampling,[4] metadynamics,[5] and forward flux sampling[6] have been developed as useful techniques to investigate crystallization mechanisms. The principle of these constrained simulation methods is to apply a biased potential to the system to either drive it along a predetermined reaction coordinate of appropriate collective variables or to prevent it from repeating previously explored trajectories and force it to explore higher energy states to overcome the kinetic barriers.[7] Therefore, the efficacy of these methods heavily relies on the accuracy of the choice of collective variables, which should properly describe the occurrence of the rare events of interest.

To date, advanced simulation methods have mostly been used to investigate the crystallization of relatively simple organic molecules. For example, the nucleation and growth kinetics of urea crystal from both aqueous solution and melt have been thoroughly studied with atomistic molecular dynamics (MD) simulation, and the selective effect of additional growth inhibitors was revealed by evaluating the free energy of adsorption using well-tempered metadynamics simulations.[8-12] However, organic drug molecules often have larger sizes and more complex crystal structures, where even biased simulation methods could be inefficient due to the large number of degrees of freedom of the molecules in the unit cell. Santiso et al. developed a general set of order parameters that can differentiate between melt and different crystal polymorphs and combined them with the String Method in Collective Variables (SMCV) to investigate the crystallization of relatively complex organic molecules.[13,14] SMCV has emerged as a useful method to determine the minimal free energy pathway of rare events described by complex collective variables.[15] The nucleation energy barrier between two polymorphs of sulfamarezine in different solvents was computed, and found to qualitatively agree with the experimental results.[16] However, the detailed growth kinetics are difficult to obtain from their method, and investigating pharmaceutical cocrystals would further complicate the issue in terms of selecting appropriate order parameters as effective collective variables that could drive the transition between states of mixtures of two different types of organic molecules. As a result, there is very limited contribution for cocrystal growth from molecular simulations compared to extensive experimental investigations. While Anuar et al. simulated a pre-built cocrystal of carbamazepine and succinic acid, only a morphology prediction was made using the classic attachment energy theory.[17] Another approach focused on understanding the crystallization and growth kinetics of simple model systems, such as hard spheres or spherical particles with simple interaction potentials.[18] However, while these sphere-based simple models are often used for colloidal and polymer systems, their lack of molecular detail in describing complex drug molecules prevents them from appropriately representing the real pharmaceutical systems. In general, it is extremely challenging to directly simulate the crystallization kinetics of pharmaceutical cocrystals with molecular simulations.

Coarse-graining is an approach that combines some of the advantages of atomistic simulation and sphere-based simple models. It offers extended time and length scales, making it less susceptible to kinetic trapping in simulation, while retaining the molecular details to a certain degree that are relevant to the real system. There have been coarse-grained (CG) models well-developed for various biomolecules including lipids, proteins, DNA and polymers.[19] For example, the widely used MARTINI forcefield uses a roughly four-to-one mapping of non-hydrogen atoms per coarse-grained bead and has different bead types for various functional groups, which differ in charge and hydrophobicity.[20] However, the interactions between the CG beads in MARTINI are described with relatively simple Lennard-Jones potentials that are parameterized for the fluid phase. Therefore, the use of MARTINI forcefield for simulating the solid phase of materials, especially drug molecules, has been very limited because it could not accurately reproduce the correct crystal structures. In an attempt to overcome this limitation, Mandal et al. reported a systematic coarse-graining scheme based on iterative Boltzmann inversion (IBI) to study crystallization and predict potential polymorphs of small organic molecules.[7] They developed coarse-grained models for several pharmaceutically relevant molecules and were able to simulate the growth of a crystalline slab from the melt. Given that the IBI scheme can be generalized to other crystal systems and the solvent-free environment matches with the experiment condition of our collaborators, we adopted the method of Mandal et al. and developed coarse-grained potentials for the cocrystal of carbamazepine (CBZ) and succinic acid (SA), a system of significant pharmaceutical interest with non-trivial complexity that was produced via the gas-assisted desublimation process.

In the rest of this chapter, we describe the methodology of our coarse-grained model for CBZ-SA cocrystal and prior investigations with atomic simulations. We then report the growth kinetics of different cocrystal facets obtained by direct simulation and analyze single molecule adsorption on the crystal surface using well-tempered metadynamics. The chapter concludes with a summary of our findings and future directions.

4.2 Method

4.2.1 Atomistic simulation

Fully atomistic simulations of the cocrystal of carbamazepine and succinic acid were conducted to provide structural information for deriving the coarse-grained model. The chemical structures of the two molecules are shown in Figs. 4-1(a) and 4-1(b) respectively. The cocrystal structure was obtained from the Cambridge Crystallographic Data Centre (CCDC) with the reference code of XOBCIB. The CBZ-SA cocrystal has a 2:1 stoichiometric ratio and a monoclinic lattice with cell parameters of $a = 1.7730$ nm, $b = 0.5217$ nm, $c = 2.0753$ nm, $\beta = 103.35°$, $\alpha = \gamma = 90°$, as shown in Figure 4-1(c). The initial structures of the cocrystal in simulations were built by replicating the unit cell along the three principal directions. A system comprising 512 carbamazepine and 256 succinic acid molecules with X, Y, and Z dimensions of 7.111, 6.523, and 4.155 nm respectively was used to develop coarse-grained potentials, with interaction parameters from the OPLS-AA force field to model the two molecules.[21] The Verlet scheme was used for neighbor searching,[22] with a cutoff distance of 1.4 nm, while the Particle-Mesh-Ewald (PME) method was used to calculate long-range electrostatic interactions,[23] and periodic boundary conditions were enforced along all three directions. Prior to the regular molecular dynamics simulations, the system underwent energy minimization using the conjugate gradient method and a short 1 ns NVT simulation at 290 K, followed by 10 ns of equilibrium simulation in the NPT ensemble at the same reference temperature and a reference pressure of 1 bar. The 20 ns production runs for data collection used Nose-Hoover temperature coupling and anisotropic Parinello-Rahman pressure coupling methods. The LINCS constraint[24] was applied on all bonds containing hydrogen atoms, and a time step of 1 fs was used. All simulations were conducted using the GROMACS 2019.6 simulation package.[25]

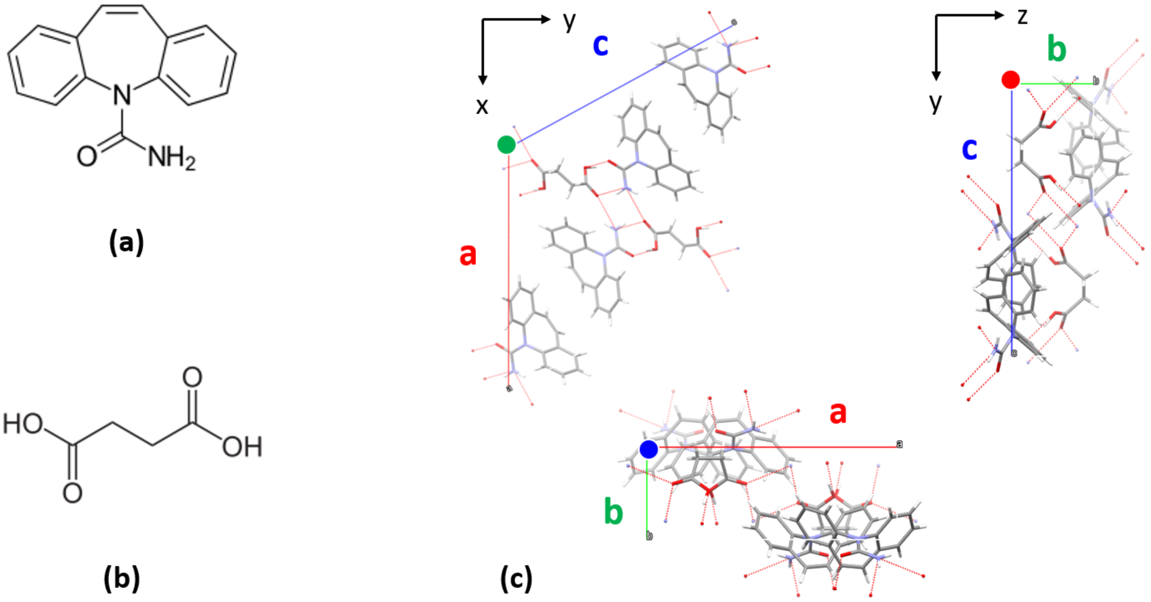

(a)

(b)

(c)

Figure 4-1. Chemical structure of ***(a)*** *carbamazepine, and* ***(b)*** *succinic acid.* ***(c)*** *The lattice structure of CBZ-SA cocrystal view along each of three directions. Note that Y axis is not parallel to side c due to the monoclinic lattice. The unit cell of CBZ-SA cocrystal contains four carbamazepine and two succinic acid molecules with hydrogen bonding represented by red dashed lines.*

4.2.2 Molecular structure of coarse-grained models

Carbamazepine is a non-planar molecule consisting of three aromatic rings, each aligned in different planes, and the middle azepine ring is connected to an amide side group that lies in a fourth plane as shown in Fig. 4-2(a). Initially, coarse-graining was attempted using a three-bead model for carbamazepine, as illustrated in Fig. 4-2(b), with two CG beads of the same type representing the benzene ring and half of the azepine ring while a third bead of a different type represented the amide group. Succinic acid was modeled as a symmetric two-bead molecule, resulting in three CG bead types for the entire cocrystal. While this simple coarse-grained model could maintain a pre-built cocrystal structure, it was unable to simulate the formation of new crystal layers from the melt mixture of the two components over an existing cocrystal surface as a seed. The simplicity and the additional symmetry from the CG model were the source of the problem, as the three-bead carbamazepine is always planar and the two-bead succinic acid is basically a rod, which deviates from the atomistic structure of the two molecules and does not have the complexity to capture the driving force for cocrystal growth.

Instead, a four-bead carbamazepine model was used, as shown in Fig. 4-2(c), with the azepine ring represented by bead “Z”, the two benzene rings represented by two beads of the same type “B”, and the amide group represented by a third type of bead “A”. The CG beads were connected by pseudo bonds, and their positions were obtained from the centers of mass (COMs) of the corresponding atomistic structures. We also note that in the atomistic model, the carbamazepine is asymmetric with respect to the middle azepine ring due to the orientation of the amide group relative to each of the two benzene rings. This results in the two different conformations of carbamazepine molecules which form pairs in the crystalline state, but each molecule can convert from one conformation into one another in the melted state. Therefore, the distances between the COMs of the amide group and each of the two benzene rings are slightly different, but they are treated as the same in the coarse-grained model since the amide group is simplified into a sphere, so that the average bond length is used. While the individual aromatic ring orientations are lost due to the spherical nature of the CG beads, they are no longer co-planar as is the case in the less realistic three-bead model of carbamazepine. Similar, a second bead type “E” was added to the succinic acid model to represent the ethylene group, and the two carboxylic acid groups were represented each by a bead type “C”. As a result, the CG models for CBZ-SA cocrystal have 5 different bead types (A, B, Z, C, E).

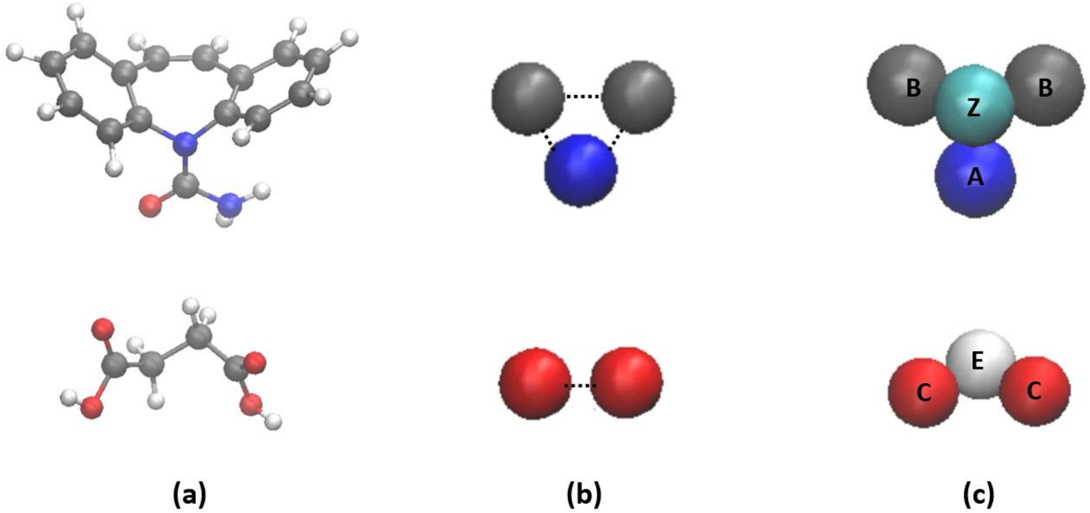

Figure 4-2. Different models for carbamazepine and succinic acid: ***(a)*** *all-atom model,* ***(b)*** *initial coarse-graining attempt of three-bead carbamazepine and two-bead succinic acid, and* ***(c)*** *coarse-grained model of four-bead carbamazepine and three-bead succinic acid.*

4.2.3 Development of the coarse-grained parameters

The behavior of the coarse-grained beads is determined by bonded potentials for intramolecular interactions and non-bonded potentials for intermolecular interactions. Specifically, the potential for the pseudo bonds between the beads is defined using a harmonic function, as shown below in Eq. 4.1:

$$V_{bond} = \frac{1}{2} K_b (r - r_0)^2 \tag{4.1}$$

where K_b represents the force constant and r_0 represents the equilibrium bond length. These values were chosen to ensure that the coarse-grained bond-length distributions matched closely the corresponding atomistic results.

The development of non-bonded interaction potentials is a crucial and challenging aspect of our crystallization simulation. Coarse-graining removes molecular details that are essential to the formation of specific crystal structures, and therefore simulations with coarse-grained force fields may not lead to the correct crystal form, as discussed earlier in the case of MARTINI. To compensate for the lost molecular structural information, we utilized the Iterative Boltzmann Inversion (IBI) method with known crystal structural information as input to generate relatively long-range non-bonded potentials. The method was first developed by Reith et al.[26] and has been widely used to derive coarse-grained potentials for various systems,[27-30] including single crystals of organic molecules in recent work.[7] In our work, we extended the application of the IBI method to the co-crystallization of two pharmaceutical components. To generate the initial guess for the coarse-grained potentials, we used the radial distribution functions (RDFs) between the non-bonded units mapped from atomistic simulations as the target observables of the IBI scheme by Eq. 4.2:

$$V_{ini} = -\alpha k_b T \, log \, (g_{aa}) \tag{4.2}$$

where g_{aa} is the RDF for the center of mass of the portions of the molecule represented by each of the CG beads from all-atom simulations (including $g_{aa,A-A}$, $g_{aa,A-B}$, etc.). k_b and T are the Boltzmann constant and system temperature, respectively. α is a scaling factor that is typically set in the range of 0.1 to 0.25 to adjust the magnitude of the potential and prevent abrupt changes in the potential during the iteration steps later. The non-bonded interaction potential between two beads was generated for each pair of CG beads, including two beads of the same type as well as two beads of different types, using the corresponding g_{aa} from all-atom simulations. The coarse-grained potentials obtained from the initial guess were then used to run coarse-grained simulations, which were iteratively improved based on Eq. 4.3:

$$V_{i+1} = V_i - \alpha k_b T \, log\left(\frac{g_{aa}}{g_{cg,i}}\right) \tag{4.3}$$

where V_{i+1} represents the updated potential after the (i+1)th iteration based on the potential V_i from the previous round of iteration and the RDF $g_{cg,i}$ is extracted from the corresponding coarse-grained simulation. The ultimate goal is to reproduce the RDFs obtained from the atomistic simulations when running coarse-grained simulations, as shown in Fig. 4-3.

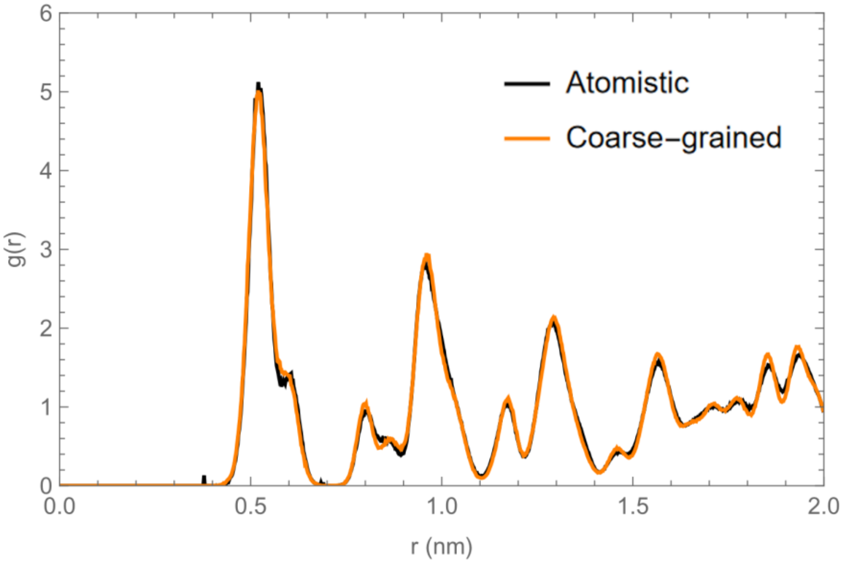

Figure 4-3. Comparison of the atomistic RDF between two type "A" beads with the corresponding coarse-grained RDF. The full set of RDFs are included in the Appendix.

The coarse-grained model for CBZ-SA cocrystal with five bead types requires a total of 15 pairwise nonbonded interaction potentials. After three iterations, the non-bonded potentials converged and were truncated at 1.75 nm using a cubic spline interpolation method. The truncation is required for the relatively long-range potentials to stabilize a pre-formed cocrystal, and the cutoff distance was chosen so that the system can remain condensed even when the molecules are in the molten state. The final set of comparisons between atomistic and coarse-grained RDFs are included in the Appendix. Unlike a simple Lenard-Jones (LJ) potential, the non-bonded potentials derived from the complex multi-peak RDFs could not be fitted to any simple analytical function. Therefore, they were tabulated and their values between tabulation points were interpolated using a cubic spline function. All coarse-grained simulations performed in this work used stochastic dynamics, hence the motion of the coarse-grained particles was governed by the Langevin equation. The temperature and pressure coupling methods were the same as the ones used in atomistic simulations described in Section 4.2.1.

4.3 Results and Discussion

4.3.1 Investigation with all-atom model

In addition to the simulations used to develop the coarse-grained models, further all-atom simulations were conducted to gain insight into the crystallization process of CBZ-SA cocrystal and, the simpler case, single crystal of carbamazepine. A CBZ-SA cocrystal system consisting of 32 unit cells periodic in three dimensions was constructed and heated from 290 K at a rate of 5 K/ns. The simulation setup is described in Section 4.2.1. The melting occurred at approximately 640 K, which is significantly higher than the experimental value of 462 K. However, this is not surprising due to the relatively fast heating rate in the simulation and the lack of any defect in the initial configuration of the system. In contrast, a cocrystal slab with the same number of molecules but with the (0 0 2) facet exposed exhibited a more reasonable melting point of around 455 K in simulation. A block of disordered molecules in the melted state was placed on a pre-built cocrystal slab, but no crystal growth was observed at different temperatures during the 40 ns simulation runs, as expected given the challenges with directly simulating crystallization with atomistic models discussed earlier. The stability of different facet was also investigated, and it was found that the surface molecules of (1 0 -1) remained in the ordered state at temperatures below 400 K, while those of the (0 1 0) and (0 0 2) facets became disordered.

Inspired by classical crystal growth theory and the step nucleation and layer completion process, we sought to investigate the crystallization of a single disordered surface layer and the attachment of a single molecule to an existing crystal surface. To simplify the problem, we focused on a single crystal of carbamazepine, rather than the more complex CBZ-SA cocrystal. A single carbamazepine molecule near the crystal surface was simulated to investigate the preferred site and effect of molecule orientation and conformation on surface adsorption. The results showed that the carbamazepine molecule bounced around between different crystalline sites at the crystal surface, and no consistent trend or favored site could be concluded. There are two types of crystalline sites corresponding to carbamazepine with different amide conformation. The adsorption was semi-stable at times, but the molecule could also be trapped when its conformation did not match the crystalline site it temporarily sat on. Additionally, the evolution of a disordered carbamazepine layer at the crystal surface was simulated, but defects observed in the prior study of single molecule adsorption (molecules sitting on the wrong site) and kinetic trapping prevented the formation of a new ordered layer even after extended simulation runs. Therefore, coarse-graining methods are necessary to achieve direct crystal growth of small organic molecules in molecular simulations.

4.3.2 Cocrystal growth from coarse-grained model

The structure of CBZ-SA cocrystal obtained from coarse-grained simulations was examined first. The change in lattice parameters was less than 1%, and all the radial distribution functions matched the corresponding atomistic results in the Appendix. The carbamazepine and succinic acid molecules in the cocrystal form remained stable during 40 ns long simulations. In theory, different crystal facets have different growth rates, which determine the crystal morphology as slower growing facets will have larger surface area. While primitive morphology prediction can be made using BFDH and attachment energy theories,[31,32] the coarse-grained model enabled direct observation of the growth of different crystal facets in simulation. Since nucleation events are typically associated with high energy barriers, the time and length scales required to simulate the formation of a large enough crystal with well-defined shape and facets could be prohibitive even with our coarse-grained model. Therefore, crystalline slabs with different facets exposed to the melt were used as seeds, a common practice to investigate crystal growth mechanisms in simulations. We focused on the (0 1 0), (0 0 2), and (1 0 -1) facets since they were predicted to have different attachment energy, with the (1 0 -1) facet having the slowest growth. Fig. 4-4 shows that, for all three facets, the molten molecules reoriented themselves to fit the cocrystal structure, and the cocrystal slab steadily grew into the melt, which were not achieved in atomistic simulations. As discussed earlier, the shape and multiple bead types of the coarse-grained model captured some of the anisotropy of the interaction of the molecules with their neighbors, and the faster dynamics in coarse-grained simulation enabled growth of the pre-assembled crystal slab. To confirm the robustness of the cocrystal growth, several simulations with different numbers of molecules and cross-sectional areas were carried out at different temperatures. In all cases except one, which will be discussed shortly, a steady growth of CBZ-SA cocrystal was observed.

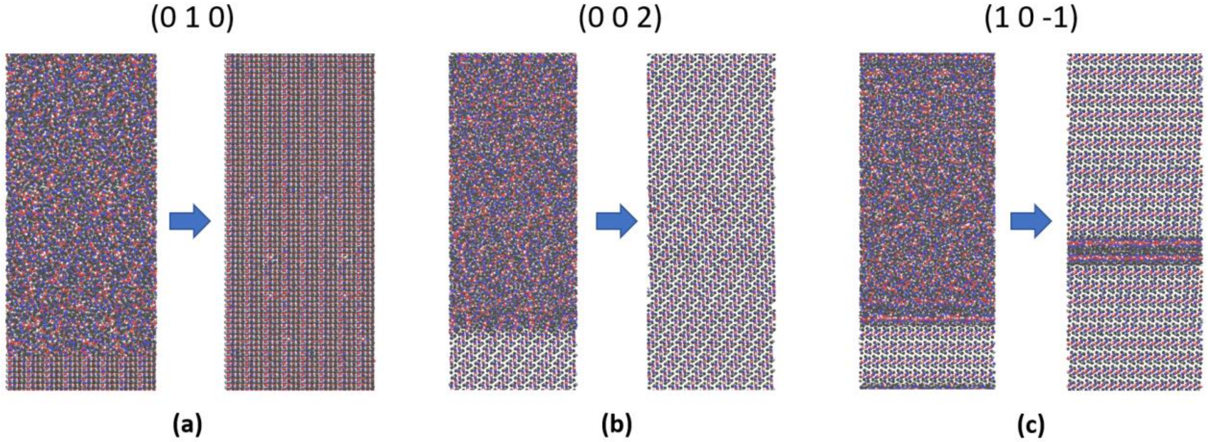

Figure 4-4. Snapshots of the simulation box at 0 ns (left) and 20ns (right) for the growth of ***(a)*** *(0 1 0),* ***(b)*** *(0 0 2), and* ***(c)*** *(1 0 -1) facets at 390 K.*

To monitor the number of molecules in crystalline state, we followed a previously used definition for the degree of crystallinity in single crystal by analyzing the major component carbamazepine only.[7] The degree of crystallinity (τ_i) of the *i*th carbamazepine molecule is given by Eq. 4.4:

$$\tau_i(t) = \frac{1}{n_i(t)} \sum_{j=1}^{n_i(t)} exp\left(-\frac{\left(\theta_{ij}(t) - \theta_0\right)^2}{2\sigma^2}\right) + exp\left(-\frac{\left(\theta_{ij}(t) - \theta_1\right)^2}{2\sigma^2}\right) \quad (4.4)$$

where n_i(t) is the number of nearest neighbors of the *i*th molecules within a cut-off distance of 0.8 nm. θ_{ij} is the angle between the ‘‘internal vector’’ of the *i*th molecule and that of its *j*th neighbor. The internal vector of carbamazepine is defined to be the vector extending from the center of bead “Z” to bead “A”. In the CBZ-SA cocrystal, the internal vectors of neighboring molecules form an angle of either $\theta_0 = 5°$ or $\theta_1 = 45°$. The standard deviation σ was taken to be 15°. Through the analysis of trajectories from simulations of a perfect cocrystal and fully melted molecules, we have determined that the average value of τ equals 1.0 for the cocrystal system (τ_{cry}) and 0.55 for the fully melted state (τ_{melt}). With this information, the percentage of molecules in cocrystal state is defined by Eq. 4.5:

$$Crystal\,\% = \frac{\tau - \tau_{melt}}{\tau_{cry} - \tau_{melt}} \tag{4.5}$$

and its time evolution is used to characterize the grow rates of different crystal facets.

The cocrystal growth simulations of (0 1 0), (0 0 2), and (1 0 -1) facets presented here all began with an equivalent number of crystalline molecules in the seed cocrystal and three times more melted molecules, and all three systems possess a comparable cross-sectional area in the growth direction between 45 to 50 nm^2 with an aspect ratio close to 1. The simulations were conducted at 390 K and 440 K to prevent nucleation away from the surface, which may occur in the melt at lower temperatures and could disrupt crystal growth over the facet, while higher temperatures that could cause the cocrystal slab to melt were also avoided. The change of the percentage of crystalline molecules in the system is plotted in Fig. 4-5, which starts at around 25% because of the 1:3 crystal to melt ratio. Although there is not a significant difference between the growth rates of the (0 1 0) and (0 0 2) facet, it is evident that the (1 0 -1) facet has the slowest growth rate at 390 K, and it failed to grow at all at 440 K. Additionally, for the (0 1 0) and (0 0 2) facets, the number of carbamazepine molecules that transition into the crystalline state increases nearly linearly until completion. Conversely, the curve for the (1 0 -1) facet in Figure 4-5(a) exhibits multiple points with abrupt decreases in slope, indicating that each new layer at the surface requires a short time to become fully ordered, potentially associated with a higher energy barrier for the formation of each layer.

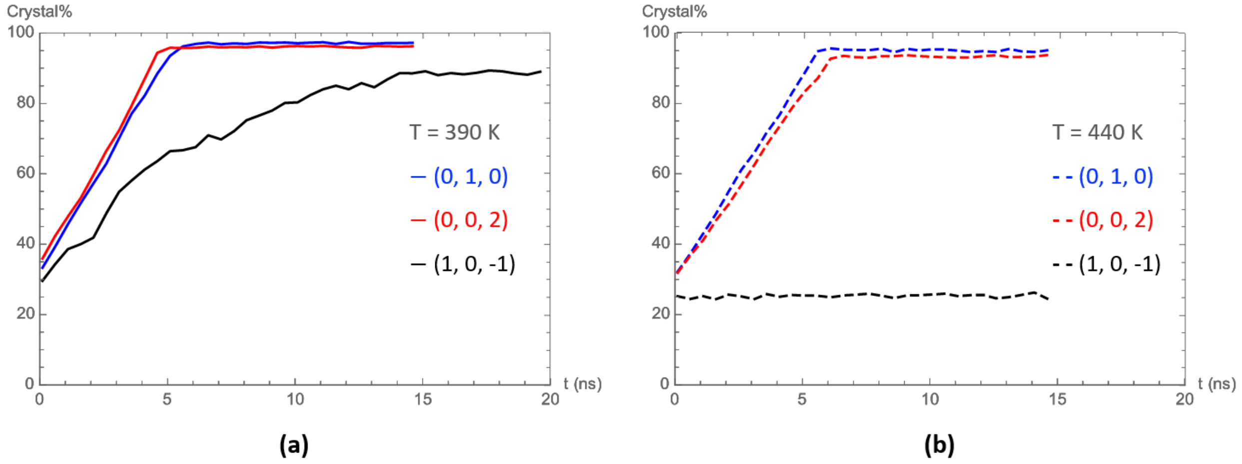

*Figure 4-5. Typical time dependence of percentage carbamazepine molecules in the crystalline state for the three different facets at **(a)** 390 K, and **(b)** 440 K.*

The average growth rates per unit surface area during the first 4 ns of simulation are summarized in Table 4-1. The slowest growth of (1 0 -1) facet qualitatively agrees with the prediction from attachment energy calculations[17] and the cocrystal morphology observed in experiments,[33] where the (1 0 -1) facet is anticipated to have the lowest attachment energy with the largest surface area. This observation also corresponds to the stability of the (1 0 -1) facet that we identified in atomistic simulations, indicating that it is energetically favored to be the exposed surface. The cessation of growth of the (1 0 -1) may be attributed to the more vigorous thermal motion at higher temperature, which hinders the molecules from becoming fully ordered at the surface, and the slower growing (1 0 -1) could be more susceptible to such effect. The temperature dependance of the growth rates over different facets is complicated since a higher temperature reduces the driving force for crystallization but at the same time helps the system to overcome the energy barrier more easily.[7] Therefore, additional simulations are necessary for further analysis.

Table 4-1. The average growth rate of the three facets during the first 4.0 ns of simulation, in units of molecules/ns-nm^2.

	(0 1 0)	**(0 0 2)**	**(1 0 -1)**
390 K	8.7	8.9	5.3
440 K	8.0	7.3	0

4.3.3 Analysis with metadynamics

To investigate the reason for the much slower growth of (1 0 -1) facet, we conducted well-tempered metadynamics (WT-MD) simulations[34] to study the adsorption of a single molecule on each of the three facets, which is a crucial step for the formation of new crystal layers. Metadynamics is a widely used method for studying rare events by adding bias potentials to the simulations to generate the free energy surface (FES) as a function of two collective variables (CVs). In this case, the first CV (referred as CV1) is the distance between the center of mass of the molecule and the crystal surface. The second CV (CV2) is defined as the relative angle between an orientation vector of the molecule and the vector normal to the crystal surface as illustrated in Fig. 4-6. A harmonic potential constraint was applied to the crystalline slab to keep the surface structure ordered, and a wall potential at a maximum distance of 3 nm was used to prevent the molecule from crossing the periodic boundary. The WT-MD simulations were performed using the PLUMED[35] software in conjunction with the GROMACS simulation package. The goal of using these CVs is to determine the favored orientation of the molecule adsorbed at the surface and whether that orientation aligns with the molecular orientation in bulk crystal. The assumption is that if those are different, an orientation change is required for the adsorbed molecule to turn into the crystalline state, which could lead to a slower growth rate of a given facet.

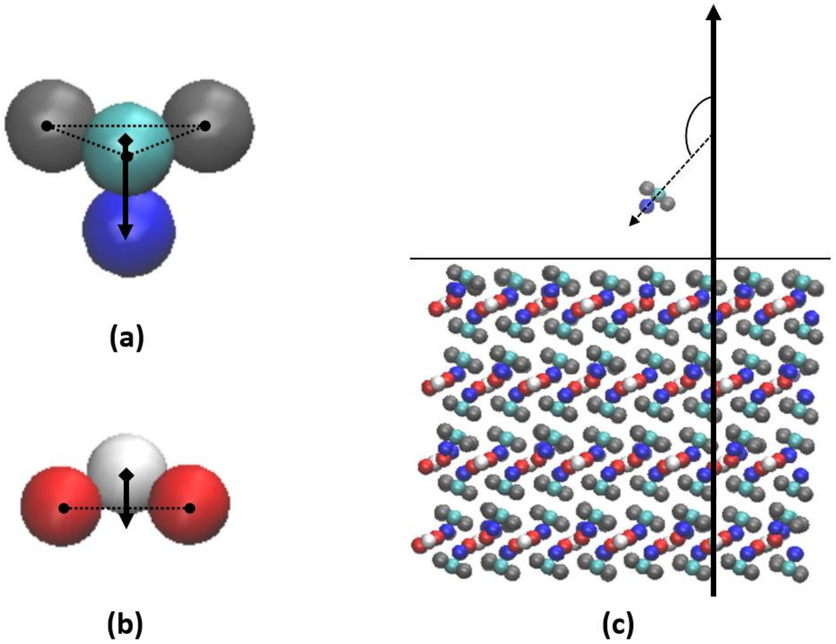

Figure 4-6. Definition of the internal vector for ***(a)*** *carbamazepine and* ***(b)*** *succinic acid.* ***(c)*** *A schematic diagram of well-tempered metadynamics simulation of single-molecule adsorption. The first CV is the distance between the surface of interest and the internal vector of the molecule, and the second CV is the angle between the internal vector and a vector perpendicular to the surface of interest.*

We first examined the orientation of carbamazepine molecules in the cocrystal. Figs. 4-7(a) - 4-7(c) depict the structure of three crystal slabs, each with a different facet exposed at the top surface. The orientation vector of carbamazepine is defined as the vector connecting the center of mass of the three CG beads representing the aromatic rings to the fourth amide CG bead to highlight the effect of hydrogen bonding. The orientation of carbamazepine molecules in each crystal slab is labeled in Figs. 4-7(a) - 4-7(c), and the distribution of the angle between the orientation vector and the upward-pointing perpendicular vector is plotted as histograms in Figs. 4-7(d) - 4-7(f). In all three cases, two preferred orientations exist for carbamazepine in the cocrystal. The first has the orientation vector pointing upwards with an angle less than $\frac{\pi}{2}$ (labeled as the white arrows), and the second has the vector pointing downward with an angle greater than

$\frac{\pi}{2}$ (labeled as the black arrows). The mean values summed over the two peaks in Figs. 4-7(d) - 4-7(f) add up approximately to π since there are equal numbers of carbamazepine molecules taking opposite orientations in the cocrystal, as shown in Figs. 4-7(a) - 4-7(c). The distributions are not symmetric about $\pi/2$ because the binning was not centered about this value.

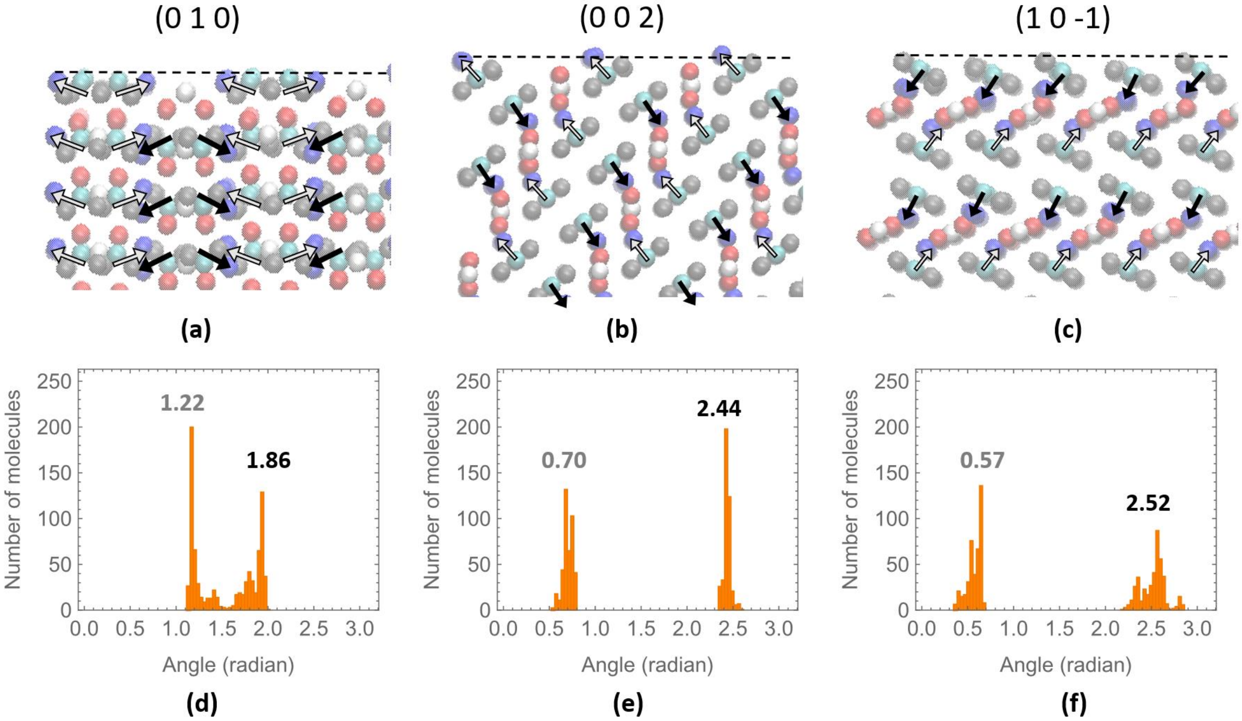

Figure 4-7. The crystal structure near the surface for ***(a)*** *(0 1 0),* ***(b)*** *(0 0 2), and* ***(c)*** *(1 0 -1) facets. The internal vector of carbamazepine molecules is labeled with white and black arrows. The distribution of the relative angle of the internal vector is plotted with the mean value of the peaks for* ***(d)*** *(0 1 0),* ***(e)*** *(0 0 2), and* ***(f)*** *(1 0 -1) facets. The gray number corresponds to the white arrows and the black number corresponds to the black arrows.*

Next, we introduced a single carbamazepine molecule, positioned 0.7 nm away from the center of the surface, to perform WT-MD simulations to map the free energy surface (FES) of its two collective variables. The FES diagrams for the three facets are shown in Fig. 4-8, with black and gray dotted lines overlaid to represent each of the two preferred orientation angles in the crystalline state for each facet as a comparison. For the (0 1 0) and (0 0 2) facets, the minimum of the FES is located near the surface at an angle greater than $\frac{\pi}{2}$ crossed by the black reference lines, indicating that the adsorbed carbamazepine molecule does indeed prefer to take an orientation similar to its form in the crystalline state, with the amide group facing downward toward the surface. In contrast, the preferred orientation angle of adsorption on the (1 0 -1) facet is less than $\frac{\pi}{2}$, meaning the amide group is facing upward, and there is a small degree of deviation between the minimum of the FES and the white reference line in Fig. 4-8(c). The lack of hydrogen bonding between the amide group and the (1 0 -1) facet could be the reason for the slight misalignment of the adsorbed carbamazepine, which would hinder the formation of a new ordered layer at the surface and lead to a slower growth rate.

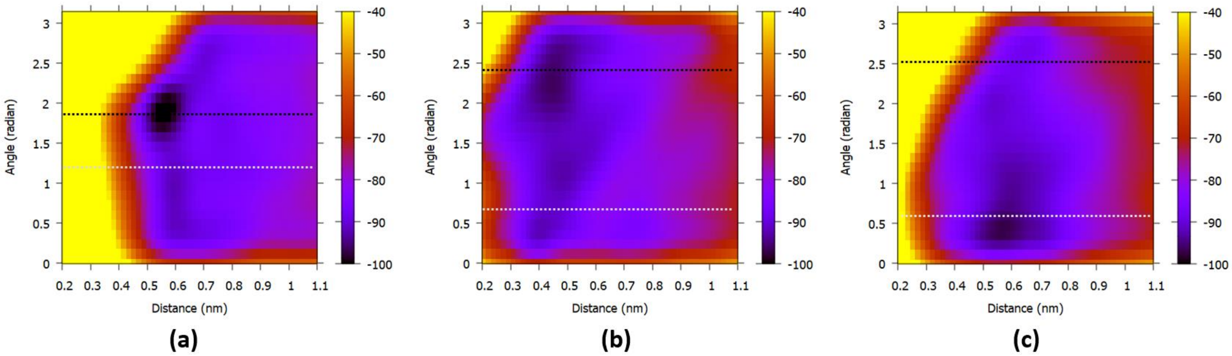

Figure 4-8. FES obtained from well-tempered metadynamics simulations for the adsorption of carbamazepine on ***(a)*** *(0 1 0),* ***(b)*** *(0 0 2), and* ***(c)*** *(1 0 -1) facets. The unit for the free energy is kJ/mol. The white and black dashed lines correspond to the mean values of the preferred angle of carbamazepine molecules in crystalline state in gray and black in Figs. 4-7(d) - 4-7(f), respectively.*

The adsorption of a single succinic acid molecule was also investigated, with the orientation vector defined as the vector connecting the center CG bead to the center of mass of the two carboxylic acid CG beads as illustrated in Fig. 4-6(b). The relative angle distribution in the cocrystal and the FES from WT-MD simulations for the three facets are shown in Fig. 4-9. For the (0 1 0) facet, there are two reference angles and the minimum of the FES slightly deviates from the white reference line. The minimum of the FES also does not correlate well with the reference angle for the (0 0 2) facet. While the adsorbed succinic acid molecule may indeed prefer to take a different orientation, it could also be that the orientation vector used is not suitable to describe the succinic acid molecule with two carboxylic acid groups. There are multiple degrees of freedom for succinic acid and the relative angle chosen as the collective variable does not account for its orientation with respect to the polar axis which lies in the horizontal plane. Nevertheless, the FES of (1 0 -1) facet in Fig. 4-9(f) is still significantly different from the other two, without deep energy minimum of a preferred angle near the surface, indicating that succinic acid is less likely to have a stable configuration for adsorption. This is also supported by the surface structure of (1 0 -1) facet in Fig. 4-7(c), where the crystal growth involves separate layers of carbamazepine and succinic acid, and the next new layer forming over the existing surface is expected to be composed of carbamazepine, not succinic acid. The absence of the other component in these single component layers may hamper their crystallization process, as observed in the cocrystal growth simulations of the (1 0 -1) facet.

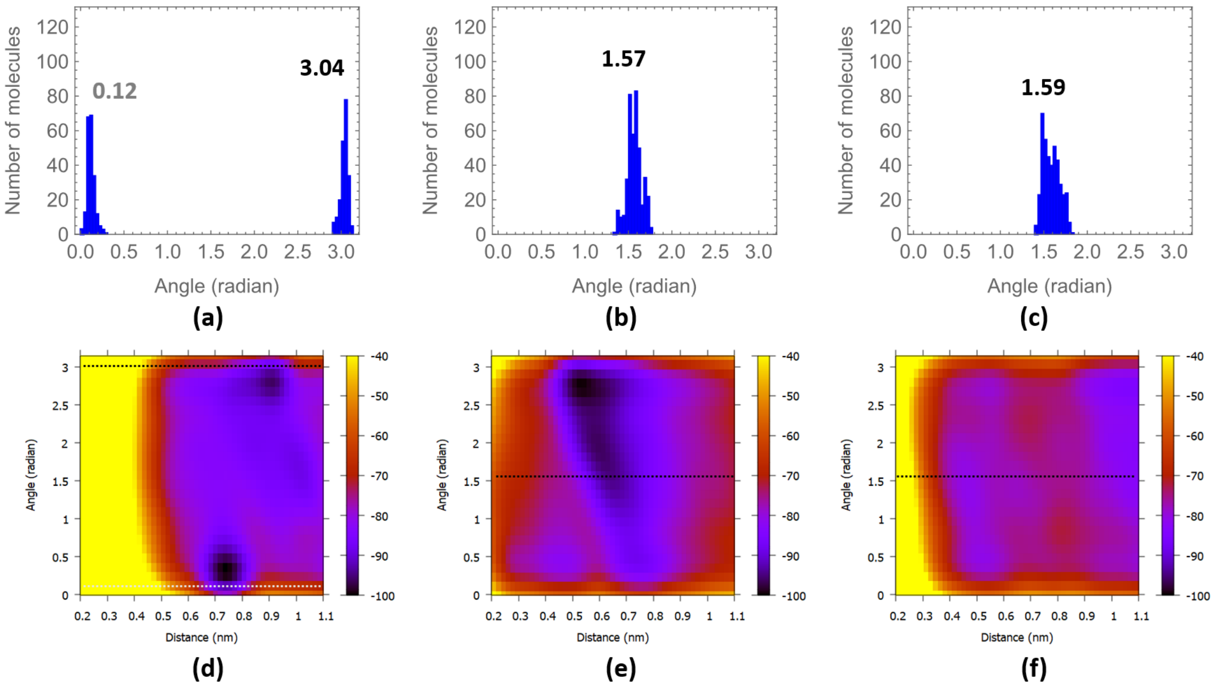

Figure 4-9. FES obtained from the well-tempered metadynamics simulation for the adsorption of succinic acid on ***(d)*** *(0 1 0),* ***(e)*** *(0 0 2), and* ***(f)*** *(1 0 -1) facets. The unit for the free energy is kJ/mol. The dashed lines correspond to the mean values of the preferred angle of succinic acid molecules in crystalline state in (a)-(c), respectively.*

The use of well-tempered metadynamics simulations to study the adsorption of single molecule on crystal surface has shed light on the different growth kinetics of various facets of the CBZ-SA cocrystal. However, these simulations have their limitations in fully understanding the crystallization mechanism as the actual process involves the interaction of multiple molecules near the surface. The results are also highly dependent on the surface layer structure and the choice of collective variables, thus further investigations are necessary to fully realize the potential of these biased simulations methods.

4.4 Conclusion and Future Directions

We have developed a coarse-grained model for the carbamazepine and succinic acid cocrystal consisted of five coarse-grained bead types. The non-bonded potential was generated using the iterative Boltzmann inversion method, which was based on the radial distribution function of the cocrystal structure obtained from atomistic simulation. The model allows for the direct simulation of pharmaceutical cocrystal growth from melt, and the growth kinetics of three crystal facets were investigated. Our findings show that the (1 0 -1) facet has the slowest growth rate, which is in line with the prediction from attachment energy calculations and crystal morphology observed in experiments. Well-tempered metadynamics simulations were performed to further explore the correlation between the molecular orientation of a single molecule adsorbed at the surface and the facet growth rate. The results indicate that the favored orientation of the carbamazepine molecule adsorbed at the surface of (0 1 0) and (0 0 2) facets matches its configuration in the crystalline state, while there is a small misalignment in the case of the (1 0 -1) facet, which might be caused by the lack of hydrogen bonding due to the orientation of the amide group. The adsorption of a single succinic molecule was also investigated, where no deep minimum on the free energy surface was found for the (1 0 -1) facet since the new crystal layer is expected to be consisting of carbamazepine molecules only.

Although we were able to simulate cocrystal growth using our coarse-grained model, we acknowledge its major limitations. Specifically, this method requires prior knowledge of the crystal structure, and the forcefield derived from a specific polymorph is unlikely to properly simulate the same molecules in other crystalline states. For instance, a different set of non-bonded interaction potentials is required to simulate the single crystal of carbamazepine compared to the cocrystal with succinic acid. One potential solution is use of a multi-state IBI scheme, which utilizes structural information from multiple physical states to generate the coarse-grained potential.[36] This approach has shown success in relatively simple systems with different density states and could be useful for different yet similar polymorphs of pharmaceutical crystals. Another avenue to validate our coarse-grained model is to employ an atomistic forcefield for the metadynamics simulations, allowing for comparison of results between atomistic and coarse-grained. Furthermore, optimizing the choice of collective variables is also a worthwhile direction to pursue.

4.5 Appendix

The full list of comparison of RDFs between different bead types from atomistic and coarse-grained simulations is included below (a total of 15 pairs).

A-A

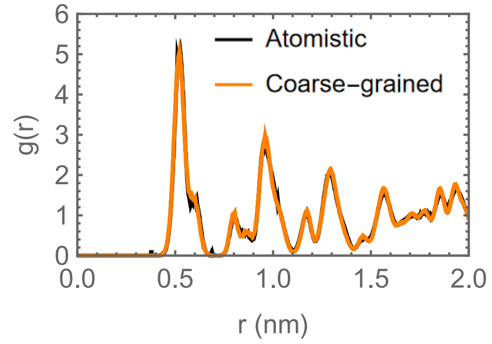

A-B

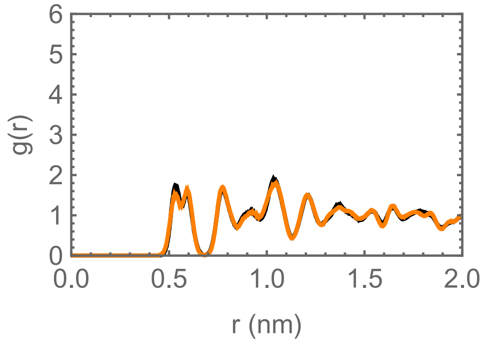

A-C

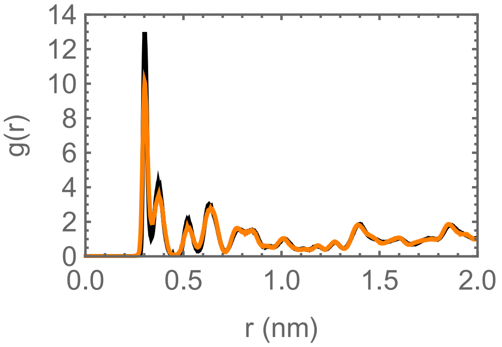

A-E

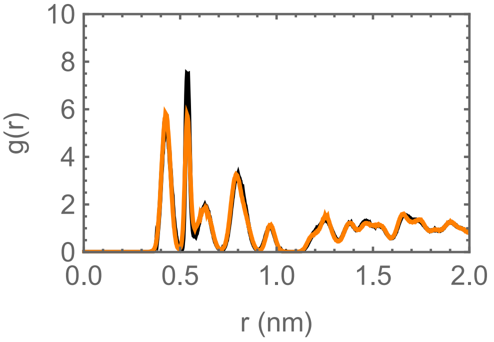

A-Z

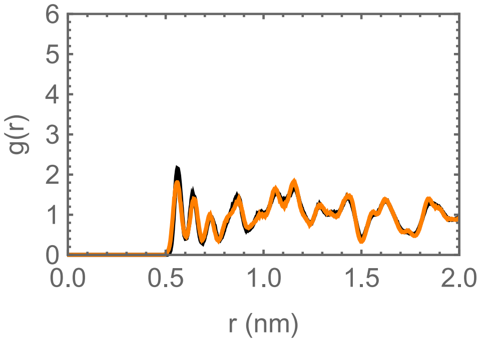

B-B

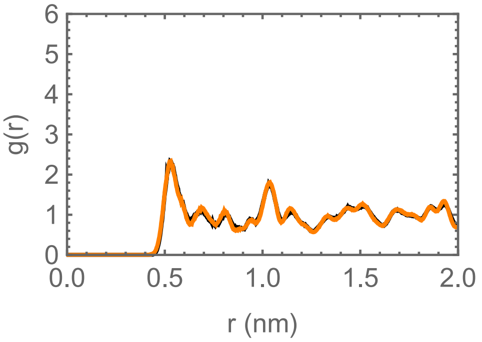

B-C

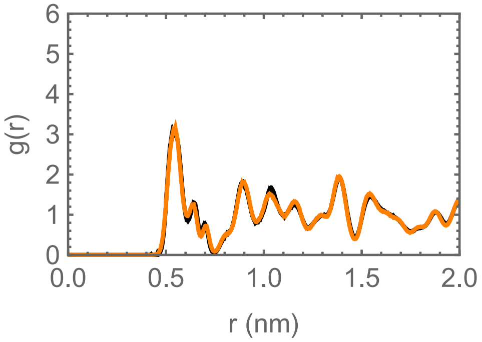

B-E

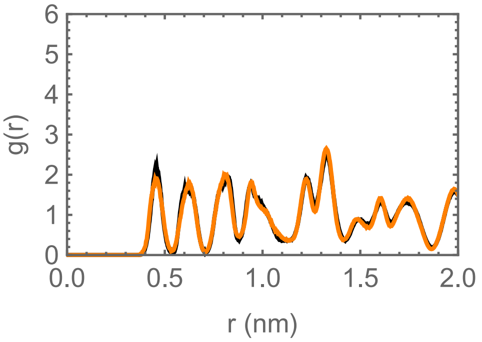

B-Z

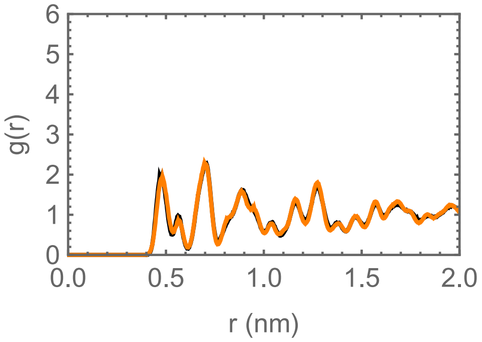

C-C

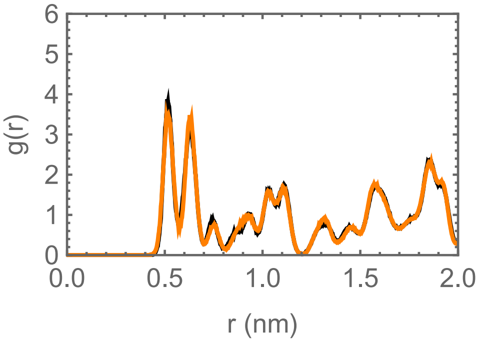

C-E

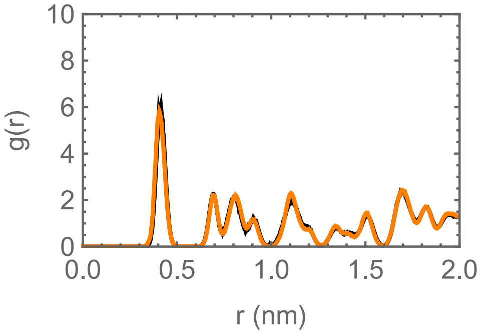

C-Z

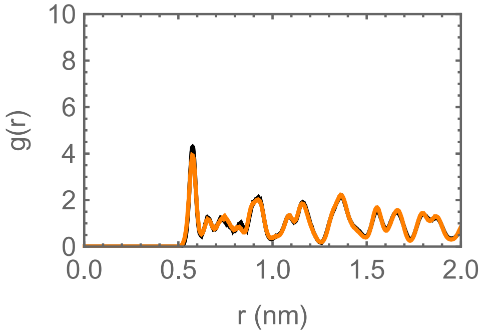

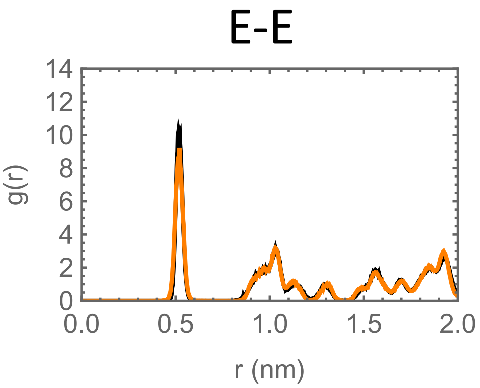

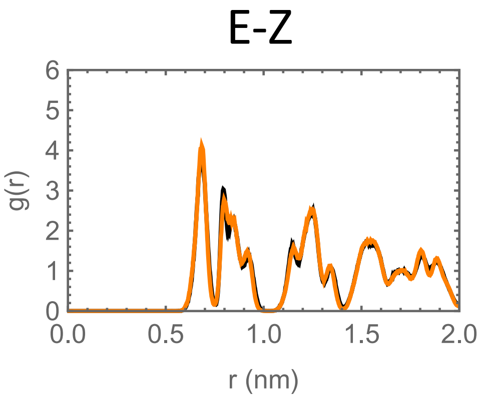

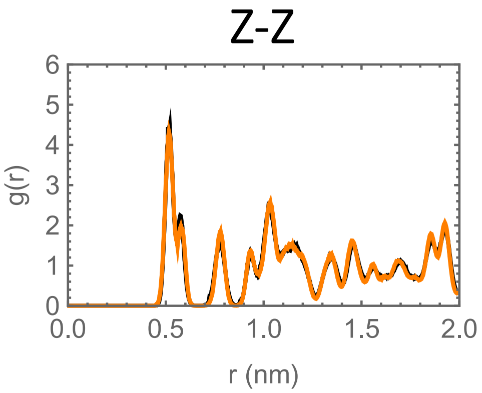

4.6 Reference

[1] Karimi-Jafari, M., Padrela, L., Walker, G. M., & Croker, D. M. (2018). Creating cocrystals: A review of pharmaceutical cocrystal preparation routes and applications. *Cryst. Growth Des.*, 18,10, 6370–6387.
https://doi.org/10.1021/acs.cgd.8b00933

[2] Sanvordenker, S., Borsadia, S., Morris, S., Rodríguez-Hornedo, N., & Shtein, M. (2022). Gas-assisted cocrystal desublimation. *Cryst. Growth Des.*, 22, 1528–1532.
https://doi.org/10.1021/acs.cgd.1c01241

[3] Nada, H. (2018). Computer simulations: Essential tools for crystal growth studies. *Crystals*, 8, 314.
https://doi.org/10.3390/cryst8080314

[4] Torrie, G. M., & Valleau, J. P. (1977). Nonphysical sampling distributions in Monte Carlo free-energy estimation: Umbrella sampling. *J. Comput. Phys.*, 23, 187–199. https://doi.org/10.1016/0021-9991(77)90121-8

[5] Laio, A., & Parrinello, M. (2002). Escaping free-energy minima. *Proc. Natl. Acad. Sci. U. S. A.*, 99, 12562–12566. https://doi.org/10.1073/pnas.202427399

[6] Allen, R. J., Valeriani, C., & Ten Wolde, P. R. (2009). Forward flux sampling for rare event simulations. *J. Phys.: Condens. Matter*, 21, 463102. http://doi.org/10.1088/0953-8984/21/46/463102

[7] Mandal, T., Marson, R. L., & Larson, R. G. (2016). Coarse-grained modeling of crystal growth and polymorphism of a model pharmaceutical molecule. *Soft Matter*, 12, 8246. https://doi.org/10.1039/C6SM01817C

[8] Salvalaglio, M., Vetter, T., Mazzotti, M., & Parrinello, M. (2013). Controlling and predicting crystal shapes: The case of urea. *Angew. Chem. Int. Ed.*, 48, 9346–9350. http://doi.org/10.1002/anie.201304562

[9] Salvalaglio, M., Mazzotti, M., & Parrinello, M. (2015). Urea homogeneous nucleation mechanism is solvent dependent. *Faraday Discuss.*, 179, 333–348. https://doi.org/10.1039/C4FD00235K

[10] Giberti, F., Salvalaglio, M., Mazzotti, M., & Parrinello, M. (2015). Insight into the nucleation of urea crystals from the melt. *Chem. Eng. Sci.*, 121, 51–59. https://doi.org/10.1016/j.ces.2014.08.032

[11] Salvalaglio, M., Perego, C., Giberti, F., & Parrinello, M. (2014). Molecular-dynamics simulations of urea nucleation from aqueous solution. *Proc. Natl. Acad. Sci. U. S. A.*, 112, E6–E14.
https://doi.org/10.1073/pnas.1421192111

[12] Singh, M. K., & Tiwari, V. S. (2015). Uncovering the mode of action of solvent and additive controlled crystallization of urea crystal: A molecular-scale study. *Cryst. Growth Des.*, 15, 7, 3220–3234.
https://doi.org/10.1021/acs.cgd.5b00346

[13] Santiso, E. E., & Trout, B. L. (2011). A general set of order parameters for molecular crystals. *J. Chem. Phys.*, 134(6), 064109.
https://doi.org/10.1063/1.3548889

[14] Santiso, E. E., & Trout, B. L. (2015). A general method for molecular modeling of nucleation from the melt. *J. Chem. Phys.*, 143, 174109.
https://doi.org/10.1063/1.4934356

[15] Maragliano, L., Fischer, A., Vanden-Eijnden, E., & Ciccotti, G. (2006). String method in collective variables: Minimum free energy paths and isocommittor surfaces. *J. Chem. Phys.*, 125, 024106.
https://doi.org/10.1063/1.2212942

[16] Liu, C., Cao, F., Kulkarni, S. A., Wood, G. P. F., & Santiso, E. E. (2019). Understanding polymorph selection of sulfamerazine in solution. *Cryst. Growth Des.*, 19, 12, 6925–6934.
https://doi.org/10.1021/acs.cgd.9b00576

[17] Anuar, N., Pauzi, N. S., Yusop, S. N. A., Azmi, N. S. M., Rahim, S. A., & Othman, M. F. (2018). Prediction of carbamazepine-succinic acid co-crystal dissolution in ethanolic

Solution using a Computational Molecular Dynamic Simulation Technique. *Intl. J. Eng. Technol.*, 7(4.18), 122–128.
https://doi.org/10.14419/ijet.v7i4.18.21884

[18] Mori, A. (2017). Computer Simulations of Crystal Growth Using a Hard-Sphere Model. *Crystals*, 7, 102.
https://doi.org/10.3390/cryst7040102

[19] Joshi, S. Y., & Deshmukh, S. A. (2021). A review of advancements in coarse-grained molecular dynamics simulations. *Mol. Simul.*, 47, 786–803.
https://doi.org/10.1080/08927022.2020.1828583

[20] Marrink, S. J., Risselada, H. J., Yefimov, S., Tieleman, D. P., & De Vries, A. H. (2007). The MARTINI force field: Coarse grained model for biomolecular simulations. *J. Phys. Chem. B*, 111, 27, 7812–7824.
https://doi.org/10.1021/jp071097f

[21] Jorgensen, W. L., Maxwell, D. S., & Tirado-Rives, J. (1996). Development and Testing of the OPLS All-Atom Force Field on Conformational Energetics and Properties of Organic Liquids. *J. Am. Chem. Soc.*, 118, 45, 11225–11236.
https://doi.org/10.1021/ja9621760.

[22] Chialvo, A. A., & Debenedetti, P. G. (1990). On the use of the Verlet neighbor list in molecular dynamics. *Comput. Phys. Commun.*, 60 (2), 215–224.
https://doi.org/10.1016/0010-4655(90)90007-N.

[23] Darden, T., York, D., & Pedersen, L. (1993). Particle mesh Ewald: An N·log(N) method for Ewald sums in large systems. *J. Chem. Phys.*, 98, 10089.
https://doi.org/10.1063/1.464397.

[24] Hess, B., Bekker, H., Berendsen, H. J. C., & Fraaije, J. G. E. M. (1997). LINCS: A linear constraint solver for molecular simulations. *J. Comput. Chem.*, 18 (12), 1463–1472. https://doi.org/10.1002/(SICI)1096-987X(199709)18:12<1463::AID-JCC4>3.0.CO;2-H.

[25] Berendsen, H. J. C., Van Der Spoel, D., & Van Drunen, R. (1995). GROMACS: A message-passing parallel molecular dynamics implementation. *Comput. Phys. Commun.*, 91, 43–56. https://doi.org/10.1016/0010-4655(95)00042-E

[26] Reith, D., Pütz, M., & Müller-Plathe, F. (2003). Deriving effective mesoscale potentials from atomistic simulations. *J. Comput. Chem.*, 24, 1624–1636. https://doi.org/10.1002/jcc.10307

[27] Srinivas, G., & Pitera, J. W. (2008). Soft Patchy Nanoparticles from Solution-Phase Self-Assembly of Binary Diblock Copolymers. *Nano Lett.*, 8, 2, 611–618. https://doi.org/10.1021/nl073027q

[28] Maffeo, C., Ngo, T. T. M., Ha, T., & Aksimentiev, A. (2014). A Coarse-Grained Model of Unstructured Single-Stranded DNA Derived from Atomistic Simulation and Single-Molecule Experiment. *J. Chem. Theory Comput.*, 10, 8, 2891–2896. https://doi.org/10.1021/ct500193u

[29] Srinivas, G., Cheng, X., & Smith, J. C. (2011). A Solvent-Free Coarse Grain Model for Crystalline and Amorphous Cellulose Fibrils. *J. Chem. Theory Comput.*, 7, 8, 2539–2548. https://doi.org/10.1021/ct200181t

[30] Mukherjee, B., Delle Site, L., Kremer, K., & Peter, C. (2012). Derivation of Coarse Grained Models for Multiscale Simulations of Liquid Crystalline Phase Transitions. *J. Phys. Chem. B*, 116, 29, 8474–8484. https://doi.org/10.1021/jp212300d

[31] Hartman, P., & Bennema, P. (1980). The attachment energy as a habit controlling factor: I. Theoretical considerations. *J. Cryst. Growth*, 49, 1, 145-156. https://doi.org/10.1016/0022-0248(80)90075-5

[32] Docherty, R., Clydesdale, G., Roberts, K. J., & Bennema, P. (1991). Application of Bravais-Friedel-Donnay-Harker, attachment energy and Ising models to predicting and understanding the morphology of molecular crystals. *J. Phys. D: Appl. Phys.*, 24, 89-102. https://doi.org/10.1088/0022-3727/24/2/001

[33] Rahim, S. A., Rahman, F. A., Nasir, E. N. E. M., & Ramle, N. A. (2015). Carbamazepine co-crystal screening with dicarboxylic acids co-crystal formers. *Int. J. Chem. Mol. Eng.*, 9, 5, 442-445.

[34] Barducci, A., Bussi, G., & Parrinello, M. (2008). Well-Tempered Metadynamics: A Smoothly Converging and Tunable Free-Energy Method. *Phys. Rev. Lett.*, 100, 020603. https://doi.org/10.1103/PhysRevLett.100.020603

[35] Tribello, G. A., Bonomi, M., Branduardi, D., Camilloni, C., & Bussi, G. (2014). PLUMED 2: New feathers for an old bird. *Comput. Phys. Commun.*, vol. 185, 2, 604-613. https://doi.org/10.1016/j.cpc.2013.09.018

[36] Moore, T. C., Iacovella, C. R., & McCabe, C. (2014). Derivation of coarse-grained potentials via multistate iterative Boltzmann inversion. *J. Chem. Phys.*, 140, 22, 224104. https://doi.org/10.1063/1.4880555

Chapter 5 Conclusion

We have demonstrated the utility of simulation and modeling methods across multiple time and length scales in investigating partially crystalline materials. Specifically, we used fully atomistic molecular dynamics simulation and constitutive modeling with mesoscopic scale analysis to study lamellar gel networks, as well as coarse-grained simulations to investigate pharmaceutical cocrystal growth.

Atomistic molecular dynamics simulations were conducted to investigate whether an interdigitated $L_{\beta I}$ phase is the equilibrium state of surfactant bilayers in lamellar gel networks. Lateral pressure and temperature scans along reversible pathways were used to drive reversible phase changes, including the formation of the $L_{\beta I}$ phase with interdigitated tails of opposing leaflets at negative lateral pressure. Using lateral pressure helps avoid kinetic bottlenecks that often occur when temperature alone is used as the control variable. Thermodynamic integration, with extrapolations to infinitely slow scans, revealed a positive free energy difference between the interdigitated $L_{\beta I}$ and non-interdigitated L_{β} phase which favors the latter, allowing for a quantitative evaluation of the stability of different bilayer phases.

To address similar kinetic limitations encountered in molecular simulations studying pharmaceutical cocrystal growth, we took a different approach. A coarse-grained model was developed for the cocrystal of carbamazepine and succinic acid, using the iterative Boltzmann inversion method based on the radial distribution function of the cocrystal structure obtained from atomistic simulation. The coarse-grained model enables direct simulation of cocrystal growth from melt. We found that the (1 0 -1) facet has the slowest growth rate, which agrees with the prediction from attachment energy calculations and the crystal morphology observed in experiment. Furthermore, well-tempered metadynamics simulations were performed to study the molecular orientation of a single molecule adsorbed at the surface of different facet, which provided some insight into the reason for the slow growth rate. While we acknowledge the limitations of our coarse-grained approach for cocrystals, as it requires prior knowledge of the crystal structure and cannot simulate the same molecules in other crystalline state, we suggest some future directions. One approach could be to use a multi-state IBI scheme, which would leverage structural information from multiple physical states to generate the interaction potentials and could be valuable for simulating different polymorphs of pharmaceutical crystals that share similarities in structure. Another way to validate our coarse-grained model is to employ an atomistic forcefield for metadynamics simulations, allowing for comparison of results between atomistic and coarse-grained simulations to identify the missing interactions from the coarse-grained model and their influence. Furthermore, optimizing the choice of collective variables is also a worthwhile direction to pursue.

In addition to microscopic scale molecular simulations, we proposed a constitutive model to investigate the macroscopic scale rheological properties of lamellar gels. The thixotropic model incorporates a boundary-induced gradient, which allows successful prediction of the complex rheology and the unique shear banding phenomenon of the material. The physical origin of the boundary-induced modulus gradient was discussed in relation to the lamellar microstructure under shear, and a more rigorous, microstructurally based approach to derive the variation of the modulus profile was suggested by doing a mesoscopic average over the lamellar anisotropy. Moving forward, it may be valuable to establish constitutive relationships between the tensor of mesoscopic average order parameter and the anisotropic elastic modulus, yielding condition, and viscous stresses. This could be achieved by linking the tensor change with a three-dimensional thixotropic elasto-visco-plastic model, which will likely require accounting for back-strain and/or back-stress and involving fourth rank tensors. Additionally, the inclusion of multiple thixotropic time scales may be necessary to capture the various time and spatial scales of the structures present in lamellar gel networks.

In conclusion, our studies on partially crystalline materials using simulation and modeling methods of multiple time and length scales have led to the development of novel techniques and models that provide new insights into the behavior of these complex systems. Our findings are not only relevant to the specific materials and processes studied, but they can also be applied to other similar systems and have the potential to contribute to the advancement of the field of modeling partially crystalline materials.